
UNIVERSITY OF
LIVERPOOL

# A Pulsed RF Discharge for a Caesium Free $H^-$ Ion Source

Thesis submitted in accordance with the requirements of the University of Liverpool for the degree of Doctor in Philosophy by

Michael James Barnes

September 2018

# Acknowledgements

I would like to thank Dr Mark Bowden for his continual guidance and support throughout this project, as well as everyone else in the plasma group (Paddy, Pete, Aaron, Francis, Ni, Youssef, Stefania, Dr. Kirsty McKay, Dr James Walsh, Andreas, Felix, Ella, David, Mo, Brandon, Matt... The list is very long.) for making every lunch (and the occasional evening) something to look forward to, and generally making Liverpool feel like a home away from home. I would also like to thank Gareth in the workshop for always being able to handle my non-stop requests, and anyone else at EEE I may have missed.

Lastly I would like to thank my parents for their continual support and encouragement.

# Abstract

Negative ion sources utilised in neutral beam injection (NBI) systems for ITER, DEMO, and future commercial reactors will be required to reliably output 40A of 1MeV $D^-$ with low co-extracted electrons for operating times of up to one hour. In order to meet these demanding criteria current fusion negative ion sources make use of caesium (Cs) in order to lower the work function of surfaces within the ion source and enhance the surface production of $H^-$ and $D^-$ ions. However it has been suggested that for DEMO/commercial fusion reactors that a similar Cs injection rate to ITER is likely to lead to NBI operational problems during the reactor's lifetime. Frequent maintenance or replacement of beamline components due to Cs contamination will result in unacceptable amounts of reactor downtime. Fusion NBI ion sources of the future will need to dramatically reduce their rate of Cs consumption, or will require alternatives to Cs for $H^-$ surface production.

In order to optimise the production of negative ions in the discharge, the electron temperature must be cooled in order to reduce the collisional detachment losses due collisions between $H^-/D^-$ ions and electrons in the plasma bulk. Negative ion sources planned for ITER make use of magnetic filters to reduce the electron temperature close to the extraction system of the ion source and maximise the density of negative ions in the region before they are extracted into the acceleration stage of the beamline. Time modulated discharges developed for use in damage free etching of silicon devices have shown to be able to generate a high density of volume produced negative ions without the use of Cs ovens. The pulsed nature of the discharge leads to low electron temperatures during the afterglow which result in enhanced production rates of negative ions through the dissociative attachment of rovibrationally excited hydrogen molecules.

In this work characterisation of a radio frequency, time modulated inductively coupled plasma source was carried out in both argon and hydrogen using a combination of Langmuir probe and retarding field energy analyser diagnostics. Time resolved Langmuir probe IV characteristics allowed insight into the evolution of $T_e$, density, and $V_p$ during the modulation cycle, as well as their response to changing discharge and modulation conditions such as gas pressure and modulation frequency. Similar techniques allowed the calculation of time resolved IVDFs of ions in the discharge.

During the activeglow, values of $T_e$, density, and $V_p$ measured during the quasi-steadystate phase

of an argon discharge agreed with other studies operating at similar discharge conditions, whilst the trends of plasma properties throughout the pulse agreed with calculations reported in the literature. During the afterglow the electron temperature rapidly cooled, falling to below 0.5eV in around 50$\mu$s whilst density decreased more slowly as ions and colder electrons diffused to the walls. Decay of the plasma density in the afterglow occurs more slowly, and agreed with analytical expressions for the decay of an electropositive discharge dominated by diffusion to the walls.

Time resolved measurements of plasma parameters in a hydrogen discharge also demonstrated similar responses to changing discharge or pulse parameters. However the molecular nature of hydrogen lead to reduced plasma densities during the activeglow, and more pronounced peak or overshoot of $T_e$ and $V_p$ during the first few $\mu$s of the pulse. During the afterglow $T_e$ and $V_p$ more rapidly decayed, decreasing to below 0.5eV on the order of 10$\mu$s. Density measurements in the afterglow suggested that the decay was mostly controlled by diffusion to the walls.

Boron doped diamond samples were placed around the extraction grid, measurements using Langmuir probes and RFA diagnostics in the extraction region and below the extraction grid were conducted in an attempt to observe any enhancement in the negative ion density in the region. No significant difference was found in the extraction region plasma properties between discharges with the BDD samples present and those without. This is likely due to intrinsic negative ion densities in the discharge being too small for the measurement techniques implemented to be able to resolve. As a result it is inconclusive as to the extent BDD enhances the surface or volume production of $H^-$ ions.

Whilst measurements of the effects of BDD on the discharge were unsuccessful, this work was successful in developing and characterising a time modulated ICP discharge in both argon and hydrogen. Whilst many modelling and experimental studies have been carried out in the area of pulsed argon discharges, there has been little research conducted into time modulated hydrogen discharges. The work carried out in this project into the time evolution of hydrogen plasma properties and their response to an extraction bias in the pulsed environment should form a useful contribution to the field.

# Contents

# Chapter 1

# Introduction

## 1.1 Plasma

Over 99% of all matter in the observable universe (excluding more exotic forms such as dark matter) exists in this plasma state. The sun's mass is almost entirely composed of plasma, as is the mass of every other star. Even the matter which exists in the interplanetary, interstellar, and intergalactic mediums exists in an almost fully ionised plasma state.

Terrestrial plasmas also exist in many forms, such as lightning, the ionosphere surrounding the earth in the upper atmosphere, and the auroras visible at the poles. Plasmas are the fourth state of matter and are composed of an ionised gas (either partially of completely) which exhibit collective behaviours and maintains quasineutrality [1].

Quasineutrality is a property through which plasmas will naturally try to maintain an overall net neutral charge. Perturbing electromagnetic fields are screened over a characteristic length scale, known as the Debye length, in order to maintain a net neutral charge over the global scale of the discharge. Upon the start up of a plasma, electrons will quickly move away to the chamber walls due to their lighter mass and greater mobility. This in turn leaves a net positive group of ions remaining. An electric field is established which decelerates the electrons/accelerates the ions such that no net current flows out of the plasma. At the chamber walls, the initial electron flux creates

a negative potential which then repels subsequent lower energy electrons from reaching the walls. This potential also generates an electric field which accelerates ions to the Bohm velocity in order to cancel the electron current. This region of depleted electron density is referred to as the plasma sheath.

Collective behaviour refers to elements of plasma in the bulk being able to affect the motion and dynamics of other elements, even at large distances. Motion of charged particles leads to the formation of magnetic fields which perturbs the trajectories and motion of other particles in the plasma. The behaviour of particles in the plasma does not depend solely on the local conditions.

Plasmas on Earth can generally be categorised into atmospheric pressure plasmas and low pressure plasmas.

### 1.1.1 Atmospheric Pressure Plasmas

Atmospheric pressure plasma discharges have numerous useful properties, and are currently in use or under research for use in a variety of different industries. As the gas pressure is around one atmosphere, there is no need for expensive vacuum chambers and pumping equipment. They are currently under investigation for use in biomedical applications such as the removal of bacteria from surfaces [2], and killing of cancerous tissue inside the body [3]. Atmospheric pressure plasmas are also being considered for the capture and conversion of $CO_2$ into CO [4], which can be used for reduction of emissions from industrial processes and recycling of the captured $CO_2$ into useful substances. Understanding plasma catalysis of these chemical processes is also a large area of current research [5].

### 1.1.2 Low Pressure Plasmas

Low pressure plasmas make use of vacuum chambers and vacuum pumps The short mean free path of electrons at atmospheric pressure restricts their energy distributions and means a lot of useful plasma chemistries are inaccessible at high pressure. Low pressure plasmas have a myriad of uses, from etching of semiconductor devices for technological purposes [6], sputtering of a target material onto a substrate for deposition of thin films [7], to use as a possible energy source through nuclear

fusion [8]. Low pressure discharges are found in a a variety of set-ups, such as capacitive discharges, filamented arc discharges, magnetrons, and inductively coupled plasmas. The ionisation degree of low pressure plasmas varies from fractions of a percent, to a fully ionised plasma in which there are no neutral atoms present in the mixture. Low pressure plasmas can generally be categorised into two types: thermal and non-thermal. In non-thermal plasmas, the ions and electrons are not in thermal equilibrium and have two distinct temperatures. The neutral gas and ions are generally considered to both be at room temperature, 300K, whilst the electrons have a temperature on the order of an electron Volt, around 10,000K.

It is hoped that high temperature, fully ionised, low pressure hydrogen discharges can be controlled and sustained in order to reliably generate electricity through fusion power here on earth.

## 1.2 Nuclear Fusion

Nuclear fusion is the process which powers the core of the sun, and a substantial amount of research has been conducted over the past 60 years in order to utilise this process here on Earth for electricity generation. Compared to nuclear fission, the fusion reaction process does not produce long lived radioactive isotopes. The waste it does inevitably produce would be short lived, and recyclable within very short period of time compared to fission by-products. Since the plasma conditions necessary to maintain the fusion reactions are so strict any significant perturbations will lead to the plasma cooling or extinguishing entirely, stopping the fusion mechanism and preventing any chance of a chain reaction leading to a meltdown. It also (depending on the reaction used) has essentially limitless fuel reserves, making it a highly desirable energy production mechanism.

The core of the sun makes use of a three step proton-proton fusion mechanism, as the intense gravity allows the core to confine the gas at extremely high densities and temperatures for large periods of time. This will not be possible for terrestrial fusion machines, so the focus of the research has been towards achieving deuterium-tritium (DT) fusion

$$D + T \longrightarrow He\,(3.5MeV) + n\,(14.1MeV)\,, \tag{1.1}$$

which has the largest cross section for plasma conditions thought to be achievable in a fusion reactor on Earth, as shown in figure 2.1. Whilst the reaction itself does not produce any radioactive isotopes, the high energy neutrons generated will inevitably propagate through the first wall of the reactor and beyond. Here the neutron interactions will cause transmutation of nuclei in the reactor components, which will lead to radioactive components and waste.

The gas must be heated to over 10keV in order for the nuclei to be able to move in close enough proximity to overcome potential barriers and fuse. The conditions required for a fusion reactor to achieve ignition is given by the Lawson criterion

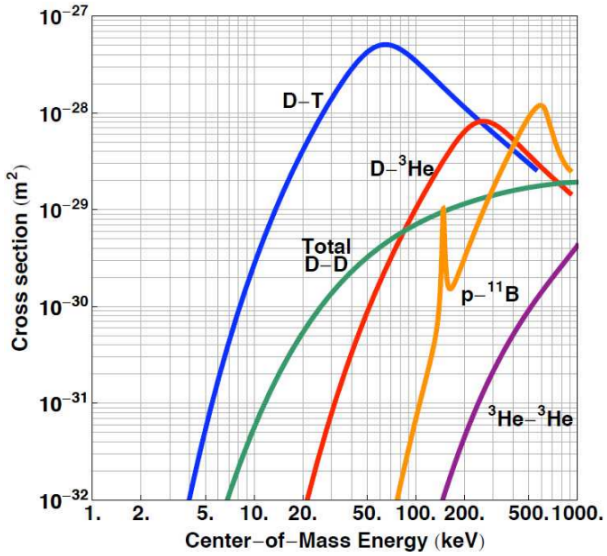


Figure 1.1: Cross-sections of various possible fusion reactions. With the temperatures achievable with current technology, deuterium-tritium has the largest reaction cross section and as a result is where the majority of the research focus lies [9].

There are currently two main techniques being investigated in order to fulfil the Lawson criterion are Magnetic Confinement Fusion (MCF) and Inertial Confinement Fusion (ICF). ICF [10] involves the use of high powered lasers to isotropically compress a pellet of DT fuel. The outermost layer of the fuel pellet is rapidly ablated by the lasers, causes an inertial shock wave to propagate through the fuel. As the shock wave compresses the core of the fuel, the density and temperature increases such that ignition is achieved and fuel undergoes fusion before the pellet explodes/vaporises.

MCF involves the use of powerful magnetic fields to confine a hot, dense plasma. MCF devices

are generally tokamaks or stellarators. Tokamaks [11] use toroidal and poloidal field coils to create a torus shaped magnetic field topology to confine plasma. The current in a central solenoid is ramped up to inductively generate the plasma current, which helps improve plasma confinement. Stellarators have a much more complicated field coil arrangement, which generates the rotational transform and plasma current without ramping the current in a central solenoid [12].

Heating of the plasma is carried out by electron cyclotron resonance heating (ECRH), ion cyclotron resonance heating (ICRH), and neutral beam injection. As ions and electron traverse along the magnetic field lines in the tokamak they move along spiral trajectories with an intrinsic period of rotation. ECRH and ICRH use electromagnetic radiation with frequencies tailored to match the frequency of gyration of the ions and electrons in order to resonantly heat the particles. However due to the strong absorption of the EM radiation it is not able to penetrate very far into the plasma, so whilst ECRH and ICRH are effective in heating the outer layers of the plasma they are unable to heat the core. NBI makes use of high energy beams of neutral particles, which can move through the tokamak unaffected by the magnetic fields and are able to reach the central region of the plasma. The beams are injected tangentially or radially into the plasma, where they are able to effectively heat the core to fusion relevant temperatures.

### 1.2.1 The Fusion Roadmap

In 2012 the European Commission requested that the European Fusion Development Agreement (EFDA, now replaced with EUROfusion) create a technical roadmap in order to achieve electricity generated by fusion power by 2050 [8]. The agreement maps out the problems which need to be solved to realise fusion energy, as well as the roles of key facilities. Currently the most important machine in the development of tokamak based fusion power is the ITER facility under construction in Cadarache, France. In recent years the timeline of the roadmap has been pushed back due to delays in ITER's development and construction, but the plan remains largely the same.

The roadmap outlines the issues which must be addressed in order to achieve fusion power. These include neutron resistant materials, tritium self-sufficiency, problems with heat exhaustion, as well as training the next generation of fusion scientists to operate ITER and eventually DEMO. ITER

is the key facility on the tokamak fusion roadmap. Its success will be crucial in the development of DEMO and fusion reactors beyond, both in demonstrating the feasibility of fusion power and the lessons learned in the operation and maintenance of the machine. Whilst the main focus of the fusion roadmap is on fusion power from tokamaks, it also outlines the possibility of stellarators being the long term alternative to tokamaks as they have some intrinsic advantages over tokamaks. However the technology associated with stellarators is not yet mature enough to achieve electricity generation by 2050. During ITER's construction and commissioning JET and JT60-SA (currently being upgraded to be superconducting) will investigate and assist in reducing the risks associate with each of ITER's operating modes: Inductive (JET), and steady state (JT60-SA).

The general plan of the fusion roadmap is for ITER to achieve its goal of achieving a net energy gain from the DT fusion plasma, as well as showcasing the feasibility of long pulse/steady state operation with non inductive current drive, technologies for heat exhaustion in the divertor and tritium breeding. After this the construction of a demonstration fusion power plant would begin. ITER will continue its operation during the construction of DEMO. DEMO will generate electricity from the power produced by the plasma, after which more fusion reactors will be constructed and fusion as an energy source will have been established.

### 1.2.2 ITER

The ITER tokamak [13] is the next large experimental tokamak on the fusion road map. It is a critical step towards fusion energy that as this machine will demonstrate a net energy gain with the ultimate goal being Q=10, i.e. the fusion power output generated by the plasma is ten times the heating power put in. Ideally once this net energy gain has been established the next MCF device would be a demonstration fusion reactor which generates electricity (DEMO). The 23,000 ton machine will heat its plasma to over 150 million degrees C, ten times the temperatures found in the core of the sun, in order to generate up to 500MW of fusion power.

The torus itself has a major radius of 6.2m, with a minor radius of 2m, giving a plasma volume of 837m$^3$. The toroidal and poloidal field coils situated around the tokamak have field strengths of 12T and 6T respectively. The toroidal field coils will be constructed using Nb3Sn (Niobium

Tin) superconductors, and poloidal made from Nb-Ti (Niobium-Titanium) superconductors, due to reduced field strength constraints. The magnetic field coil system is the most expensive piece of the ITER tokamak, and its large size and scale will push the limits of modern manufacturing techniques. Heating systems comprise of 2 16.5MW NBI beamlines, 20MW of ECRH, 20MW of ICRH, and 20MW of lower hybrid. ITER will initially operate in an inductive pulsed regime, where the current in the central solenoid is ramped to generate plasma current. After this it will eventually move to long pulse and steady state operation which will make use of non-inductive current drive, e.g. the use of NBI to generate plasma current.

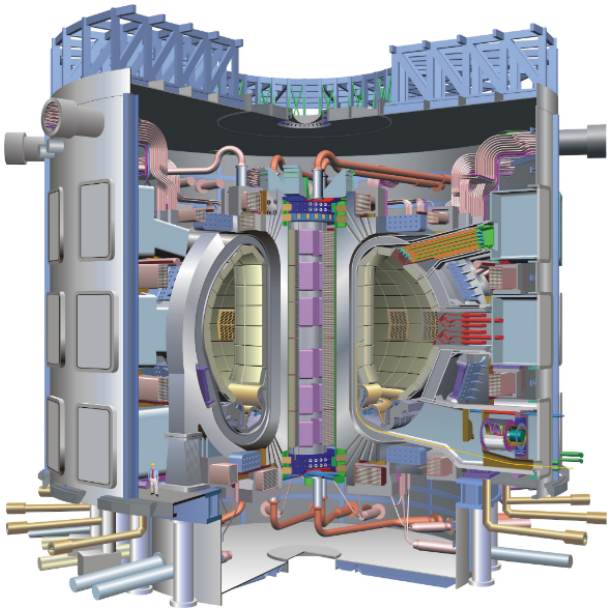

Figure 1.2: The ITER tokamak currently under construction in Cadarache.

Fusion power has progressed significantly since it's conception in the 1950s, but there are several problems which must be solved if commercial nuclear fusion reactors will be realised in the future. ITER will attempt to address many of these problems during its lifetime, and demonstrate the feasibility of technologies before moving onto commercial fusion power plants.

The large fluences of high energy neutrons represents a radiation environment that current materials have not been exposed to, and cannot (currently) be replicated. As the neutrons have large energies (14.1MeV) and have no charge, they are capable of traversing large distances through reactor materials. Neutrons will leave behind cascades of displaced atoms and damage to the crystal

lattice, some of which repairs itself through annealing, but permanent damage builds up over time with neutron fluence which will significantly affect the crystal structure and material properties during the lifetime of the reactor. Materials have to be designed such that they are able to handle years of neutron bombardment without significant changes to mechanical and thermal properties, and also do not produce any long lived radioactive isotopes through transmutation.

A system which utilises the neutron flux to breed tritium fuel without significant tritium retention must also be developed. It is expected that a commercial fusion reactor will consume NUMBER of tritium. Currently tritium is rare, expensive, and only produced in small quantities by fission reactors. This supply of tritium will be enough to start commercial reactors, but will be insufficient for long term operation of the machine - reactors will have to breed their own supply of tritium fuel. Lithium can be used for this process

$$Li + n \longrightarrow He + T \tag{1.2}$$

but the breeder layer must be able to breed and extract enough fuel to keep the machine running whilst at the same time preventing tritium diffusing into other components, and limiting the amount of tritium in the system/in storage as the maximum stockpile of tritium is strictly controlled. Current ideas include layers of flowing liquid lithium, or solid lithium pebbles to produce a supply of tritium during the reactor's operation. Lithium is quite corrosive however and so components must be carefully designed to minimise the required maintenance over the reactor's lifetime. Issues such as prevention of hydrogen/tritium diffusing out of the lithium mixture and into other components must also be solved.

As tokamaks move towards long pulse and steady state operation, neutral beam injection (NBI) systems will most likely have to deliver non inductive current drive into the plasma. In ITER, NBI will have to provide stable high power beams for pulse lengths of up to one hour. This requires the development of negative ion sources that are able to provide the required ion beam current and energy for the duration of the pulse. The ITER NBI negative ion sources will make use of caesium to enhance the surface production of $H^-$ ions near the plasma grid of the ion source (Discussed in section 2.3.2). Whilst caesium is useful for producing a high density of negative ions

and a decreased co-extracted electron current, it will have to be regularly removed from beam line components and Cs ovens will have to be refilled. This will not be an issue for ITER but for commercial fusion reactor the maintenance required for the ion sources and beam line components will be unacceptable. The fraction of time the reactor spends not generating electricity during maintenance periods is crucial in determining the final cost of electricity from a fusion reactor. If the reactor has to spend significant time repairing the NBI systems due to build up of caesium then fusion will never be economically competitive with alternative electricity sources. This means that for DEMO and commercial reactors Cs has to be used much more efficiently with significantly reduced build up in NBI components, or alternatives materials to Cs must be used in the negative ion sources.

# Chapter 2

# Literature Review

This Review discusses negative ion production and sources in the context of both fusion and non-fusion neutral beams. Negative hydrogen ions are currently of interest across several fields. In the field of spacecraft propulsion, ion propulsion systems are considering their use in ion-ion, positive and negative ion plasma engines. For particle physics negative ion sources are used for particle accelerator beam sources and for plasma etching of semiconductor devices in the materials processing/integrated circuit industry. In nuclear fusion $H^-$ sources are utilised for neutral beam injection (NBI) for nuclear fusion applications, and $H^-$ ions may also play an important role in achieving acceptable heat loads onto tokamak divertors. Negative ion sources and neutral beams could also prove to be useful for materials processing and microelectronics industries, as future microchips and integrated circuits will require damage free anisotropic etching techniques for feature sizes $\leq$10nm, which could be provided by neutral beam etching.

In magnetic confinement fusion (MCF), NBI forms one of the heating mechanisms used in tokamak and stellarator devices. NBI will also be essential for the generation of non-inductive current drive for long pulse or steady state operation of future MCF devices and reactors. Powerful and reliable ion sources are currently under development to meet the requirements of future tokamaks on the path to realising sustainable electricity generation through nuclear fusion.

The structure of the review is as follows: Section 2.1 of this review summarises neutral beam

injection, with a focus on ion sources used on current generation NBI systems, and the research currently developing negative ion sources for the ITER tokamak. Section 2.2 discusses inductively coupled plasma discharges and the E-H transition. Section 2.3 discusses $H^-$ production and loss mechanisms. Magnetically filtered and temporally filtered ion sources, including the dynamics of pulsed plasmas, are reviewed in sections 2.4 and 2.5 respectively. The need for Caesium free ion sources for tokamaks beyond ITER is in section 2.6, and negative ion sources and neutral beams used for plasma etching are discussed in section 2.7 before the summary of the review in section 2.8.

## 2.1 Neutral Beam Injection

NBI is one of the primary heating mechanisms used in MCF devices. Ions extracted from a source are accelerated to high energies (usually several KeV) before neutralisation. After neutralisation excess ions and electrons are removed from the beam using electric fields and sent to an ion dump. High energy neutral particles are then able to traverse the magnetic field and enter the fusion plasma where they transfer their energy through collisions, heating the plasma to fusion relevant temperatures. The efficiency with which the ion beam can be extracted and neutralised will be crucial in determining the efficiency of the tokamak and ultimately the cost of electricity.

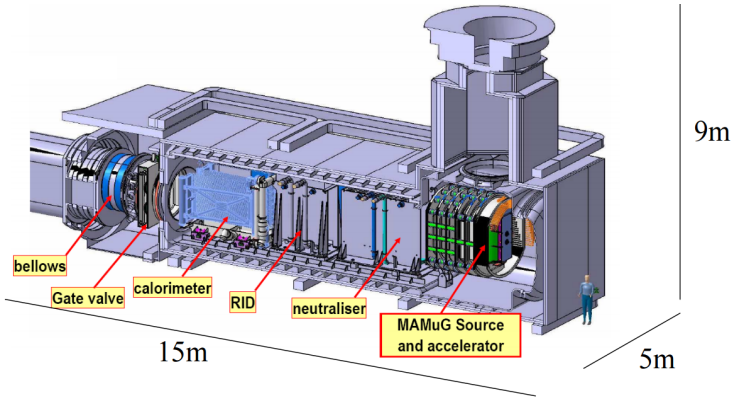


Figure 2.1: Conceptual design of an ITER neutral beam injector.

Almost all tokamaks currently in operation use positive ion based neutral beam injectors. Stellara-

tors such as Wendelstein 7-X [14] and LHD also make use of NB heating. W7-X uses short NBI pulses of H and D atoms, 1.3MW and 2MW for tangential injectors, 1.1MW and 1.8MW for radial injectors. The construction of the neutral beam injectors is slightly more complicated as the beam must enter the machine between the complicated field coil arrangement. The NBI heating power of some tokamaks are summarised in figure 1.

| | $R_0$ (m) | $a$ (m) | $I_p$ (MA) | $B_t$ (T) | Installed heating power (MW) | | | | |
|---|---|---|---|---|---|---|---|---|---|
| | | | | | P-NBI | N-NBI | ECRH | ICRH | LH |
| ITER | 6.2 | 2.0 | 15 | 5.3 | - | 33 | 20 | 20 | - |
| JET | 2.96 | 1.25 | 4.8 | 3.45 | 34* | - | - | 10 | 7 |
| JT-60U | 3.4 | 1.1 | 5 | 4.2 | 40 | 3 | 4 | 7 | 8 |
| JT-60SA | 2.97 | 1.17 | 5 | 2.25 | 24 | 10 | 7 | - | - |
| TFTR | 2.4 | 0.8 | 2.2 | 5 | 40 | - | - | 11 | - |
| EAST | 1.7 | 0.4 | 1.0 | 3.5 | - | - | 0.5 | 3 | 4 |
| DIII-D | 1.67 | 0.67 | | 2.1 | 20 | - | 5 | 4 | - |
| ASDEX Upgrade | 1.65 | 0.65 | 1.2 | 3.1 | 20 | - | 6 | 8 | - |

*recently upgraded

Figure 2.2: Heating power for various past, present, and future tokamaks [15]

NBI systems which are based on negative ion sources will be essential for next generation MCF devices. Devices such as the JT-60 tokamak and the LHD stellarator are currently testing negative ion neutral beam injectors. JT-60SA [16] will use two positive ion neutral beam injectors and one negative ion based source. LHD also uses a negative ion based NBI system [17], each source aiming to achieve 40A of 180keV using filamented ion sources. Sources which operate using filaments have shorter lifetimes and more complicated designs than those which use an RF inductively coupled plasma. The frequency at which maintenance must be performed on the ion sources must be kept to a minimum, so future NBI ion sources use RF ICPs. Development of efficient and reliable negative ion NB sources will be crucial for the next generation of tokamaks such as ITER and eventually a demonstration fusion reactor DEMO.

### 2.1.1 ITER NBI

A 1MeV beam of neutral deuterium atoms will provide 33MW of heating power to achieve a burning fusion plasma in ITER, as well as generating the necessary non inductive current drive to improve confinement of the plasma and increase pulse length. The requirements for the ITER NBI system are 40A of 1MeV D atoms for up to 3600s.

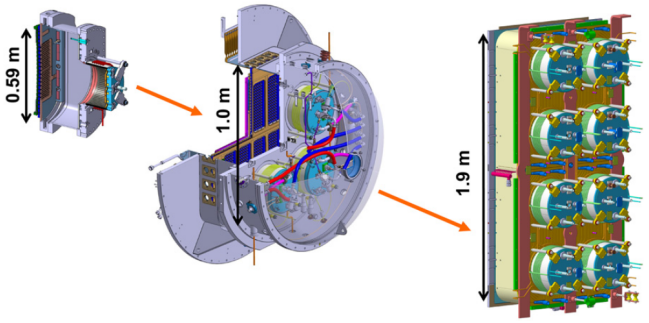


Figure 2.3: Scaling of NBI negative ion sources from an IPP prototype source to a full scale ITER NBI source which uses eight IPP sources with a large extraction area [18].

Sources currently being developed to fulfill the ITER NBI criterion are the half size ITER source ELISE at IPP Garching [19, 20], the full size ITER source SPIDER [21] based at Padova, and the planned full size NB injector MITICA [22] also based in Padova, Italy. Previous test sources used to demonstrate certain ITER NBI relevant parameters were the BAvarian Test MAchine for Negative ions (BATMAN) facility, MANITU, and RADI sources [23].

Currently the ITER relevant conditions have not been met by a single ion source simultaneously. The ELISE (Extraction from a Large Ion Source Experiment) source is designed to meet the ITER NBI source parameters, demonstrate large scale extraction of $H^-$ and $D^-$ ions for 400s and 3600s respectively. After the half size ITER source ELISE, the SPIDER ion source will then be used to optimise the performance of a full scale ITER like source. Ions from the SPIDER source will be extracted using a 100kV extraction system. The MITICA full size NB injector test bed will then extract ions from a full scale source at the ITER requirement of 1MV for the full 1h pulse length. The Scaling from the IPP prototype sources to a full scale ITER source like the planned SPIDER source is shown in figure 2.3.

The use of positive ion based NBI systems will not be possible for the ITER system due to the increased beam energy. At 1MeV, the neutralisation cross section for $H^+/D^+$ is so small that a positive ion based NBI would be too inefficient for commercial nuclear fusion reactors to ever be economically competitive. Negative ion neutralisation cross section however remains constant at higher beam energies (figure 2.4). As a result, the ITER NBI system will utilise negative ion sources. Due to the finite neutralisation cross section for the negative ions, the criterion for the ITER NBI ion sources are to deliver 69A of Hydrogen and 57A of Deuterium ions consistently throughout the duration of each ITER pulse [24]. The source will also require a high ratio of extracted negative ions to electrons for improved source efficiency and to reduce incident heat loads on extraction grids and residual ion/electron dump.

## 2.2 ICP Plasmas

Inductively coupled plasmas (ICPs) are useful for plasma processing/etching due the added flexibility of the ability to independently bias a substrate within the plasma without affecting the incident ion flux . See [25] for further reading. The principle behind ICP discharges is to use an RF current in an adjacent coil, usually separated from the discharge by a dielectric window. The resulting changing magnetic field from the coil induces an RF current in the plasma. Input RF power from the coil determines the ion density/flux, whilst the bias on the substrate controls the ion energy. In capacitively coupled discharges the ion energy and flux both depend on the absorbed power into the plasma, and so independent control of the two parameters is difficult to achieve. ICP coil configurations are typically cylindrical or planar

heating of electrons occurs through collisional/ohmic heating and by a collisionless process in which electrons interact with the oscillating RF sheaths present in the discharge. These power transfer mechanisms occur within a thin layer close to the plasma surface known as the skin depth. The spatial decay constant of EM waves propagating normally to a boundary of uniform plasma is given by

$$\alpha = -\frac{\omega}{c} Im\kappa_p^{1/2}, \tag{2.1}$$

where

$$\kappa_p \approx -\frac{\omega_{pe}^2}{\omega^2(1 - j\nu_m/\omega)}, \tag{2.2}$$

is the relative plasma dielectric constant. In this equation $\omega_{pe}$ is the plasma frequency, $\nu_m$ is the electron neutral collision frequency, and $\omega$ is the frequency of the incident EM radiation. In ICP plasmas RF waves typically oscillate at a lower frequency than the plasma frequency, leading to evanescent propagation of the waves, i.e. they are attenuated rapidly by the electrons and the currents induced by the RF field flow within the skin depth $\delta$ of the system

$$\delta \equiv \frac{1}{\alpha}. \tag{2.3}$$

Equation 2.2 shows that there are two collisionality regimes for the skin depth. If $\nu_m \ll \omega$ then equation 2.2 reduces to

$$\delta_p = \frac{c}{\omega_{pe}} \tag{2.4}$$

which is the collisionless skin depth. If however the electron neutral collision frequency is much greater than the plasma frequency, $\nu_m \gg \omega$, and expand equation 2.2 then

$$\alpha = -\frac{1}{\sqrt{2}}\frac{\omega_{pe}}{c} \approx \delta_c^{-1}, \tag{2.5}$$

which yields a collisional skin depth

$$\delta_c = \delta_p \frac{2\nu_m}{\omega} \tag{2.6}$$

where $\delta_c$ is the collisional skin depth. A third skin depth regime also exists, in which the interaction time of the skin layer with the electrons is short relative to the time scale of the RF oscillations or the neutral collision frequency. This leads to an anomalous skin depth $\delta_e$ related to the collisionless

skin depth by

$$\delta_e = \delta_p \left( \frac{C_e \nu_e}{2\omega\delta_p}^{1/3} \right) \tag{2.7}$$

Where $\nu_e$ is the interaction frequency between the electrons and skin layer. In high density discharges the skin depth is much smaller than the chamber dimensions and the RF is absorbed screened by the plasma in a short distance close to the coil. At low density regimes (such as when capacitive coupling dominates the discharge), the skin depth is on the order of or larger than the plasma dimensions. The EM radiation propagates freely throughout the discharge and the RF oscillations are large.

The rate at which the electric and magnetic fields from the coil decay in the plasma increases with electron density. The electrons quickly respond to maintain quasineutrality close to the sheath at the walls and at high density the skin depth is small, with the E and B fields exponentially decaying to zero at the centre of the discharge. In a cylindrical discharge the RF current flowing in the plasma is given by

$$I_p = N I_{coil} \left[ \frac{1}{J_0(kr_0)} - 1 \right] \tag{2.8}$$

where $I_{coil}$ is the current flowing in the coil of N turns, k is the wave number, $r_0$ is the radius from the centre of the discharge to the dielectric, and $J_0$ is a Bessel function. The plasma current increases with electron density until all of the current is confined within the skin depth and the plasma current is equal to the coil current. The current induced in the skin depth flows in the opposite direction to the movement of current in the coil, which cancels the magnetic field induced by the coil (Due to the fact the magnetic field is nearly constant in the dielectric window there are negligible currents flowing through the dielectric, though there is a displacement current).

### 2.2.1 E-H Transition

An important phenomenon associated with ICP plasmas is the E to H transition. ICP generally have two discharge modes: an electrostatic E mode, and the electromagnetic H mode. The coil used to generate the ICP is capacitively coupled to the plasma, i.e. a plasma can be ignited by the electric field which exists between turns of the coil and ground. At lower input powers, the electrostatic coupling between the coil and the plasma generally dominates. In the capacitive E mode, the plasma density is much lower, the plasma potential is higher, and the plasma is fainter/has much lower emission. As the input power to the discharge is increased, the plasma will eventually undergo a transition from the capacitive E mode to the inductive H mode. The transition is usually indicated by a dramatic increase in light emission and a much greater plasma density compared to that of the E mode. When the power deposited into the system by the inductively coupled current is larger then that contributed by the capacitive current, then the plasma is in the inductive H mode.

Hysteresis is usually observed when moving from H mode back into E mode, where the minimum input power required to sustain H mode is usually smaller than the threshold power required to bring about an E to H transition. This hysteretic behaviour arises due to the differences in the starting conditions of the two modes, such as the much larger plasma density observed in the inductive mode, and because of non-linearity in power coupling into the plasma and power dissipation from the discharge. The non linearity in the power transfer and dissipation is thought to be due to the presence of capacitive coupling in the plasma, even whilst the discharge is in H mode [26, 27]. However MH Lee and CW Chung [28] have reported an observation of inverse hysteresis when operating an argon ICP at low pressures. The normal pattern of hysteresis was seen at pressures of 80mTorr, but when the discharge was run in the 8-15mTorr range, the hysteresis became unclear and even at very low pressure the path of the hysteresis became inverted. They believed this behaviour was due to a transition from a bi-maxwellian electron energy distribution in the E mode to a maxwellian distribution in H mode, and that the conventional explanation of non linearities in power deposition and dissipation could not explain the observations at low pressure. The larger fraction of high energy electrons provides a greater ionisation efficiency when the plasma is in E mode. This results in a greater inductive coupling efficiency for the bi-maxwellian distribution, which allows the E-H transition at smaller coil currents and leads to the inverse hysteresis.

## 2.3 $H^-$ Production

Understanding the production of negative hydrogen ions in the plasma volume and on surfaces is essential in order to design and develop ion sources for the next generation of NBI systems. Negative ions are more easily ionised due to the additional electron occupying the atom's affinity level. The binding energy of this affinity level is quite small, 0.75eV [29], and the electron can be easily liberated. Whilst this makes negative ions useful for neutral beam applications this property also causes their reliable generation and extraction to be challenging, as the ions are easily destroyed/neutralised through several mechanisms.

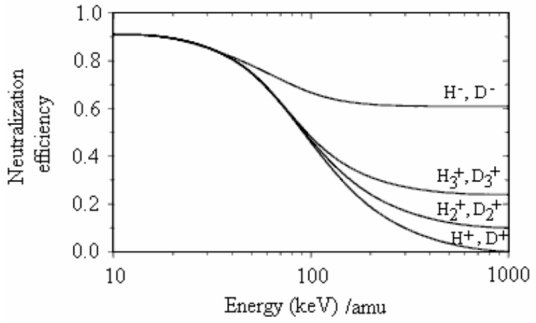


Figure 2.4: Neutralisation efficiency of H and D ions against energy. $H^-$ and $D^-$ ions must be for ITER's 1MeV NBI system [30].

At high beam energy positive ions are no longer a viable option for neutral beam heating due to the decreasing neutralisation cross section. Negative ion neutralisation cross section remains constant at high energies, as shown by figure 2.4. Whilst negative ions are much easier to neutralise compared to positive ions, they are much more difficult to produce and extract from the ion source, and plasmas with large numbers of negative ions have more complicated dynamics.

$H^-$ ions are mostly generated though two mechanisms: i) the dissociation of rotationally and vibrationally excited hydrogen molecules in the plasma volume

$$H(\nu'') + e^- \rightarrow H_2^- \rightarrow H^- + H; \tag{2.9}$$

and ii) through the backscattering of positive ions and neutrals as negative ions from low work

function surfaces.

$H^-$ ions are easily destroyed through several processes:

mutual neutralisation

$$H^- + H^+ \rightarrow 2H \tag{2.10}$$

$$H^- + H_2^+ \rightarrow H_2 + H \tag{2.11}$$

collisional detachment

$$H^- + e^- \rightarrow H + 2e^- \tag{2.12}$$

associative detachment

$$H^- + H \rightarrow H_2 + e^- \tag{2.13}$$

and photo-neutralisation

$$H^- + h\nu \rightarrow H + e^- \tag{2.14}$$

An understanding of the balance between these creation and loss mechanisms in the plasma is crucial in order to maximise the negative ion current extracted from the source. For example processes such as collisional detachment have a threshold electron energy, and through the reduction of electron temperature in the source the loss of ions can be effectively reduced.

Sections 2.3.1 and 2.3.2 discuss the volume and surface production mechanisms of $H^-$ ions in more detail

### 2.3.1 Volume Production

Volume production of negative hydrogen ions relies on the generation of rotationally and vibrationally excited hydrogen molecules either through $H_2$ collisions with electrons or H atom interactions with the chamber surfaces. The negative ion is then produced in through the dissociative attachment of electrons to rovibrationally excited molecules in the plasma volume. In the 1970s a large discrepancy was discovered between calculated and observed $H^-$ densities. The calculations were based on the production of negative ions through the dissociative attachment (DA) of low energy electrons to hydrogen molecules in their ground state, and dissociative recombination of positive molecular ions. It was later shown that the cross section for DA production of negative ions increased with rotational and vibrational excitation [31]. The vibrational energy levels in a hydrogen molecule form an anharmonic or Morse oscillator, where (in contrast to the harmonic oscillator) the energy separation between vibrational states decreases for increasing $\nu$, up to a dissociation energy. Each vibrational energy level then contains several rotational energy levels.

$$E_\nu = h\nu_0(\nu + \frac{1}{2}) - h\nu_0 x_e(\nu + \frac{1}{2})^2, \nu = 0, 1, 2... \tag{2.15}$$

Where $\nu$ is the vibrational energy level, $\nu_0$ is the harmonic frequency, and $x_e$ is the anharmonicity constant.

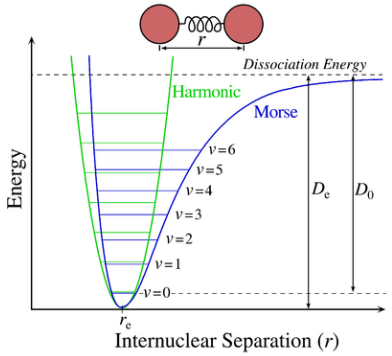


Figure 2.5: Vibrational levels of the Morse oscillator.

For a rotationless hydrogen molecule in the electronic ground state, the cross section for DA increases by around four orders of magnitude as the vibrational quantum number, $\nu''$, increases from

$\nu'' = 0$ to $\nu'' = 4$. This is due to an increased survival factor which results from the increased amplitude of vibrational motion and anharmonic stretching, allowing electrons to be captured at greater distances [32]. Increases in rotational excitation also result in an increased DA cross section, but does not have as great an effect as vibrational excitation for low values of rotational quantum number, $J$. Higher values of $J$ or increased rotational temperature have a more substantial effect on the DA cross section as shown by more recent calculations performed by Horacek *et al* [33].

Collisions with thermal electrons, e-V processes, excite molecules into the lower vibrationally excited states through an intermediate resonant $H_2^-$ state.

$$H(\nu'') + e^- \rightarrow H_2^- \rightarrow H(\nu'' + \Delta\nu) + e^- \tag{2.16}$$

Interactions with higher energy electrons (>20eV) proceed via E-V processes, in which molecules are excited to higher electronic singlet states. The excited state decays and some of the energy is retained as vibrational or rotational energy [34].

$$H_2(\nu'' = 0) + e^- \rightarrow H_2^*(B^1\Sigma_u, C^1\Pi_u) + e^- \tag{2.17}$$

$$H_2^*(B^1\Sigma_u, C^1\Pi_u) \rightarrow H_2(X^1\Sigma_g) + h\nu \tag{2.18}$$

E-V processes produce much more highly excited rovibrational states ($\nu$ = 5-14) [35]. Triplet electronic excitations dissociate and do not lead to molecular final states. The cross section for DA from the resulting $H_2(X^1\Sigma_g)$ state is large due to increased vibrational excitation and provides a large fraction of the negative ions generated through the DA process. However higher temperature, fast electrons are necessary for E-V excitation to higher vibrational levels. These higher temperature electrons also lead to an increased $H^-$ loss rate due to collisional detachment (equation 2.12) and a decreased DA rate, which has a maximum cross section close to 1eV.

This trade off between increased E-V excitation and decreased collisional detachment/DA cross section is a serious limitation for efficient volume production of negative hydrogen ions. To counter

this, current volume sources use magnetic or temporal filtering to maintain a high E-V excitation rate, whilst reducing collisional detachment losses. These concepts are discussed in sections 2.4 and 2.5 .

Inelastic Vibrational-Vibrational and Vibrational-Translational interactions also occur within the plasma where a high vibrationally excited molecule collides with a molecule with little or no rovibrational excitation and the resulting energy exchange alters the vibrational excitation of both molecules. The vibrational energy can also be converted into translational through collisions with other particles or chamber surfaces.

Caesium is often used in fusion negative ion sources. Gas phase Cs in the plasma volume affects the ionisation degree and EEDF of the plasma due to its low ionisation energy of 3.89eV [36]. The presence of Cs in the plasma should decrease electron temperatures and increase the dissociative attachment rates. Cs can also destroy vibrationally excited $H_2$ molecules through ionisation and attachment processes such as

$$Cs + H_2 \rightarrow CsH + H \tag{2.19}$$

which contribute to a decrease of the $H^-$ production rate.

Direct surface production of $H^-$ ions through backscattering of neutrals is discussed section 2.3.2, but surfaces in the plasma chamber can also affect rovibrational hydrogen molecule populations within the plasma volume. Hydrogen ions are physisorbed or chemisorbed onto surfaces in contact with the plasma. These H atoms can then thermally propagate along the surfaces where they can interact with other hydrogen atoms bound to the surface. This can result in the two H atoms leaving the surface as a $H_2$ molecule through recombinative desorption, with a probability for that molecule to be in an excited rovibrational state. Hydrogen atoms in the gas phase moving in close enough proximity to the surface collide/interact with a surface bound H atom, leaving the surface as a vibrationally excited molecule, through the Eiley-Rideal (ER), Langmuir-Hinshelwood (LW), and hot atom mechanisms. The desorbed molecule leaves the surface in an excited state due to the molecular bonding between H atoms being much stronger than the binding energy between the H atom on the surface. This strong H-H interaction can also cause the incident gas phase H atom

to be steered towards surface bound H atoms, and further increase the ER cross section [37]. The calculations of Jackson *et. al.* [38] showed that the cross section for ER interactions increased as the strength of the H atom - surface bond decreases. This results in much larger DA cross sections for carbon surfaces than for metallic surfaces, and that hot atom processes were more important for the recombinative desorption of excited $H_2$ molecules from metal surfaces. Surfaces can also assist with production of vibrationally excited molecules through recombination of ions on the chamber surfaces,

$$H^+ + H^- + S \rightarrow H_2(\nu'') \tag{2.20}$$

and through Auger de-excitation processes

$$H_2(^3\Pi_u) \rightarrow H_2(\nu'') \tag{2.21}$$

Calculations by Amorim *et. al.* [39] suggested that the production of vibrationally excited molecules through recombinative wall desorption is an important $H^-$ formation mechanism, as highly excited ($\nu = 10, 11$) molecules populate vibrational levels through V-V interactions. Surface processes provide the largest contribution to high J states, as electron excitation of rotational levels is inefficient.

Vankan [40] measured the rovibrational distribution using vacuum UV multiplexed laser induced fluorescence and stimulated anti-stokes Raman scattering and provided evidence that the relative populations of higher rovibrational states suggest a Boltzmann distribution with a temperature far greater than that of lower excited states. Gabriel *et. al.* [41] also observed a similar temperature distribution for low and high vibrational states. Lower rotational excitations (J<5) were populated by a Boltzmann distribution at ambient temperature but higher levels were extremely overpopulated, for example an overpopulation of over seven orders of magnitude was measured for $\nu$=2 [42]. These rotational distributions are similar for almost all vibrational levels until close to the dissociation energy of the $H_2$ molecule. Vankan suggests that recombinative desorption of hydrogen molecules from a surface provides an explanation for the temperature distribution of rotationally excited states, and that the results agree qualitatively with those of Rettner *et. al.* [43], who

measured the rotational distribution of $H_2$ molecules forming on a copper surface at 925K. They found the vibrational populations for $\nu$=1 ($H_2(\nu = 1)/H_2(\nu = 0)$) were enhanced by a factor of 18 compared to populations associated with a surface temperature of 925K, with similar deviations for $\nu$=0.

The attachment of electrons to high Rydberg state molecules has also been suggested [44] to explain differences in measured and predicted $H^-$ densities (equation 2.22). Hiskes [45] suggested that the highly excited Rydberg state molecules made only a negligible contribution to the negative ion density (1% or less).

$$H_2^R + e \rightarrow H^- + H^R \tag{2.22}$$

Pinnaduwage *et. al.* [46] however argue that the long lived Rydberg state molecules exist in significant densities in the discharge, and the subsequent DA provides a substantial contribution to negative ion production. Amorim *et. al.* [39] calculations also show that the $H^-$ to $H_2$ ratio increases when including $H^-$ production through DA of high Rydberg state $H_2$ molecules.

An isotopic effect was observed for the DA cross section value between hydrogen and deuterium molecules in the 60s [47, 48]. Low energy DA processes showed a decrease in the cross section for $D^-$ from $D_2$ of two orders of magnitude compared to $H^-$ production from $H_2$. The time of dissociation increases for $D_2$ molecules leading to a decrease in DA cross section [49]; heavier molecules also have a decreased survival probability.

### 2.3.2 Surface Production

The other main negative ion production process is upon the surfaces, where low work function surfaces in contact with the plasma can be observed to generate a current of H− ions. In the 70s Belchenko *et. al.* [50] demonstrated that the negative ion current extracted from a surface plasma source depended on the cathode material used and the use of Caesium vapour inside the chamber. The Cs vapour lowered the work function of the surface ($\phi$), and a large increase in the extracted negative ion current was observed. The work of Varbeek *et. al.* [51] also showed increasing negative

ion currents for materials with decreasing work functions.

The surface ionisation mechanism is the tunneling of an electron from a surface energy level to the affinity level ($E_A$) of a hydrogen atom moving away from the surface [52]. The atom interacts with an image potential when moving lose to the surface. This interaction causes the affinity level of the atom to decrease and broaden. When the atom is close enough to a surface with a low work function, such as a Cs coated surface, the affinity level of the atom will fall below the work function of the surface and overlap with electron energy levels of the surface. There is then a probability that an electron occupying one of these energy states will tunnel across to the atom's affinity level through resonant charge transfer and remain there as the atom moves away, resulting in a negative ion. Figure 2.6 depicts the perturbation of the atom's affinity level as it approaches a surface.

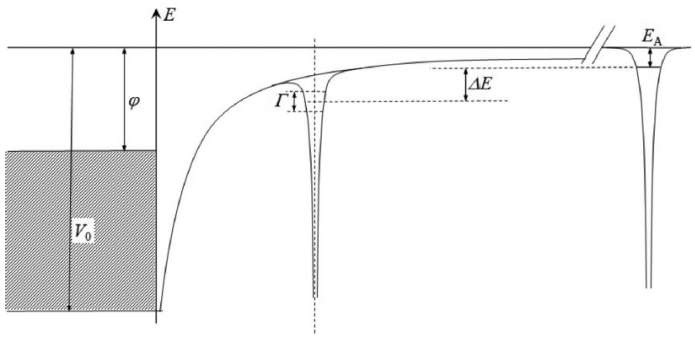


Figure 2.6: Interaction with the induced image potential shifts and broadens the hydrogen atom's affinity energy level. The affinity level overlaps with occupied electronic states in the surface, allowing electrons to tunnel across [53].

$H^+$ ions approaching the surface are initially neutralised through an Auger transition of an electron from the surface, before then acquiring a second electron as the affinity level is modified by the image potential. Incident molecules are neutralised and dissociated as they approach the surface. The hydrogen atom can be ionised due to backscattering from the surface or as they are desorbed from the surface. As the negative ion leaves the surface and the affinity level becomes greater than the Fermi level of the material, the ion can be destroyed as the electron tunnels back to an unoccupied energy state. Verbeek *et. al.* [54] scattered 5keV beams of H atoms from surfaces, their results suggesting that the probability for production of $H^-$ decreased with higher velocities, whilst the destruction probability decreased for higher energy backscattered ions. This is generally what

one would expect as each process requires some finite interaction time.

The potential difference between the plasma and the surface is important when considering the ion yield from surface production. When the surface potential $V_b$ is less than plasma potential $V_p$, positive ions from the plasma volume are accelerated toward the surface where they are converted into negative ions and repelled from the surface back into the plasma bulk. This increases the negative ion yield and the average energy the ions carry back into the plasma. As the surface bias is brought closer to $V_p$ the positive ions reach the surface with less energy, and the negative ions produced also carry less energy. At some $V_b$ the negative ions will no longer have enough energy to move back through the sheath and in to the plasma volume. For incident neutral particles, the potential at which negative ions can longer escape the surface is given by [55]

$$E_{in}\left(\frac{R_E}{R_N}\right) - E_{thr} \leq e(V_b - V_p), \tag{2.23}$$

where $E_{thr}$ is the minimum energy required for the formation of a negative ion

$$E_{thr} = \phi - E_A, \tag{2.24}$$

$E_{in}$ is the energy of the incoming particle, $R_E$ is the energy reflection coefficient, and $R_N$ is the particle reflection coefficient. Equation 2.23 is modified slightly for incident ions,

$$(E_{ion}(R_E/R_N) - E_{thr})/(1 + (R_E/R_N)) \leq e(V_b - V_p). \tag{2.25}$$

Molecular ions dissociate during interactions with the surface and the subsequent ions are then neutralised, yielding larger quantities of negative ions. Calculations of negative ion fluxes from the surface by Wunderlich *et. al.* [56] and McAdams *et. al.* [57] suggest that the maximum negative ion flux away from the surface is space charge limited by the formation of a virtual cathode between the surface and the plasma sheath. This virtual cathode provides a potential barrier for negative ions leaving the surface, and also decelerates positive ions moving toward the surface after they reach the potential minimum. The virtual cathode provides a fundamental limit to the maximum extractable

negative ion current from a surface, and also implies that a increased positive ion density/flux to the walls would increase this maximum current.

In addition to negative ion formation through the ionisation and reflection of incident particles, surface $H^-$ production can also occur through desorption of atoms from the surface. Schiesko *et. al.* [58] studied $H^-$ and $D^-$ production on graphite, and attribute the main peak of the ion energy distribution to a superposition of this atom desorption process and the backscattering mechanism. Backscattering of incident positive ions as negative ions is responsible for the high energy tail of the distribution. An Isotopic effect is also observed for the energy of backscattered H and D ions, which is thought to be due to the difference in mass leading to an increased maximum energy transfer between ions/atoms and the surface.

A kinetic resonance also plays a role as the production of negative ions dependent on the velocity component of the incident particle parallel to the surface [59]. In the rest frame of the ion/atom moving parallel to the surface, the occupation of the electronic states is given by a Doppler-Fermi-Dirac distribution. The neutralisation/ionisation of ions/atoms has a dependence on the parallel velocity component.

The surface production of ions from Caesiated surfaces has a much greater yield compared to $H^-$ production through dissociative attachment of rovibrationally excited molecules. ITER NBI test ion sources all use the magnetic filter concept along with caesium evaporation for enhanced $H^-$ surface production, because the ITER requirements for extracted current and co-extracted electron ratio can only be met by using surface $H^-$ production [60]. This conclusion has caused negative ion sources for fusion applications to be designed for optimal production of ions on their Caesiated plasma grids close to the extraction system for a maximum probability of extraction from the source. However the consensus is that the use of Caesiated ion sources in tokamak NBIs after ITER will not be possible. The next section discusses some alternatives to Cs which are currently being considered for use in these future magnetic confinement fusion reactors.

## 2.4 Magnetically Filtered Sources

As discussed in the previous section, the high energy electrons required for E-V excitation of $H_2$ molecules are also responsible for the neutralisation of the $H^-$ ions through collisional detachment. The cross section for DA production of negative ions is also greater for lower energy electrons. One technique developed to address the loss of $H^-$ ions is to use a magnetic filter field in the plasma source. Generally there are two types of magnetically filtered sources: tandem and hybrid sources.

Permanent magnets are used to create a magnetic field across the plasma volume, as shown in figure 2.7 . The field separates the sources into two regions: the driver and the extractor. In the driver region highly vibrationally excited hydrogen molecules are produced through E-V interactions due to the high fast electron population. Subsequently there is an increased rate of $H^-$ losses and lower DA rate. The magnetic field then acts as a filter for the high temperature electrons in the discharge as they cannot easily pass through the filter due to their larger Hall parameter/Lamor radius. High energy electrons lose energy through collisions whilst trapped inside the magnetic field. Low energy electrons, neutral atoms and molecules, and ions pass through the filter into the extraction region.

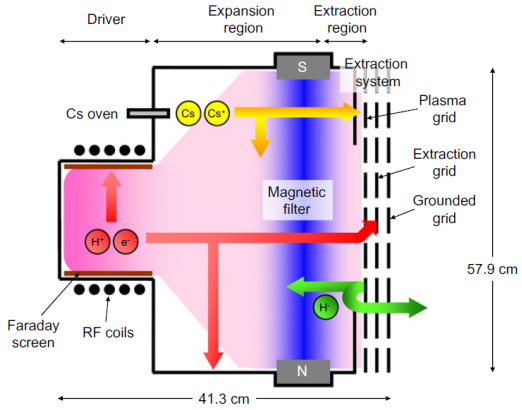


Figure 2.7: IPP Negative Ion Source

Electron temperatures are lower in the extractor region, resulting in a larger DA cross section and reduced collisional detachment of $H^-$ ions. Negative hydrogen ions can be produced and extracted much more efficiently with a reduced co-extracted electron current (Essential for decreased extractor grid and ion dump heat loads for fusion NBIs). $H^-$ production does take place in the driver

region, but survival probabilities are much smaller than for ions formed in the extraction region. Simulations by Boeuf *et. al.* [61, 62] show that an "ideal" magnetic filter is very effective at limiting the electron current into the extraction region of the source, even for small magnetic field strengths. This current increases with grid bias until it saturates at the plasma potential. However in reality instabilities arising from presence of the walls and $E \times B$ drifts lead to an increase in higher energy electron drift.

Leung and Bacal [63] found using a positively biased electrode in the extraction region of the source enhanced the extracted $H^-$ current whilst reducing the co extracted electron current. Small magnetic fields in front of the plasma electrode (PE) reduce electron transport, and the positive bias of the PE collects electrons that are able to move across the field. This enhances the negative ion current as negative ions must compensate for the depleted electron density to maintain quasineutrality, and are not affected by the magnetic field.

## 2.5 Temporally Filtered Sources

Temporally filtered plasma sources have been used for efficient negative ion generation for both fusion [64, 65] and non fusion neutral beams [66, 67, 68]. By pulsing the input power to the plasma, and varying the duty cycle (power on to power off fraction for each pulse), the discharge and afterglow can be tailored to optimise negative ion production and extraction.

The lifetimes of rovibrationally excited molecules in the afterglow phase are much greater then that of the high energy electrons. The high energy tail of the electron energy distribution (EEDF) rapidly decays in $1\mu$s due to the short confinement time of fast electrons, and the average electron temperature falls. The lifetimes of vibrationally excited molecules and low energy/thermal electrons are significantly longer. Hopkins *et. al.* [69] found that after $50\mu$s the EEDF temperature had cooled to 0.4eV. The electron density had not decreased significantly, but the high energy tail had been removed.

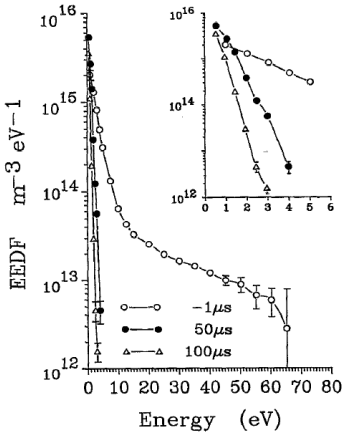


Figure 2.8: EEDF measured during the discharge (1$\mu$s), and during the afterglow (50 and 100$\mu$s) [69].

Negative ion production continues into the post discharge, with reduced collisional detachment losses from decreased fast electron populations. The rovibrationally excited molecules are generated in the plasma volume during the "on" phase, then ions are produced and extracted during the afterglow phase. The reduced electron temperature increases the lifetime of negative ions produced during the afterglow phase of the plasma, and with the increased survival probability a greater ion current can be extracted than from conventional continuous operation $H^-$ sources. A larger population of low energy electrons also increases the rate of DA interactions due to a larger cross section for thermal electrons. Temporally filtered sources should operate more efficiently at lower temperatures as the increased fast electron density and E-V excitation rate should result in larger $H^-$ currents in the afterglow.

The pulsed nature of the plasma leads to a time averaged rovibrational population, which can be modified by varying the pulse duty cycle. Through modulation of the discharge time the time average loss rates of rovibrationally excited hydrogen are lower compared to the continuous operation rates, whilst production of vibrationally excited molecules remains proportional to the plasma discharge current.

$$< n >= N_c \left(1 + \frac{t_{off}\tau_{on}}{t_{on}\tau_{off}}\right) \tag{2.26}$$

The time averaged $H_2(\nu")$ population can approach the steady state rovibrational population, as shown by equation 2.26 [64], if the frequency of the pulse is chosen such that the second term goes to zero, where $\tau_{on}$ and $\tau_{off}$ represent the lifetime of $H_2(\nu")$ particles when the discharge is on and off, and $t_{on}/t_{off}$ are the time periods for which the plasma is on or off during each pulse. The vibrationally excited populations would be equivalent to the steady state, with reduced collisional detachment losses in the afterglow phase.

The decrease of the electron to negative ion fraction in the afterglow phase of the discharge also assists with the extraction of $H^-$ ions. In a discharge with a high electron to negative ion ratio, the electrons will have a higher temperature and escape to the walls of the chamber much more easily. This leaves a region of positive space charge, and the resulting potential well prevents the negative ions from escaping [70]. In a pulsed discharge the decreased electron to $H^-$ ratio and the lower average electron temperature reduce the sheath potential and allow more negative ions to escape to the chamber walls for extraction.

### 2.5.1 Pulsed Plasma Dynamics

Time modulated plasmas [71, 6] have been studied since the 1980s, where they were used to study fundamentals of plasma physics as well investigated for their use in plasma etching of semiconductor devices. It was found that pulsed plasmas demonstrated the ability to solve some of the typical problems associated with continuous wave (CW) plasma etching.

Some plasma induced damage (PID) examples are: Physical damage to the substrate surface due to ion bombardment; UV damage; plasma spatial non-uniformity leading to non-uniform potential on the wafer; and differential charging of high aspect ratio etch patterns which leads to charge build up and undercutting of feature walls. As the etching feature sizes become smaller (10nm and below), these damage mechanisms become increasingly important, and development of plasma etching devices capable of reducing PID issues and controlling etching performance at these

Pulsed plasmas can help mitigate these problems, as collapse of the plasma potential and the electrostatic field within the plasma during the afterglow allows (discussed below) for a larger angular distribution of ion trajectories which can help reduce charge imbalances on the wafer

[72, 66]. They also can reduce the UV radiation dose to wafers [73], and allow some control of the ion energy distribution function (IEDF) to operate at lower ion energies [72, 66, 74]. The ability to extract negative ions (if present in the plasma) during the afterglow of the pulse (again, discussed below) also provides a potential solution to charge build up/differential charging problems.

One potential downside to the use of pulsed plasmas is that the power matching of the RF into the plasma can be worse than CW devices. This is mainly due to the fact that the plasma impedance varies rapidly with time within the pulse, which can be difficult for matching units to follow.

The time evolution of the pulsed plasma can be divided into the activeglow, when RF power is being deposited into the plasma, and the afterglow, where the power is switched off and the plasma density and temperature decays away over time.

### 2.5.2 Plasma Activeglow

Figure 2.9 shows the evolution of charged species in a pulsed chlorine ICP model. In the early stages of the RF power pulse, there is only a small population of free electrons present in the system after the decay of the previous pulse. The RF power is absorbed by this small number of electrons, which causes a large peak in the electron temperature [75, 76], often larger than the steady state value of $T_e$. Increasing $T_e$ leads to ionisation and increasing positive ion densities.

Assuming that ion electron pairs are created through ionising electron collisions with background neutrals and that all particles are lost by diffusion to the chamber walls, the electron particle balance equation for electropositive plasmas is

$$\frac{1}{n_e}\frac{dn_e}{dt} = \nu_{iz} - \nu_{loss} \tag{2.27}$$

where $n_e$ is the electron density, $\nu_{iz}$ is the ionisation rate, $\nu_{loss} = u_B/d_{eff}$ is the loss rate to the walls, and $d_{eff} = V/A_{eff}$, V being the discharge volume and $A_{eff}$ is the effective area for particle loss. The power balance is a combination of the collisional energy loss rate in the plasma volume and the power lost to the walls through the kinetic energies of lost ions and electrons. The collisional energy loss is given by

$$P_c = en_e n_g V \Sigma K_i \varepsilon_i, \tag{2.28}$$

$K_i/\varepsilon_i$ represent the rate constant/energy loss per excitation, ionisation, and elastic collision interactions. Kinetic energy losses to the walls are given by

$$P_i = e(V_s + \frac{1}{2}T_e)n_e u_B A_{eff} \tag{2.29}$$

for ions, and

$$P_i = 2eT_e n_e u_B A_{eff} \tag{2.30}$$

for electrons. $V_s$ is the sheath potential at the walls. Combining yields the power balance equation

$$P_c = \left[\frac{d}{dt}\left(\frac{3}{2}en_e T_e\right) + en_e n_g V \Sigma K_i \varepsilon_i\right] V + e\left(V_s + \frac{5}{2}T_e\right) n_e u_B A_{eff} \tag{2.31}$$

Now by using the particle balance given by equation 2.27 to remove $dn_e/dt$ give the evolution of the electron temperature

$$\frac{1}{T_e}\frac{dT_e}{dt} = \frac{P_{abs}(t)}{W_e} - \left(\frac{2\varepsilon_c}{3T_e + 1}\right)\nu_{iz} - \left(\frac{2}{3}\frac{V_s + 5/2T_e}{T_e} - 1\right)\nu_{loss} \tag{2.32}$$

Here $\varepsilon_c$ is the all of the collisional energy losses combined, and $W_e = \frac{3}{2}en_e T_e V$ is the plasma energy. During the early stages of the activeglow, there is little to no particle losses (i.e. $\nu_{loss} = 0$) and an charged species are produced through ionisation. Using equations 2.27 and 2.32 we find the evolution of the plasma density

$$\frac{1}{n_e}\frac{dn_e}{dt} = \nu_{iz} \tag{2.33}$$

and the electron temperature

$$\frac{1}{T_e}\frac{dT_e}{dt} = \frac{P_{abs}(t)}{W_e} - \left(\frac{2\varepsilon_c}{3T_e} + 1\right)\nu_{iz} \tag{2.34}$$

Equation 2.33 shows that initially the plasma density increases steadily at a rate proportional to the ionisation rate constant (a function of $T_e$). $\nu_{iz}$ is small due to the low electron temperature at the start of the pulse cycle, causing the density increase and the second term in equation 2.34 to also be small. This means that the rate of increase of $T_e$ is dominated by the first term in equation 2.34 and leads to a rapid growth in $T_e$. The electron temperature increases much more rapidly than the plasma density [77, 78].

During the spike in the electron temperature, mobility of electrons and the strength of the electrostatic/ambipolar field increases. From the fluid equation of motion for an isothermal plasma in steady state, the velocity of a particle species in the plasma is given by

$$\mathbf{v} = \frac{1}{nm\nu}(\pm en\mathbf{E} - k_B T\nabla n) \tag{2.35}$$

Defining the diffusion coefficient, $D = k_B T/m\nu$, and the mobility of the species, $\mu = |q|/m\nu$, equation 2.35 then becomes

$$\Gamma = n\mathbf{v} = \pm\mu n\mathbf{E} - D\nabla n \tag{2.36}$$

The ambipolar field can be found by using the criterion that the plasma must be quasineutral, i.e. that there cannot be a net flow of charge within the plasma bulk, $\Gamma_i - \Gamma_e - \Gamma_n = 0$, where the subscripts i,e, and n correspond to ions, electrons, and negative ions (for electronegative plasmas) respectively. Using positive ions and electrons, $\Gamma_i - \Gamma_e = 0$, and equation 2.36, the ambipolar electric field is

$$\mathbf{E} = \frac{D_i - D_e}{\mu_i + \mu_e}\frac{\nabla n}{n} \tag{2.37}$$

During the initial stages of the plasma activeglow, the spike in $T_e$ leads to a high plasma potential

and high energy ions incident to the walls/any substrate present in the discharge. Ambipolar diffusion of electrons and ions to the walls of the discharge causes stratification of the negative ion population remaining from the previous pulse drift towards and be confined to the core of the plasma [79, 80, 81]. During this phase of the pulse negative ion populations are small due to the electron detachment losses, but negative ion fluxes to the walls are very small due to the confining field so the population slowly increases [82].

Eventually $T_e$ decreases, and the plasma achieves a quasi-steadystate for the duration of the RF pulse. The final values of the electron temperature, electron density, ion density, and plasma potential should be similar to that of a CW plasma. However this may not necessarily be true for pulsed plasmas with a large afterglow period (low duty factor) or which operate at high frequency, as the plasma cannot achieve the quasi-steady state phase.

### 2.5.3 Afterglow

As the input RF power stops, electrons continue to lose their energy through the usual ambipolar diffusion to the walls and in the early afterglow through inelastic collisions with neutral species. The energy loss manifests as a rapid decrease in the electron temperature. The decrease in $T_e$ is eventually slowed down by the energy of the electrons falling below the minimum threshold energy for inelastic processes, after which the electrons lose energy at a slower rate through elastic collisions and continued diffusion to the walls. The electron density falls away during the afterglow as ionisation processes stop, and electrons are lost to the walls and attachment to ions. Eventually the decrease of $n_E$ and $T_E$ leads to the loss of the electrostatic field within the plasma, which allows the negative ion population confined to the core to diffuse out into the plasma bulk.

The lower electron temperature also increases the population of negative ions in the plasma volume. During the activeglow phase of the RF power pulse the high temperature electrons populate high rovibrationally excited states through E-V interactions. Then during the plasma afterglow the low energy electrons have a greater cross section for negative ion production through dissociative attachment [74]. A reduced collisional detachment rate for negative ions in the afterglow also contributes to a peak in the negative ion density during the afterglow. Attachment rates eventually

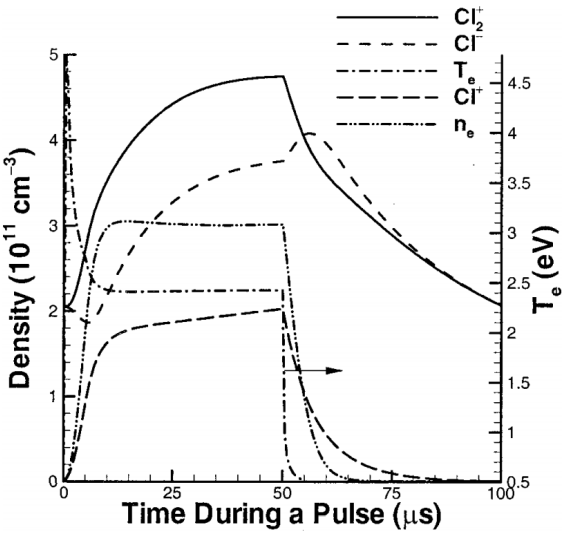


Figure 2.9: Evolution of $T_e$, electron and ion densities in a simulated 10kHz 50% df Chlorine ICP discharge in a GEC reference cell [82].

plateau and then decrease as the electron population is depleted.

As the electrons are lost and the negative ion population increases (the plasma becomes increasingly electronegative), an ion-ion plasma can form in the late stages of the afterglow (figure 2.9) The ambipolar electron diffusivity is given by

$$D_{ae} \approx \left[\frac{1+2(n_n/n_e)}{((\mu_e/\mu_n)+1)+2(n_n/n_e)}\right] D_e \tag{2.38}$$

Where $D_e$ is the free electron diffusivity [81]. Equation 2.38 implies that as the electronegativity of the plasma $(n_n/n_e)$ increases, the ambipolar diffusivity tends towards the value of $D_e$. In the ion-ion plasma the negative ions are the dominant negative charge carrier in the discharge. Therefore during the late afterglow of an electronegative plasma, $n_n \gg n_e$, the electrons diffuse freely to the walls ($D_{ae} \approx D_e$), and the ambipolar field between positive and negative ions is given by

$$\mathbf{E} = \frac{D_i - D_n}{\mu_i + \mu_n}\frac{\nabla n}{n}. \tag{2.39}$$

This field vanishes if the diffusivity of the positive and negative ions are approximately equal,

$D_i \approx D_n$, and all species in the plasma diffuse freely.The positive and negative ion populations then decay through diffusion and recombination/mutual neutralisation processes until the start of the next RF pulse. At this stage the negative ions are able to move away from the core and be extracted from the plasma. Though if the product of the negative ion diffusion time and the detachment frequency is greater than 2 ($\gamma_d\tau_d>2$), ions are converted into electrons leading to a new electric field in the late afterglow which restricts negative ion diffusion out of the plasma (self trapping). However when $\gamma_d\tau_d<2$, negative ions can escape and the eventually the positive and negative ion fluxes to the walls are equal [83, 84, 85]

For electropositive discharges, the analytical expressions representing the decay of the electron temperature and plasma density during the afterglow are [78]

$$T_e(t) \approx T_{e\infty} \left(1 + 2\nu_\infty (t - \alpha\tau)\right)^{-2}, \tag{2.40}$$

and

$$n_e(t) \approx n_{emax} \left(1 + 2\nu_\infty (t - \alpha\tau)\right)^{-1/2}, \tag{2.41}$$

respectively. $\tau$ is the pulse period, $\alpha$ the duty cycle, $T_{e\infty}$ is the electron temperature in the steady state, and $n_{emax}$ is the electron density at the end of the activeglow period.

The final value to which the plasma density falls to generally depends on the plasma pulse frequency and the duty cycle of the pulse. For large duty factors or high frequency pulsing, there is not enough time during the short afterglow for the plasma to decay away significantly. Due to the formation of negative ions in the afterglow, the rate of electron loss is greater for electronegative discharges compared to electropositive. The electron density at the end of the afterglow is therefore much smaller. This leads to a much more pronounced overshoot of the electron temperature at the beginning of the activeglow, especially for lower pulse duty cycles.

### 2.5.4 Grid Biasing in Time Modulated Plasmas

The ability to control the pulse frequency, duty factor, and biasing of the plasma also allows much more control of the EEDF compared to that of CW plasmas. Longer afterglow periods have much lower plasma density and electron temperatures, which leads to a greater peak in the electron temperature during the early activeglow and modifies the high energy tail of the EEDF. Bi-maxwellian EEDFs typical of ICPs also can become maxwellian during the afterglow. A bias on the target substrate/extraction grid can be applied in order to modify the IEDF of the ions which are incident onto the surface. The biasing system can be set up with a continuous substrate/grid bias with a time modulated plasma; a time modulated bias in a CW plasma; or synchronised pulsing of the RF power and the bias applied to the grid.

The presence of a substrate/extraction grid bias within the plasma can significantly affect the dynamics of particle species during the plasma afterglow. When a continuous RF bias is applied, the activeglow and early afterglow periods of the plasma generally remain unaffected by the bias. Ion Energy distributions will typically have a bimodal structure in the presence of an RF bias [86], with each peak corresponding to the maximum and minimum voltage applied during the biasing cycle. if the ratio of the ion transit time through the sheath to the period of the biasing waveform

$$\frac{\tau_i}{\tau}. \tag{2.42}$$

is small, then the ions are accelerated by the instantaneous voltage across the sheath and the resulting distribution is broad. As this ratio increases, the distribution width decreases until it becomes a single peak as the ions only react to a time averaged sheath potential.

It was found that during the late afterglow, after $T_e$ and $n_e$ had mostly decayed, the electron temperature began to increase again. This is thought to be due to heating of the electrons by the capacitively coupled oscillating bias applied to the extraction grid (reactive ion etching mode). Electron temperatures increased back to as high as 7eV. For longer afterglow periods, the densities of the plasma also began to increase again [87, 88]

For electronegative plasmas this capacitive heating of the electrons in the late afterglow essentially

means that the plasma potential cannot decay away/collapse, which means that negative ions remain trapped within the plasma bulk and are unable to reach the extraction grid. Synchronous RF gird bias pulsing can increase the time it takes for capacitive heating of the electrons in the afterglow to take effect, and makes the extraction of negative ions possible. However as bias amplitude is increased, the negative ion current is reduced as the capacitive heating mode arises more rapidly.The affect of source pulsing is to modify the average plasma parameters (density, $T_e$, etc), whilst the bias pulsing alters the features of the extracted ion energy and angular distributions. Altering the phase between the RF pulse and grid bias allows some control over these parameters.

Banna *et. al.* [89] investigated a pulsed ICP with synchronous RF substrate biasing. The plasma potential drop was more pronounced during the afterglow compared to a pulsed plasma with CW RF biasing applied to the substrate, which is due to the biasing power to the substrate being shut off during the afterglow. When the biasing power and RF power are not completely in phase with each other, the electron temperature varied by around 10% with the lowest temperature measured with a 180 degree phase lag between RF and biasing. A similar result is found for the effect of the phase lag on the ion density, with no phase difference yielding the highest densities and $180^o$ the lowest. The effect of the phase lag on the plasma potential was much more significant, where all three phase differences (90,180,270) had plasma potentials of around 10V at the end of the afterglow compared to less than 5V for no phase difference. They conclude this shows that the plasma potential can be controlled through variation of the phase lag between RF power and bias power to the substrate.

DC biases applied to the substrate or extraction system during the activeglow causes a shift in the plasma potential in order to maintain quasineutrality in the plasma bulk. Application of a bias during the activeglow of the plasma leads to a ion energy distribution with two peaks: a narrow afterglow peak at low energies and a broad higher energy peak corresponding to a distribution of ions accelerated towards the substrate when the input power is on. A synchronous DC bias on the extraction grid during the late afterglow, when $T_e$ and $n_e$ are low, prevents acceleration of ions during the activeglow and reduces the energy of the broad peak. Shin *et. al.*. [90] investigated IEDFs using an retarding field energy analyser in an argon ICP with a biasable backing electrode, and found that the separation of the IEDF peaks can be modified by adjusting the pressure of the

gas (which affects $T_e$ and the plasma potential), and the DC bias, which alters the locations of the broad and narrow peaks respectively. Higher pressure discharges have a lower electron temperature and as a result the broader peak shifts to lower energies. They also investigated the effect of the time during the afterglow at which the DC bias was applied, and the length of time the electrode was biased. Biasing during the early afterglow (When the electron temperature is still relatively high) leads to broader extraction peak in the IEDF. The reduction in $T_e$ during the afterglow decreases the width of the high energy peak. Later in the afterglow when the rate of $T_e$ reduction is much lower, the timing of electrode bias has little effect on the width of the high energy peak. However if the biasing time is long compared to the characteristic decay time of $T_e$ the time at which biasing starts in the afterglow has little effect on the resulting distribution, as the average $T_e$ will be low. Xu *et. al.* [91] reported a nearly mono-energetic ion beam using a synchronous DC bias in a pulsed argon CCP. A ring electrode was used to filter out the broad peak of higher energy ions to leave a single narrow peak of ions extracted from the afterglow of the plasma, with FWHM of the peaks increasing with applied bias. Even at 100V biasing the FWHM of the peak was 3.4eV.

## 2.6 Beyond ITER/DEMO & Cs free $H^-$ Production

Caesium is distributed into the ion source usually through Cs ovens which heat a reservoir of elemental Cs (greater than 99% pure) in order to produce a flux of Cs vapour. The tubing transporting the Cs is also maintained at a high temperature to prevent build up of Cs on surfaces. Ion sources which make use of Cs have to go through an extensive conditioning phase, during which Cs is evaporated onto the source surfaces until the optimum surface work function of the plasma grid is achieved. In reality this optimum work function is difficult to achieve and often the temperature of the plasma grid surface itself also needs to be varied until the minimum is established. Cs is usually evaporated into the ion source during operation as the plasma will remove Cs accumulated on surfaces through sputtering and to apply new layers to walls in order to cover impurities.

Caesiated ion sources will be used for the ITER reactor, but will most likely not be a viable option for DEMO and future commercial reactors. ITER itself will evaporate Cs into its ion sources at an estimated rate of around 20mg/h. This roughly translates into around 18 months of usage before the

Cs ovens will have to be replaced, which is the expected length of the average ITER experimental campaign. However for a steady state fusion power plant such DEMO, Hemsworth and Boilson [92] reported that a demonstration reactor with a similar CS consumption rate to ITER will use more than 1kg of Cs every six years of operation. Since most of the Cs evaporated into the ion source remains there, this significant usage/build up of Cs in the source will lead to problems in ion source or NBI operation. Cs ovens must be replaced during the lifetime of the reactor, and with significant build up of Cs over time the ion source and accelerator components will have to be cleaned or replaced during the reactors lifetime. Replacement of components will be costly, whilst cleaning would be very difficult due to limited access to the beamline during operation and would have to be performed remotely. The other solutions are to reduce the rate of Cs consumption by around a factor of 20 compared to the operation of ITER's NBI, or to use/develop alternative materials to Cs.

The presence of Cs in the plasma itself can contribute to increased erosion of the ion source backplate due to backscattering ions in the NBI system. As negative ions are accelerated forward to the required 1MeV energy they collide with neutral gas present throughout the acceleration grids. Some of these atoms are ionised, which generates a flux of positive ions accelerated back into the ion source. Some of these ions are able to reach the backplate where they sputter and erode the wall material. It has also been observed [93] that the presence of caesium in the plasma discharge leads to increased beam halo effects (ions in the extracted beam with much larger divergences than the main beam). Caesium contamination can also lead to breakdowns/arching in components such as the acceleration system, and could act as a high Z impurity in the fusion plasma.

NBI sources for DEMO and commercial fusion reactors must be able to produce reliable, high current $H^-$ and $D^-$ beams with a heavily reduced Cs consumption rate or without the use of Cs to enhance surface production on the plasma grid to ensure the price of electricity generated is competitive with electricity costs of alternative sources.

### 2.6.1 Carbon Based Alternatives

Carbon materials have so far shown to be promising candidates for caesium alternatives, demonstrating increased negative ion yields, and for some diamond based surfaces show little to no hydrogen retention after exposure to the plasma. Diamond, diamond-like carbon (DLC), graphite, highly orientated pyrolytic graphite (HOPG), and other carbon based materials are being considered as potential candidates for use on the ion source plasma grid and other plasma facing materials such as tokamak divertors.

Carbon has a greater work function than Cs and so will fundamentally have a smaller probability of electron transfer to backscattered atoms. Ion beam scattering experiments on graphite [94], polycrystalline diamond [95], and diamond-like carbon [96] have demonstrated high yields of negative hydrogen ions from high workfunction surfaces. This suggests that the charge exchange process occurs through a different channel to resonant electron transfer of low workfunction materials. Insulating surfaces have large bandgaps and are unable to neutralise negative ions formed on the surface as there are no empty states available for the electron to occupy. There also appears to be no kinetic resonance for carbon materials as the negative ion fraction has little dependence on the the ongoing trajectory of the particle, which is in contrast to both caesiated and non-caesiated metallic surfaces [97, 95, 98, 99]. Gleeson and Kleyn [98] also observed that the addition of Cs to a HOPG surface does not show a comparable increase in the negative ions produced from the surface. These features of negative ion production of carbon surfaces suggest that conventional theories of surface charge exchange are not applicable. Differences in negative ion yields from different forms of carbon provide evidence that the charge exchange process is dependent on the electronic structure of the carbon surface used [99].

Carbon type and operating temperature play an important role in the negative ion yield of the surface. Ahmad *et. al.* [100] found that though the shape of the negative ion distribution function (NIDF) was similar for each form of carbon, the intensity of the NIDF differed between materials. At room temperature HOPG produced the greatest yield of $H^-$, greater than that of DLC, boron doped diamond (BDD), nano-crystalline diamond (NCD), and ultra nano-crystalline diamond (uNCD). At higher temperatures the NIDFs remained similar to room temperature for BDD, NCD, and uNCD, but the HOPG NIDF changes due to a much smaller sputtering contribution as the hydrogen sub

surface content has decreased [58]. BDD demonstrated the greatest negative ion yield at 400°C [101]. Changes in NIDFs are attributed to the modification of the sp3/sp2 ratio of the surface and the hydrogen surface coverage. When increasing the temperature the sp3/sp2 ratio increases for diamond materials and decreases for HOPG, which follows the same trend as the negative ion yield. They suggest that the increased ionisation efficiency of the material could be due to an increase of the hydrogen sub-surface content, which could be explained by a change in the sub-surface structure and the sp3/sp2 ratio as the temperature increases. Material temperature has a seemingly negligible effect on the ion contribution from backscattering [102]. Scheer *et. al.* [96] measured negative ion production on tetrahedral amorphous carbon (ta-C) films using molecular hydrogen ions at grazing incidence; the electron transfer probability is increased by hydrogen termination of the surface. The surface electronic structure is altered by by the presence of hydrogen from positive to negative electron affinity (NEA) [103], which increases negative ion yield as no unoccupied states are present on the surface to neutralise outgoing $H^-$ ions.

### 2.6.2 Non-Carbon Based Alternatives

Whilst most of the research plasma grid alternatives to Cs has been focused on carbon allotropes, there has been some work in non carbon based materials. In the past, tantalum has been investigated for use as a plasma grid material to enhance surface $H^-$ production, but it was found that whilst it did provide an enhancement it was not as effective as Cs. However more recently work has been conducted by Bacal and Wada [104] in the use of tantalum adsorbates on the plasma grid surface for increased surface production. Instead of using a pure tantalum plasma grid, they investigated the use of stainless steel plasma grids upon which they deposited a thin film of tungsten or tantalum. They found that when the optimum grid bias for $H^-$ extraction is used for each adsorbate material respectively, that the measured negative ion current for a grid coated in a tantalum adsorbate is comparable to that measured from a source which coats the grid in Cs. The co-extracted electron current is also similar for both Cs and tantalum covered electrodes. They suggest that tantalum should be used in place of Cs for enhancing the performance of negative ion sources.

Tantalum has been shown to be effective in absorbing atomic hydrogen and releasing it in molecular form. During the recombinative desorption of the hydrogen atoms, the resulting molecules have

been shown to have a wide range of vibrationally excited states [105] up to $\nu'' = 9$. Therefore for a plasma grid coated in tantalum adsorbates the increased vibrational energies of the molecules leads to greater negative ion densities in the vicinity of the extraction grid. The depletion of atomic hydrogen near the grid also assists in reducing negative ion losses in the extraction region of the source.

Recently Friedl *et. al.* [106] made a comparison of the $H^-$ density enhancement from Cs free alternatives and a Cs coated plasma grid, with respect to the density measured due solely to the volume production of negative ions in the bulk plasma. Cs alternative materials used were boron doped and undoped diamond, tungsten, tantalum, $LaB_6$, and MoLa (lanthanum doped molybdenum). Their results suggest that only MoLa and $LaB_6$ actually made any enhancement to the negative ion density above that measured due to volume production mechanisms.

Current fusion $H^-$ ion sources for LHD, JT60-SA, and those planned for ITER, will make use of Cs for enhanced surface production. Cs free production will become important for machines beyond ITER. As ITER is still currently under construction, ion sources for NBI beyond ITER are not a major concern. Some work towards testing alternative materials to Cs is performed at the PIIM laboratory (Physics Laboratory for Ionic and molecular Interactions) [107, 102, 58], and was planned at the SNIF [108] based at Culham. Research for Cs free $H^-$ production has also been conducted for ion sources used in the materials processing and microelectronics industries, where the simple neutralisation of $H^-$ ions is desirable for neutral beam etching techniques.

## 2.7 Neutral Beams for Plasma Etching and Materials Processing

So far the focus has been on negative ion sources and neutral beams for fusion applications. Similar $H^-$ sources have also been developed for the materials processing and microelectronics industries. Techniques developed for the next generation of ion sources to be utilised for ultra large scale integration (ULSI) circuit boards could be used for the improvement of Cs free fusion NBI ion sources.

As microchips achieve higher speeds and complexity of design, reduction of damage processes associated with plasma dry etching becomes increasingly important. Ultraviolet radiation emitted by the plasma can alter electrical properties of dielectrics. Electron hole pairs are generated in dielectric films by UV photons with an energy greater than the band gap. Trapped charges in films and material interfaces detrimentally affect the conductivity, minority carrier lifetime, and are responsible for problems such as dielectric breakdown [109]. Exposure to UV photons can also produce defects and dangling bonds on the etched surface [110]. This increases the etch rate of the material but decreases selectivity and anisotropy of the etching process.

Charge build up on the substrate surface also becomes increasingly important as the features etched onto the surface become increasingly small. Charge build up can occur through plasma non-uniformities which lead to an excess current of ions or electrons from the plasma [111]. Hashimoto [112] also found that the aspect ratio of antennas on the metal-oxide-semiconductor (MOS) device lead to an electron shading effect. Average electron trajectories from the plasma to the surface will have larger angles of incidence compared to that of the ions. For high aspect ratio antennas, ions will mostly propagate between the antennas whilst electrons will collide with the antenna walls. This results in a build up of positive charge on the base and an excess negative charge on the antennas. Incident ion trajectories are then deflected by the positive charge on the bottom of the trench. The ion deflection also contributes to a reduction in etching accuracy. Charging of the surface may also be responsible for reactive ion etching lag (RIE lag) as the energy of ions incident inside the trench is reduced.

The use of neutral beams for the etching of nanoscale devices has been proposed as a solution to these damage processes [113, 114, 115, 66, 67]. If the ions can be neutralised into a neutral beam before reaching the surface, then problems associated with charge build up and electron shading can be eliminated. Shimokawa and Kuwano [116] produced neutral beams using a fast atom beam source (FAB), in which accelerated ions were neutralised through collisions with background gas molecules or low energy electrons. The energy distribution of the neutral particles depended on the discharge voltage and the gas pressure/mean free path of the ions.

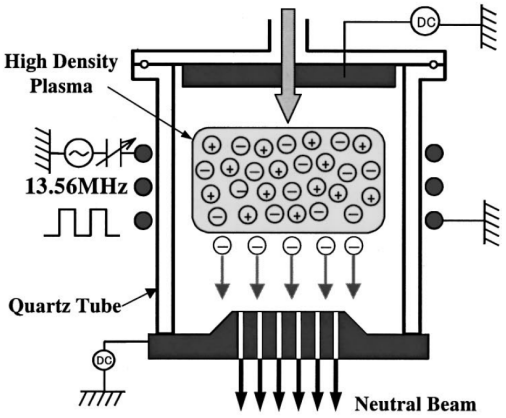


Figure 2.10: A neutral beam source for etching. Ions are accelerated towards a carbon plate, where they are neutralised through collisions as they pass through the apertures [114].

Samukawa and other groups have used biased graphite neutraliser grids to extract and neutralise the ions from a plasma discharge, in which ions are neutralised through collisions with the graphite as they pass through the apertures. Neutralisation of the ions depends on the ratio of the plasma sheath thickness S to the diameter of the orifice of the neutraliser D. If S is much larger than D the sheath is not perturbed by the grid and ion trajectories remain perpendicular to the sheath edge and parallel to the grid walls. This results in few ion collisions with the walls and only a small fraction of ions will be neutralised. When $S \approx D$ the meniscus formed by the sheath perturbation causes the ions to have a much larger angular distribution, allowing more neutralising collisions and a greater neutral particle fraction in the beam. If $D \gg S$ then a sheath forms along the neutraliser channel walls (plasma moulding) as the plasma leaks through. calculations by Nam *et. al.* for large aspect ratio holes [117] Large amounts of plasma moulding leads to more ions colliding closer to the top of the neutraliser. These ions will lose a larger fraction of energy per collision and will be reflected at larger angles increasing the probability for more collisions and more energy loss. The beam uniformity is more challenging to control with increased plasma moulding for $D \gg S$ due to a greater angular distribution of the neutral particles [118]. The neutraliser also blocks a substantial portion of UV radiation generated by the plasma, mitigating surface roughness and other UV damaging mechanisms.

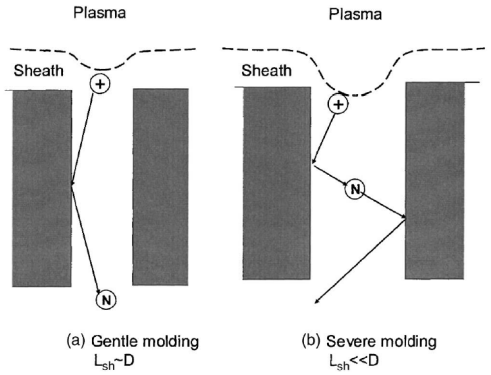


Figure 2.11: Larger orifice radius leads to increased molding of the sheath inside the grid. Increased particle collision frequency reduces neutral particle energy [118]

A very high neutralisation fraction can be achieved when extracting negative ions from the discharge as the energy required for detachment is smaller then the charge transfer energy of positive ions. Neutralisation efficiencies of almost 100% were observed for neutral beams utilising $Cl^-$ ions [119]. Samukawa *et. al.* [111] found that a neutral beam generated from a $Cl_2$ discharge produced a high selectivity etch with negligible side etching, but with a low etch rate. They suggest that Cl radicals had little to no involvement in the etching process, and that the etch was produced by the bombardment of the neutral beam. Conversely a $SF_6$ neutral beam had a high etch rate, but created a large number of F radicals leading to increased side etching. $F_2$ based neutral beams provided a improved etch rate compared to Cl with a more reasonable selectivity and reduced side etching over $SF_6$.

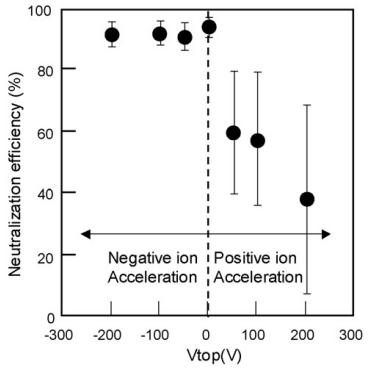


Figure 2.12: Neutralisation efficiencies of $Cl_2^+$ and $Cl_2^-$ ions in a pulsed $Cl_2$ discharge.

The neutral beam source used by Samukawa *et. al.* had an extraction/neutralisation grid diameter of 100mm, which must be scaled up and demonstrate good spatial uniformity if the technique is to be used in the mass production of ULSI devices. Kubota *et. al.* [113] developed a 200mm neutralisation aperture based on the source developed by Samukawa *et. al.*. They achieved high neutralisation efficiencies of >99%, and good spatial uniformity of less than 5% in 100mm diameter using $F_2$. $Cl_2$ neutral beams again demonstrated highly accurate etching with no undercutting. Their results suggest that the neutral beam source is scalable to larger diameter sources for industrial application whilst maintaining beam uniformity.

## 2.8 Conclusion

The rovibrational volume and surface production of $H^-$ ions have both been investigated for many years in an effort to develop efficient high current ion sources for particle accelerator, materials processing, and fusion purposes. Current NBI ion sources in development for the ITER tokamak utilise magnetic filtering to separate rovibrational excitation and $H^-$ formation for improved volume production, with the addition of Caesium a low work function plasma grid for increased surface ion generation.

The addition of Cs demonstrates increased $H^-$ yields, but will not be an option for commercial fusion reactors. Carbon has been shown to be a good candidate material for enhanced Cs free production of ions on high work function surfaces, where carbon type and operating conditions affect the negative ion yield. Experiment suggests that this is due to the electronic structure of the carbon surface, for example if the surface is hydrogen terminated and the sp3/sp2 ratio of the carbon.

Next generation ULSI semiconductor devices could use neutral beams to provide accurate anisotropic etching. Time modulated plasmas provides temporal filtering for efficient ion production, and allow tailoring of the power pulse for pumping of rovibrational populations. Whilst some testing of Cs alternatives has been performed in the more conventional magnetically filtered fusion NBI ion sources, which are more orientated toward the surface $H^-$ production mechanism, none has been performed in a temporally filtered time modulated discharge. Whilst Cs will always have a lower

workfunction, the pulsed environment may compliment the surface production from Cs alternatives by providing a larger volume density of $H^-$, reduced collisional detachment rates, and the rapid reduction of the plasma potential in the afterglow allowing easier movement of ions out of the plasma.

## 2.9 Thesis Outline

The structure of this thesis is as follows: Chapter 3 concerns the experimental set-up, the equipment, and the diagnostic techniques used throughout this project; Chapter 4 discusses results from the characterisation of a time modulated argon discharge, IVDF measurements, and the effect of an applied extraction bias on plasma properties; Chapter 5 contains results from the characterisation of a pulsed hydrogen plasma both in the centre of the discharge and extraction region, along with plasma property measurements with an applied DC bias, and IVDF measurements in the plasma bulk; Chapter 6 investigates the the effect of boron doped diamond samples on the plasma properties in the extraction region of the plasma, including Langmuir probe measurements above and below the grid, IVDF measurements, and the effect of the plasma on the samples. Chapter 7 contains conclusions and suggestions for future work.

# Chapter 3

# Experimental Set-Up

All experiments in this thesis were carried using the University of Liverpool's negative ion source. A quartz window separates a 6mm outer diameter, two turn planar copper coil around 10cm in diameter from a steel cylindrical vacuum vessel. The coil is contained within an aluminium box which acts as a Faraday shield during operation. De-ionised water is pumped through the coil to provide cooling during operation. The plasma chamber itself is 30cm in diameter and 9cm in height.

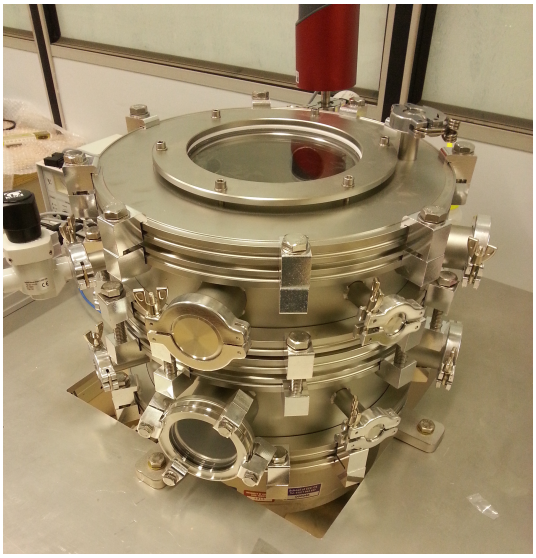

Figure 3.1: Ion source vacuum chamber

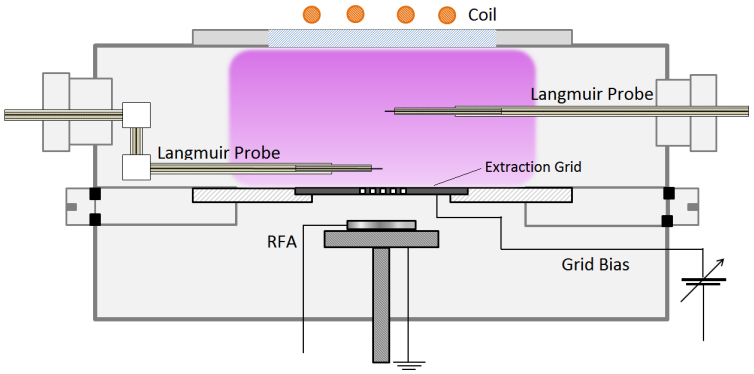


Figure 3.2: Cross section of ion source.

The vacuum chamber is divided into two sections by an extraction grid. The aluminium extraction grid is placed inside an insulating mount which allows biasing of the grid for ion extraction. The grid itself is a 20mm×20mm aluminium mesh of 0.4mm diameter apertures and when using the alternative materials is surrounded by eight 10mm by 10mm squares of material so that the Cs alternative samples are symmetric around the extraction apertures.

RF power is delivered to the coil using an MKS Elite 1.2kW power supply. It can provide up to 1200W of 13.56MHz RF power, that can be used in continuous wave or pulsed modes. The pulsing of the RF can either be carried out internally by the power supply or through an external bias applied to pin 24 of the interface connector. The RF output is screened when a bias is applied so by using an external bias with a particular frequency and pulse length, the RF pulse frequency and duty factor can be easily selected. The blanking signal used to pulse the RF is generated by a Stanford digital pulse generator which has a pulse rise time of around 2ns. The same signal is then also used to trigger the oscilloscope for acquisition of Langmuir probe characteristics. A matching circuit is situated above the coil/Faraday shield which enables the forward power into the matching-coil-plasma network to be maximised.

Vacuum pumping of the chamber is provided by a ACP 28CV backing pump in combination with a HiPace 300C turbomolecular pump. The pressure in the discharge is monitored using a Pfeiffer Pirani gauge, a full range gauge which makes use of a Pirani at higher pressures and switches to a cold cathode pressure gauge at pressures below $10^{-2}$mbar, and a Peiffer baratron gauge with a 0.1mbar range. An identical second baratron monitors the pressure in the lower chamber.

The work conducted in this project was performed in argon, hydrogen. Hydrogen gas was provided by a Peak Scientific Hydrogen Trace machine, which generates hydrogen on demand using deionised water through electrolysis. The machine outputs the gas at 250sccm, at a pressure up to a maximum of 7.5bar. The gases then passes through an MKS Mass Flow Controller (MFC) before entering the vacuum chamber. In argon and hydrogen the system operates with a gas pressure of a few Pascals. A problem arose due to the discontinuity in the flow rates between the hydrogen generator and the MFC as once the pressure achieved its desired value in the pipeline before the MFC, the generator would stop producing hydrogen. The vacuum would then drain the gas, but a delay before the hydrogen trace began to produce hydrogen again would cause fluctuations in the final pressure value achieved in the vacuum chamber. This was solved by placing a needle valve between the output of the hydrogen machine and the MFC, effectively giving the MFC controller its own small hydrogen reservoir that is mostly immune to the pressure fluctuations. This reduced the pressure fluctuations from greater than 0.4Pa to around 0.04-0.06Pa which dramatically improved the IV characteristic data taken by the Langmuir probes. The Langmuir probes use for this system were constructed with tungsten wires with diameters ranging from 0.2-0.25mm, and a combination of ceramic and stainless steel tubing.

## 3.1 Langmuir Probes

The system makes use of two Langmuir probes: one positioned in the centre of the plasma chamber for measuring bulk plasma characteristics, and a second probe with its tip approximately 1cm away from the extraction grid of the chamber in order to measure differences in plasma properties close to the grid when making use of Cs free alternatives on the plasma grid and when a bias has been applied to it. The probe positioned in the centre of the chamber is mostly built from 3mm outer diameter alumina tubing, and 6mm stainless steel outer tubing. This sits inside quarter inch outer diameter stainless steel tubing for mounting through the flange.

Time resolved Langmuir probe characteristics were measured by capturing the probe signal throughout a pulse of the plasma activeglow and afterglow. A probe signal was acquired for each individual probe bias, after which the data was smoothed using by applying a Fourier transform filter to re-

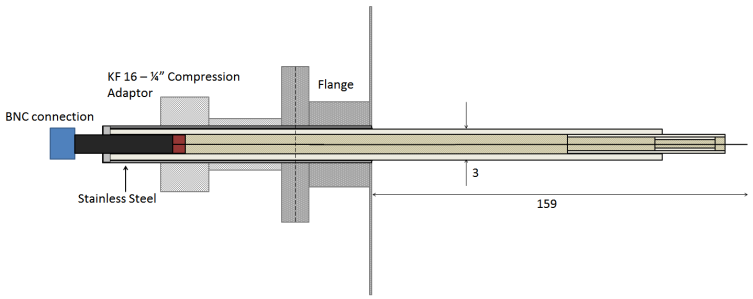


Figure 3.3: Schematic of the Langmuir probe utilised in the centre of the discharge chamber.

move higher frequency signals. The data is then concatenated and IV characteristics for each time step can then be built from all the probe signals measured at that particular time in the pulse. The probe signals measured on the oscilloscope are usually made up of around 50-100k data points per pulse, and averaged by the scope 512 times. Before analysing the information the data points themselves were usually averaged in sets of twenty, which at a typical pulse frequency of around 2kHz corresponds to a timescale of 4ns for 50k data points. This is much shorter than the timescales of the processes relevant to this investigation, so no important information should be lost through the averaging process.

### 3.1.1 Langmuir Probe Theory

Langmuir probes have been a widely used plasma diagnostic tool for decades due to their relatively simple construction, ease of implementation, and their ability to extract a wide range of information from the characteristics. However although the use of probes and acquisition of data is simple, the analysis of the data to extract accurate and reliable information about the plasma parameters can be difficult. An Ideal IV curve is shown in figure 3.4. Langmuir probe IV characteristics have several key features: the ion saturation region, the transition region, the electron saturation region, floating potential, and plasma potential. When an unbiased probe is placed in the plasma bulk, a sheath potential emerges in an identical manner to the walls surrounding the discharge, and the net current through the probe tip is zero. The point on the IV characteristic where the current passes through zero is the floating potential.

Beyond the floating potential is the transition region, where the probe begins to collect electrons.

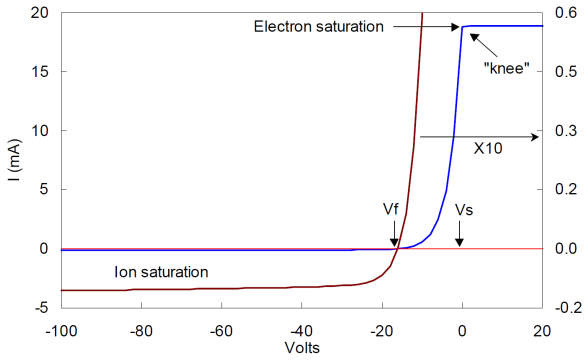


Figure 3.4: An ideal Langmuir IV characteristic [120]

.

Due to the much greater mobility of the electrons, the electron current is much larger than that of the ions. If it is assumed that the plasma contains a Maxwellian distribution of electrons, the current drawn by the probe in the transition region is given by

$$I_e = I_{sat_e} exp\left(\frac{e(V_p - V_s)}{kT_e}\right) \tag{3.1}$$

Where $I_{sat_e}$ is the electron saturation current, given by

$$I_{sat_e} = en_e A\sqrt{\frac{kT_e}{2\pi m}}, \tag{3.2}$$

$n_e$ is the electron density, and A is the probe surface area. When the probe current is plotted semi-logarithmically against probe bias, the gradient of the linear region provides a measurement of $1/T_e$.

Once the probe bias reaches the plasma potential, the probe collects the entire thermal flux of electrons around the probe tip. The plasma potential can be obtained through several methods: the intersection between a linear fit of the electron saturation and the end of the transition region; A large peak in $1^{st}$ derivative of the IV characteristic; and when the $2^{nd}$ derivative of the curve passes through zero. In an ideal characteristic, beyond this point the electron current would remain constant as all of the electrons surrounding in the sheath around the probe are collected. However the more realistic situation is that the probe current continues to increase slowly in the electron

saturation region, as the high bias depletes the surrounding space of electrons. This leads to the sheath around the probe expanding and the effective collection area of the probe increases so the current never truly saturates.

One can use equation 3.2 with the current measured at the plasma potential in order to obtain an electron density. However this is generally unwise as the knee of the curve occurs in the transition region, and the exponential behaviour of this region means small inaccuracies in the voltage leads to a large error in the current and therefore large errors in the calculated value of $n_e$.

The extraction of electron or ion densities from the IV characteristic usually requires a theory of ion collection. The simplest of these theories, and also the most restrictive, is orbital motion limited theory.

**Orbital Motion Limited Theory**

OML theory considers the current drawn by a probe when all of the undisturbed particles (which energetically have the capability of reaching the probe) are able to be collected by the probe. if the point of closest approach in the ion's trajectory is smaller than the radius of the probe, then the ion is collected. OML uses the limit that the sheath is infinitely large in size compared to the probe dimensions, i.e.

$$a/\lambda_D \longrightarrow 0, \tag{3.3}$$

where $a$ is the probe radius and $\lambda_D$ is the Debye length.

Using the conservation of energy and the ion's angular momentum

$$\frac{1}{2}m(v_r^2 + v_\phi^2) + e\left[\Phi_p - V_b\right] = \frac{1}{2}m(v_r'^2 + v_\phi'^2) \tag{3.4}$$

$$sv_\phi = av_\phi' \tag{3.5}$$

where $a$ is the probe radius, $s$ is the sheath radius, and $m$ is the mass of the ion species drawn into the probe tip. Using equations 3.4 and 3.5 yields

$$v_r'^2 = v_r^2 + v_\phi^2 + \frac{2e\left[\Phi_p - V_b\right]}{m} - \frac{s^2}{a^2}v_\phi^2 \tag{3.6}$$

Setting $v_r'^2$ to zero, we obtain

$$v_\phi = \left(\frac{v_r^2 + 2e\left[\Phi_p - V_b\right]/m}{s^2/a^2 - 1}\right)^{\frac{1}{2}} \tag{3.7}$$

The saturation current collected by the probe is calculated by an integral of the radial flux of ions over the energy distribution of the ions at the sheath edge. In this case it is assumed that the distribution is an isotropic Maxwellian

$$f = \frac{m}{2\pi eT} exp\left(\frac{m(v_r^2 + v_\phi^2)}{2eT}\right) \tag{3.8}$$

where T is the temperature of the ion species at the sheath edge. The integral is not simple and is solvable using error functions. However by making some assumptions for a probe biased to a large voltage, the integral can be simplified. If the probe has a large bias applied, then the sheath size will be much larger than the probe radius,

$$\frac{a}{s} \ll 1 \tag{3.9}$$

and also making the assumptions

$$v^2 \ll \frac{e\left[\Phi_p - V_b\right]}{m} \tag{3.10}$$

and

$$v_\phi^2 \ll \frac{eT}{m} \tag{3.11}$$

equation 3.7 then becomes

$$v_{\phi 0} = \frac{a}{s}\left(\frac{2e\left[\Phi_p - V_b\right]}{m}\right)^{\frac{1}{2}} \tag{3.12}$$

Using equation 3.12 and 3.8 and integrating

$$I = -2\pi s d n_s e \int_{-\infty}^{0} v_r dr \int_{-v_{\phi 0}}^{v_{\phi 0}} f(v_r, v_\phi) dv_\phi \tag{3.13}$$

Yields the ion (or electron) saturation current, given by

$$I = 2ad n_s e\left(\frac{2e\left[\Phi_p - V_b\right]}{m}\right)^{\frac{1}{2}} \tag{3.14}$$

The saturation current given in equation 3.14 by a collisionless sheath with a Maxwellian particle energy distribution is independent of the species temperature, and a plot of $I^2$ against $V_b$ would be linear and proportional to square of the density of the plasma, $n_s^2$ [77].

$$n_s^2 = \frac{m}{8e^3(ad)^2}\frac{dI^2}{dV_b} \tag{3.15}$$

OML is limited in its application due to the fact that one must assume that the width of the sheath surrounding the probe is essentially infinite, and it also assumes that there is no absorption radius around the probe, i.e. a region in the sheath where the electric field is strong enough such that ions cannot escape. The vast majority of plasmas have a well defined, not infinitely large sheath, and have an absorption radius meaning that OML is not applicable. OML also considers the sheath to be collisionless i.e. the mean free path for collisions with other ions and background neutrals is much larger than the sheath thickness. This is often not true, and the presence of collisions in the plasma lead to more complicated treatment of the probe characteristics. Collisions result in smaller sheath sizes [121] which will affect the validity that OML theory may have had. In a more realistic scenario the charged species propagate around the probe tip with orbital motion, leading to some particles to have a trajectory which orbits around the probe tip and do not contribute to the

collected current. However when collisions are include this orbital motion is disturbed causing some particle which would would otherwise have not been collected to have a new trajectory towards the probe tip leading to a larger collected current [122]. As OML makes an assumption of no collisions the larger probe current caused by collisions leads to overestimations of the density.

Generally OML is an applicable theory when the ratio of probe radius to the Debye length is less than three [123, 124]. Also a plasma with collisions in the sheath region ($\lambda_{e,i} \approx$ sheath size), the electrons/ions collected are drawn in from close proximity to the probe and the measured parameters such as $T_e$ only represent the *local* discharge conditions. Other parts of the probe theory also begin to become less valid, for example [125] discusses the breakdown of the Bohm criterion in sheath formation when considering a collisional sheath or pre-sheath.

It is also unphysical for the plasma to have a discrete boundary between the plasma bulk and the electron depleted sheath region. In reality a pre-sheath region exists in which ions are accelerated to the Bohm velocity before entering the sheath. However inclusion of the pre-sheath in the treatment of ion collection makes the physics much more complicated.

According to Chen [126], OML is still useful as it it can still provide good values of ion densities even when it should technically should be invalid. OML generally yields much simpler and easier to interpret results compared to other ion collection theories such as ABR and BRL. OML also provides an upper limit to the current collected by a probe in the limit of a collisionless sheath/discharge as potential barriers which arise when considering collection radii and non-infinite sheaths are only able to reduce the current collected by a probe. However this results in OML often over-estimating the density of ions in the discharge [124].

#### Electron Energy Distribution Function

The electron energy distribution function (EEDF) of the plasma can also be extracted from Langmuir probe characteristics. EEDFs allow the calculation of the electron temperature and plasma density and can also provide valuable insight into the nature of the energy distribution of the electrons, i.e. if the plasma contains a Maxwellian, bi-Maxwellian, or Druyvesteyn distribution. For an ideal characteristic, at the plasma potential the electron current saturates and all electrons are

collected by the probe. As the bias becomes more negative with respect to the plasma potential lower energy electrons are screened by the potential barrier until all electrons are prevented from reaching the probe as the current approaches zero. This screening of the electron population allows insight into the energy distribution of the electrons in the plasma. The EEDF of an isotropic distribution of electron energies is given by

$$g_e(V) = \frac{2m}{Ae^2}\left(\frac{2eV}{m}\right)^{1/2}\frac{d^2I_e}{dV^2} \tag{3.16}$$

This method is useful as it is valid for any convex probe shape, eg. a cylindrical probe geometry, as well as being applicable to any isotropic velocity distribution of electrons. It also makes no assumptions regarding the ratio of the probe radius to Debye length. As previously stated this technique also allows the calculation of electron temperatures and densities from non-Maxwellian distributions [77].

The electron probability distribution can also be calculated from

$$g_p(\epsilon) = \epsilon^{\frac{1}{2}} g_e(\epsilon), \tag{3.17}$$

and electron density can be calculated from the integral of the distribution function over all energies

$$n_e = \int_0^\infty g_e(\epsilon)d\epsilon \tag{3.18}$$

This measurement can be difficult to implement however as it relies on the second derivative of the IV characteristic which means that it is sensitive to noise and usually requires the use of smoothing in order to provide useful information, and in some situations can only provide qualitative insight into the nature of the electron population in the discharge.

## 3.2 Retarding Field Energy Analyser

A retarding field energy analyser (RFA) was used to measure the velocity and energy distributions of ions in the discharge. The RFA operates with a series of grids designed to remove the electrons from the incident particle flux and collect the remaining ion current. A repelling grid is biased to a sufficiently negative potential such that all electrons are diverted away to the walls. Ions are accelerated through the negative potential into the next stage of the RFA. A second grid is then bias relative to this repulsion voltage. When the two biases are equal, all of the ions move through and are collected by an electrode. As the bias of the second grid is made to be increasingly positive, only ions with enough energy to overcome the potential barrier are able to contribute to the measured current. This bias is swept over a range until ideally no current is collected as no ions are capable of reaching the electrode. The gradient of the current signal then yields the energy distribution of the collected ions.

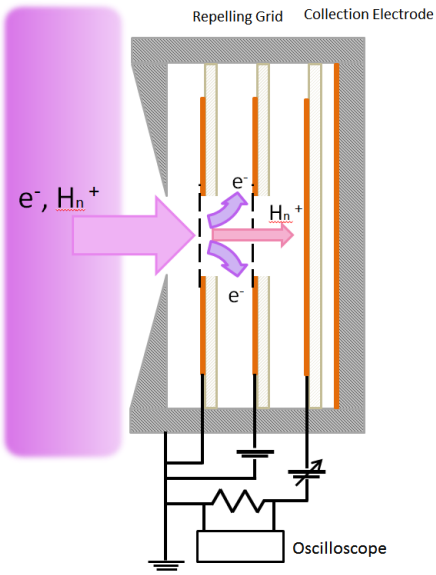


Figure 3.5: Schematic of the RFA used to measure IVDFs in the ion source.

As ions bombard the grids and collection electrode they can liberate secondary electrons from the surface which will affected the measured current through the loss of negative charge from the material. This effect becomes particularly important when only a fraction of the ions are being

collected, i.e. at large positive bias relative to the electron repulsion electrode. This is because the typical secondary emission coefficient is on the order of a few percent, so when only a few percent of the ion flux is collected it can have a significant effect.This can be combated through the use of an extra electrode to repel any secondary electrons generated back to the collection electrode. Another issue that can arise in high density plasmas is if the plasma is able to enter the analyser and charge species are selectively removed from the flow, then this will create a charge density difference between the grids which can alter the potential between them.

# Chapter 4

# Argon Characterisation

## 4.1 Introduction

Pulsed plasma sources have been identified as a solution to a variety of problems associated with plasma etching of semiconductor devices, as discussed in section 2.5. The University of Liverpool is currently developing an pulsed ion source based on a planar coil inductively coupled plasma discharge. In this chapter the characterisation of a pulsed argon ICP discharge, at a variety of gas pressures, pulse frequencies, pulse duty factors, and RF powers, is presented.

The primary aim of this work was to demonstrate that the ion source could reliably sustain an argon plasma in the inductive H mode over a wide range of operational conditions. A second aim was to understand the effect of a bias applied to the extraction grid and extracting ions on the bulk plasma properties, as ion sources used in fusion NBI systems ions are continually extracted into the acceleration systems. In contrast to conventional NBI ion sources which utilise magnetic filtering to reduce the electron temperature in the extraction region, this ion source uses temporal filtering to achieve this as electrons cool rapidly during the early stages of the afterglow period of the pulse.

Argon is an ideal gas for this initial characterisation as it is a monatomic gas, with few channels for inelastic electron collision processes other than ionisation. As a result it is easier to ignite a plasma, and does not require a very large amount of RF power to induce a transition from the initial E mode

to H mode. Characterisation of the ion source was conducted using Langmuir probe diagnostics and a retarding field energy analyser (RFA). This chapter is divided up into the following sections: Section two discusses the Langmuir probe measurements, and the evolution of the plasma properties extracted from IV characteristics throughout the RF pulse cycle. Section three concerns the effect of a DC bias applied to the extraction grid throughout the pulse on the measured plasma properties. Finally section four summarises the measurements conducted with the RFA, and the evolution of the ion velocity distribution functions during the activeglow and afterglow of the discharge.

## 4.2 Evolution of Plasma Properties In a Time Modulated Discharge

### 4.2.1 Procedure for Measurement of Langmuir Probe IV Characteristics

IV characteristics were measured using a Langmuir probe positioned in the centre of the discharge chamber. This measurement was performed for a variety of different discharge conditions: varying the pressure, power, RF pulse frequency, and pulse duty factor. Usually a voltage sweep from -20V to 25V was used to obtain characteristics but this maximum value varied depending on the discharge conditions, as larger currents drawn from higher density plasma would cause the tip to glow hot due to electron bombardment. Before the data was processed and concatenated the pulse was separated into its respective activeglow and afterglow components. During this separation process the data was also put through a high frequency Fourier filter in order to try an eliminate noise introduced through the RF fluctuations in the plasma. As discussed previously, one often has to use filters with Langmuir probes in RF as the oscillation of the potential difference between the probe and the plasma potential can introduce errors when determining plasma parameters from IV characteristics. At first some effort was made to create a passive RF filter between the probe and the oscilloscope, which did provide some reduction to the measured RF amplitude on the probe signal. However as a lot of the RF oscillation is lost to ground through the stray capacitance between the probe stem and the chamber wall, and even if some of the noise is filtered before the oscilloscope, the fluctuations are still affecting the current collected by the probe inside the discharge. Active

filtering may have been possible to set up but would have taken a lot of time and effort, and may have not worked effectively. EM fields should be effectively shielded within the plasma's skin depth. Provided that the observed RF oscillations are not on the order of the electron temperature, then the IV characteristics measured should be mostly unaffected by the presence of RF, and therefore it was decided that RF filtering was not a requirement.

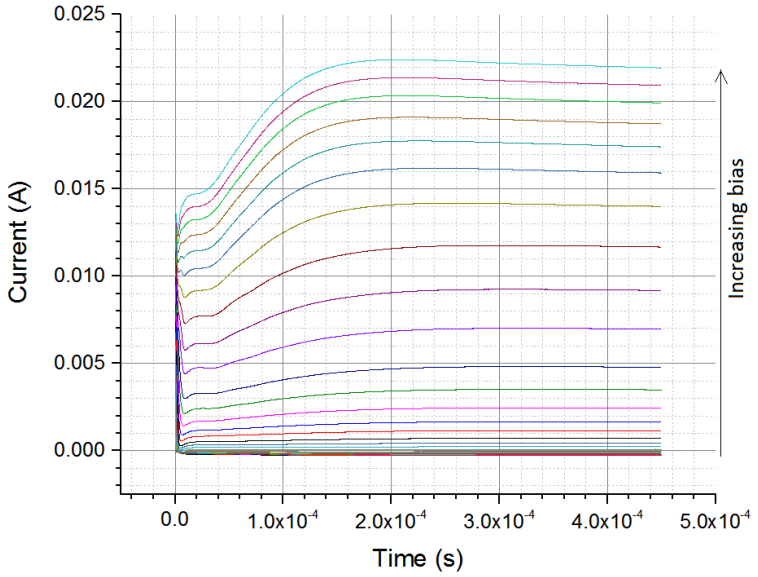


Figure 4.1: Typical current waveform measured by Langmuir probe positioned in the centre of a 2kHz 90% duty factor argon discharge during the activeglow. Each line represents the current drawn at a different probe bias.

Figures 4.1 and 4.2 shows the typical current pulse shape in the activeglow and afterglow of the discharge as the probe bias is increased. Langmuir characteristics can be constructed by taking a vertical slice through the set of current pulses. By performing this process throughout the activeglow and afterglows the evolution of the plasma properties can be extracted from IV characteristics measured at different times during the RF pulse. Figure 4.3 shows that the plasma takes on the order of 100-200$\mu$s to reach a quasi-equilibrium state where the current remains largely the same for the remainder of the pulse. An increase in the measured probe current can be observed during the early stages of the afterglow, which can be associated with two process: the initial rapid decrease of the plasma potential allowing a greater flux of electrons to be pulled into the probe by the applied bias; and high energy electrons released through the relaxation processes of argon metastables. Metastable states present in the discharge typically have long lifetimes compared to

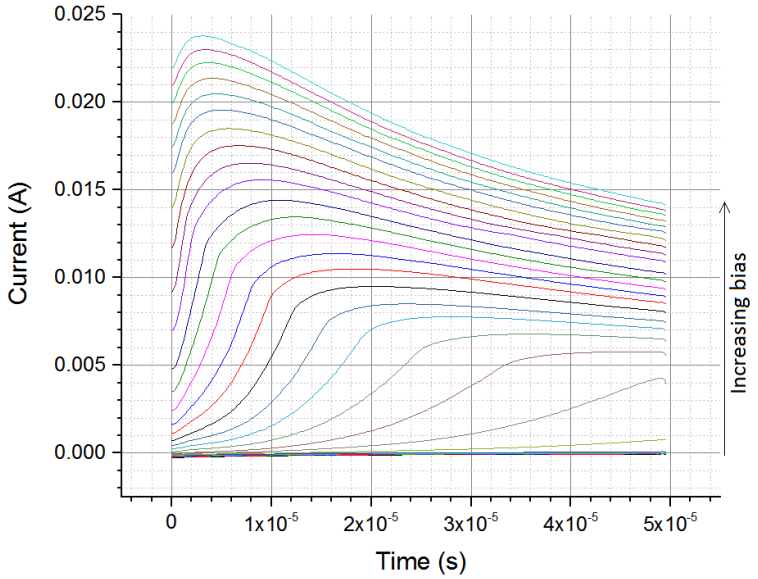


Figure 4.2: Typical current waveforms measured at different probe biases in the centre of a 2kHz 90% duty factor argon discharge during the afterglow.

other atomic excitation and relaxation processes, and so a population of metastables generated during the activeglow could survive into the afterglow.

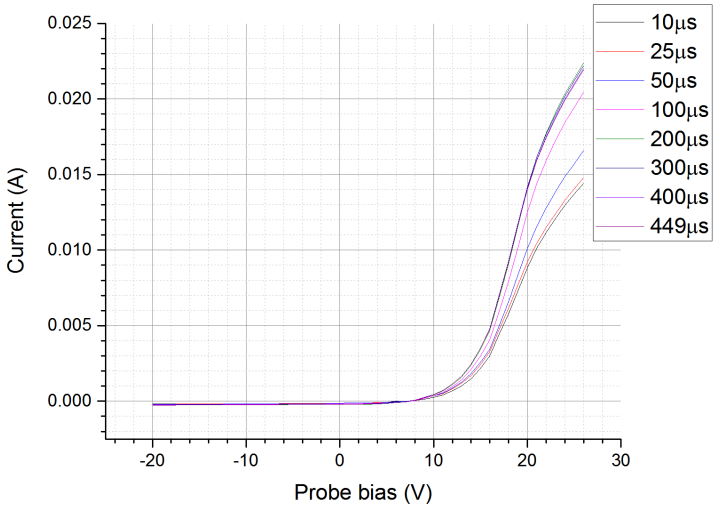


Figure 4.3: Evolution of IV characteristics during the activeglow of a 2kHz 90% duty factor argon ICP discharge. Electron saturation current increases, but there is little change to the features of the IV curves after the first few $\mu$s.

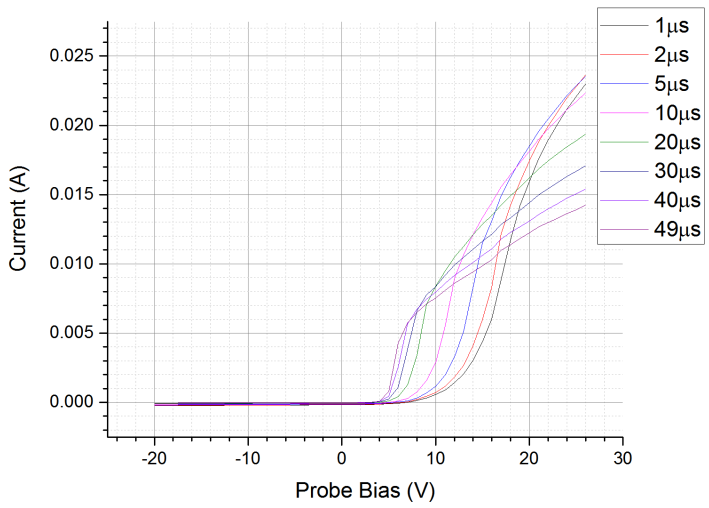


Figure 4.4: IVs measured during the afterglow of a 2kHz 90% duty factor argon discharge. Plasma potential and electron saturation currents rapidly decrease, whilst the gradient of the transition region becomes steeper indicating a decreasing electron temperature.

Extraction of the plasma properties for each IV characteristic was carried out using the techniques outlined in section 3.1.1. OML was used for calculation of the plasma density for both argon and hydrogen discharges. Plasma potential was taken to be the peak of the first derivative of the IV characteristics and the electron temperature was measured between the floating potential and plasma potential, assuming a maxwellian distribution. The typical values measured in the argon discharge for electron temperature and density result in a Debye length of approximately $4\times10^{-5}$m, resulting in a probe tip radius ratio of 5, which is on the borderline of where OML can be considered to produce accurate values of density [123, 124]. The treatment of the ion region was quite simple, i.e. a linear fit was taken of the whole data set below the floating potential, this often includes some of the data which begins to curve up into the transition region of the IV curve. This means values of densities extracted will be a slight over estimation/an upper limit of the plasma density, however OML itself gives an over estimation of densities in most cases due to assumptions such as collisionless sheaths [124].

This process was repeated for a variety of discharge conditions, varying the input power, the pulse frequency, pulse duty factor, and pressure of the discharge.

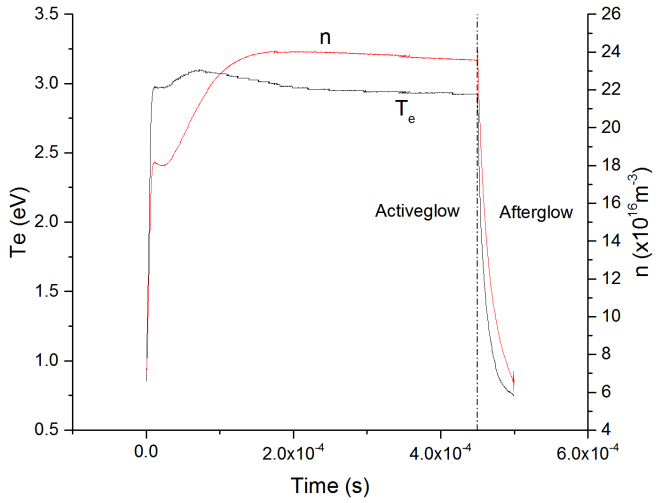


Figure 4.5: Evolution of $T_e$ and $n$ throughout the modulation cycle of a 2kHz 90% duty factor argon plasma operated at 2.2Pa with 100W of RF power.

Figure 4.5 demonstrates the time evolution of electron temperature and plasma density characteristics throughout the activeglow and afterglow in an argon discharge operating at 2.2Pa, input power of 100W, with an RF power pulse frequency of 2kHz at 90% duty factor. The activeglow IV curves show a rapid increase in the electron saturation current as the plasma recovers from the low plasma density at the end of the previous pulse. After around 100$\mu$s the change in the IV characteristics is small as the plasma has achieved its quasi-equilibrium state. In this equilibrium the changes in the plasma potential, electron temperature, and plasma density are small as the plasma has attained a quasi steady state with parameters similar to those that would be observed if the RF power was run in continuous wave. For the afterglow, the plasma potential rapidly decreases, and the gradient of the transition region increases as the high energy electrons are quickly lost to the walls and the average electron temperature decreases. As discussed in section 2.5.2, equation 2.39 shows that as the electron temperature and mobility decrease, the plasma potential also decreases [6]. The electron saturation current also decreases quickly in the afterglow as the electrons are lost to the chamber walls and the electron temperature drops below the threshold for ionisation.

An estimation of errors in the measurements of plasma properties was carried out by repeating IV characteristic measurements for the same discharge conditions on separate days. Measurements

were repeated over a five day period, and the observed plasma properties were compared. The difference in electron temperature and plasma density was found to be on the order of 10-15%, with larger variance in the density measured from each day.

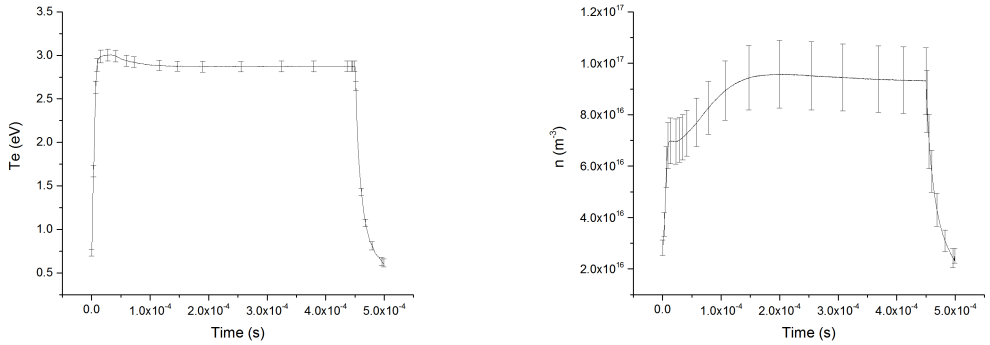


(a) (b)

Figure 4.6: Estimation of uncertainty for probe measurements of (a) $T_e$ and (b) $n$.

During these initial measurements with argon the installed baratron was not functioning properly, and so a less accurate compact full range gauge had to be relied upon instead. This pressure gauge makes use of a pirani gauge at higher pressures and a cold cathode pressure gauge at pressure below $10^{-2}$mbar. At a few Pascals, the gauge reading is a combination of the pirani and cold cathode, with an accuracy to within ±30%. Generally the pressure of the discharge was controlled by maintaining the same flow rate through the mass flow controller, so whilst the error on the value of the pressure is reasonably large the pressure between different experimental runs should remain consistent.

### 4.2.2 Plasma Property Dependence on Input RF Power & Gas Pressure

Increasing the power delivered to the plasma results in an increase in the measured plasma density, with little effect on the measured electron temperature or plasma potential. In most simple plasma models $T_e$ is decoupled from the power density in the plasma. The density of charges however is very strongly connected with the power deposited into the plasma. Figures 4.8 show $T_e$, the plasma density, and plasma potential measured in a 2kHz 90% duty factor argon discharge with a gas pressure of around 2.3Pa. The electron temperature and the plasma potential remain essentially constant from 100W to 200W of RF power. Figure 4.8 demonstrates that the charge carrier density

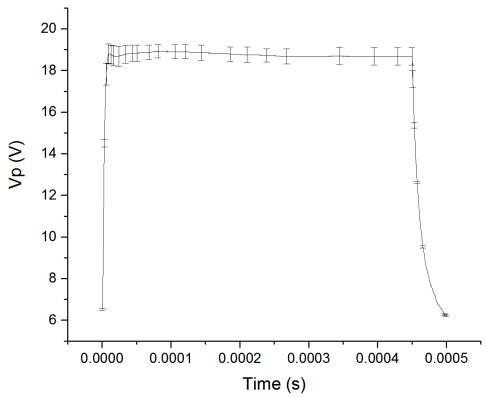


Figure 4.7: Estimation of uncertainty for probe measurements of $V_p$

of the plasma increases with with power from around $7\times10^{16}$ at 100W to $2.4\times10^{17}$ at 200W once the plasma has reached its quasi-equilibrium density value after 200$\mu$s.

Increasing the feeding gas pressure of the discharge will reduce the mean free path of the electrons, leading to a decrease of the average electron temperature as the greater collisionality of the plasma will result in the high energy population of electrons in the discharge distributing their energy more frequently through collisional processes. More inelastic collisions between electrons and neutrals will result in more ionisation and the charge carrier density of the plasma should increase, as shown in figure 4.9. Figure 4.9 shows that as gas pressure the is increased the measured plasma potential decreases, this is due to the reduced electron temperature and the smaller Bohm velocity required to equate the electron and ion currents incident to the chamber walls.

If the cooling of the electron temperature is controlled mostly through the diffusion of electrons to walls, the decay of the electron temperature during the afterglow should be affected by the pressure of the discharge. Figure 4.10 shows the decrease of $T_e$ during the afterglow at different pressures (a) and at different powers (b). The electron temperature can be seen to decrease more rapidly at lower feeding gas pressures. This suggests that the mechanism for the decay of $T_e$ in the afterglow is diffusion cooling [127, 128]. As the average temperature and thermal velocity of the electrons is greater at lower gas pressures, they will be lost to the chamber walls more rapidly in the afterglow as the plasma potential rapidly diminishes.

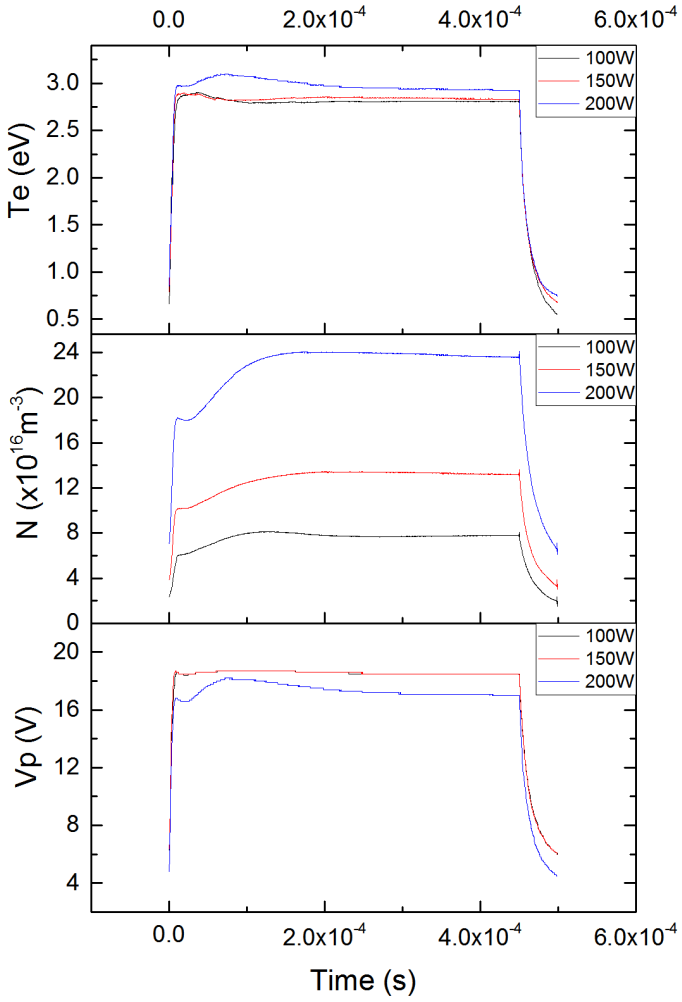


Figure 4.8: Effect of changing RF power in plasma properties for a 2kHz 90% duty factor discharge operated at 2.3Pa.

Figure 4.11 shows a comparison between the measured decay of the electron temperature during the afterglow of the pulse and the analytical expression for the temperature decay, Given by [78]

$$T_e(t) \approx T_{e\infty} \left(1 + 2\nu_\infty (t - \alpha\tau)\right)^{-2}. \tag{4.1}$$

There appears to be a good agreement between the experimental data and the calculated decay of the electron temperature for electropositive gases. This expression assumes that the dominant loss

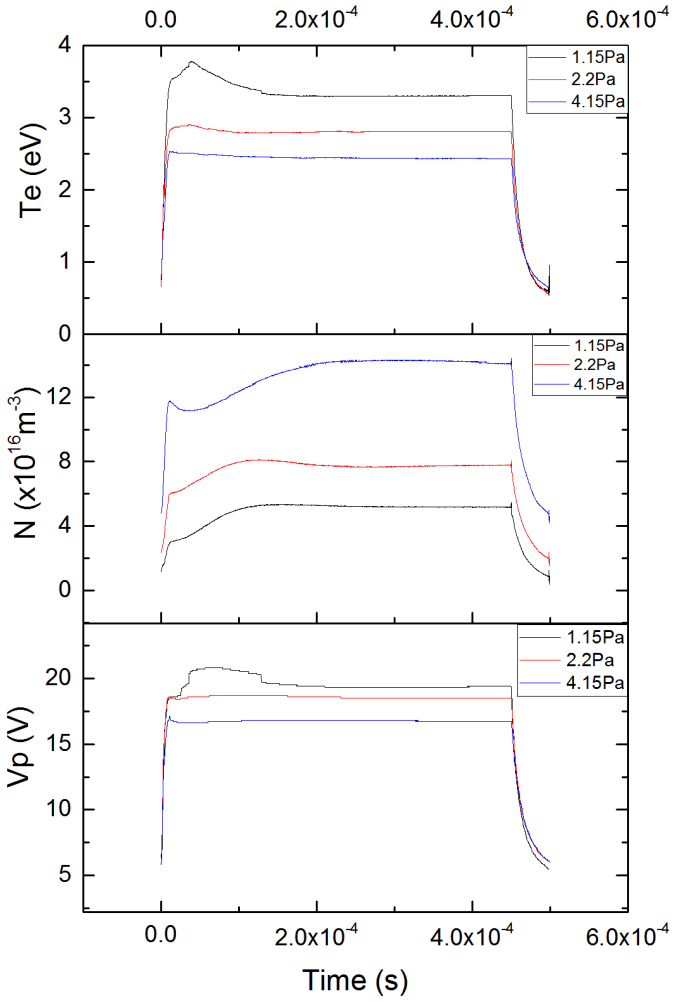


Figure 4.9: Plasma property measurements with increasing gas pressure in a 2kHz 90% duty factor at 100W.

of electrons and electron energy in the afterglow is through diffusion to the walls. The agreement between this expression and experiment implies that electron cooling mechanism in the afterglow is through diffusion.

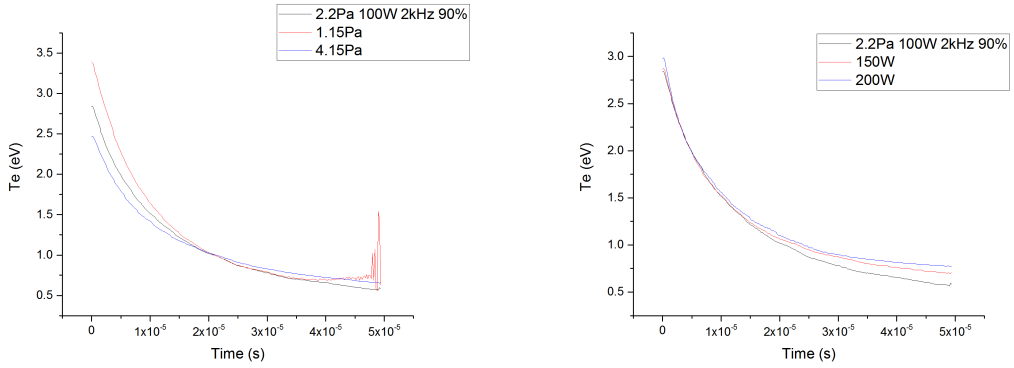


(a) (b)

Figure 4.10: Decay of the electron temperature in the afterglow at (a) different pressures and (b) increasing power. This afterglow was for a 2kHz 90% duty factor discharge.

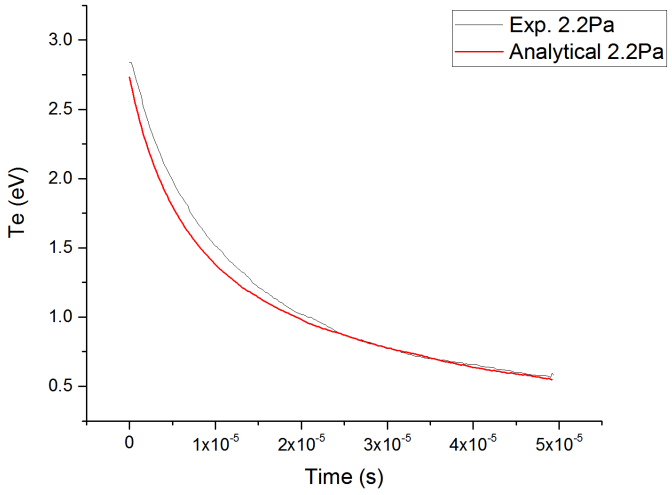


Figure 4.11: Comparison between experimental $T_e$ measurements taken in the afterglow of this experiment and an analytical expression for the the decay of $T_e$ in an electropositive gas discharge.

### 4.2.3 Dependence of Plasma Properties on Pulse Modulation

Figure 4.12 shows the effect of changing modulation frequencies on plasma properties in the centre of the discharge. Altering the modulation frequency and the duty factor of the pulse should result in a similar effect on the plasma properties. Changing the modulation frequency should have little effect on the plasma properties for lower frequencies, as the plasma has plenty of time to reach its

quasi-steadystate values. Higher frequency power modulation has little effect on on the electron temperature and plasma potential but results in reduced maximum plasma density achieved during the pulse as the production rate of ions in the early stages of power deposition is much slower than that of the electron temperature. If the rate of production of meta-stable atoms is slow enough such that at higher modulation frequencies they are unable to achieve a large enough population to have a significant affect on the ionisation rate in the plasma, this could result in reduced plasma densities compared to those observed at lower modulation frequencies for the same pressures and powers. Also if one considers the way the power is deposited into the system (where the RF power supply is supplying a continuous amount of power which is then gated by the screening voltage provided by the pulse generator), the amount of power supplied per cycle into the plasma may also provide an explanation for the reduced density at higher frequencies. If the power supply outputs a continuous 100W, then for a 1kHz pulse at 90% 0.09J of energy is deposited during the activeglow phase (assuming 100% power transfer), whilst for 2kHz this amount drops to 0.045J.

With a fixed duty factor, lower frequency modulation will lead to increased afterglow periods in the pulse as shown in figure 4.12. This will produce much lower values of plasma density and electron temperature at the end of each pulse cycle. Lower plasma density at the end of the pulse will result in a more pronounced peak in electron temperature during the initial stages of the activeglow.

Figure 4.13 shows how the steady state value of the electron temperature measured in the centre of the chamber is largely unaffected by a change in the pulse duty factor. A duty factor 60% demonstrates a more obvious overshoot as power is initially deposited into the lower density discharge. The measurements of $T_e$ have larger errors for later times in the afterglow as the measurement is made between the floating potential and plasma potential, which have a decreasing number of data points available as the plasma potential rapidly decays. As this data set diminishes the fluctuations between the points due to the intrinsic uncertainty in the current measurement also have a larger effect.

Figure 4.13 shows that the steady state values of density are close to or within one standard deviation of each other. The lower duty factor pulses take much longer to achieve this maximum density value however, and this may be attributed to the E-H transition in the plasma. During each pulse the discharge must start from its initial low density state and transition into the high density

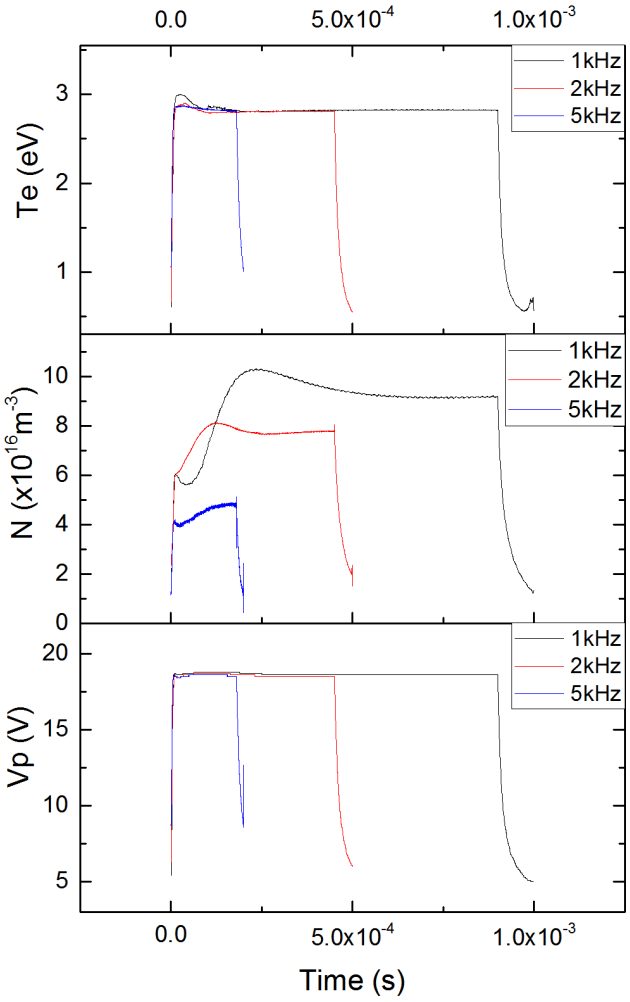


Figure 4.12: Effect of changing modulation frequency on plasma properties. The duty factor is kept constant at 90%, with a gas pressure of 2.2Pa and power of 100W.

inductive mode. As the lower duty factor pulses will start each cycle with a lower electron density, it requires more time before the plasma can reach the conditions necessary to start the cascade into H mode. A similar behaviour can be seen at 1kHz, where the extended afterglow period results in a reduced plasma density at the beginning of each new pulse cycle. Changing the duty factor will also affect the population of meta-stable atoms at the beginning of the next cycle. [129] suggests that step-wise ionisation of argon atoms through metastable state plays an important role in the in the ionisation rate of the plasma and the transition from E-H mode in the early stages of the

pulse as power is initially deposited into the discharge. Whilst the electron temperature and density rapidly decrease in the afterglow over a few tens of $\mu$s, the argon metastable density lifetime is on the order of milliseconds. Chemi-ionisation and metastable collisions with electrons can result in a population of high energy electrons during the afterglow. The density of these metastables will decrease with larger afterglow periods and so there are fewer during the initial heating of the next pulse, leading to a reduced higher energy electron population and less step-wise excitation of argon atoms.

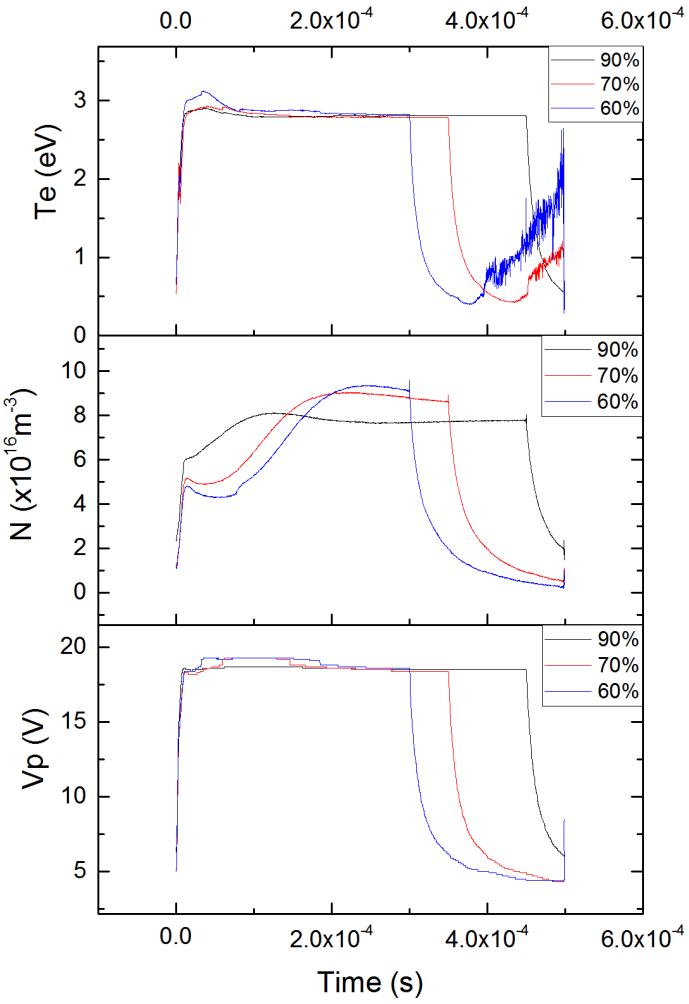


Figure 4.13: Evolution of plasma parameters in a time modulated discharge with a fixed modulation frequency of 2kHz and changing pulse duty factor. Gas pressure of 2.2Pa and power of 100W.

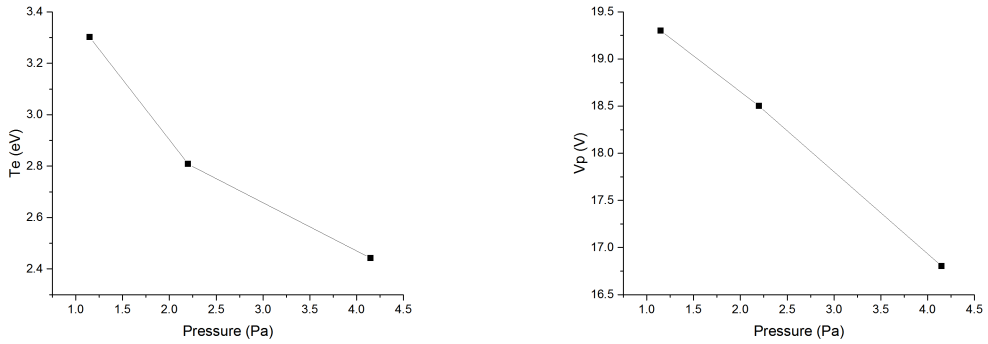


(a) (b)

Figure 4.14: $T_e$ (a) and $V_p$ (b) with increasing gas pressure, measured during the quasi-equilibrium phase of the plasma at 200$\mu$s.

Figure 4.14, 4.15 show more detailed behaviour of $T_e$ and $V_p$ with increasing pressure and power at 200$\mu$s into the activeglow, during the quasi-equilibrium phase of the discharge. Their trends agree with that would be found in continuous wave discharges, with plasma potential and the effective electron temperature decreasing at larger pressures, whilst remaining mostly insensitive to changes in the RF power. Charge carrier density is very sensitive to increasing power as expected, with the density of the discharge also increasing at larger gas pressures.

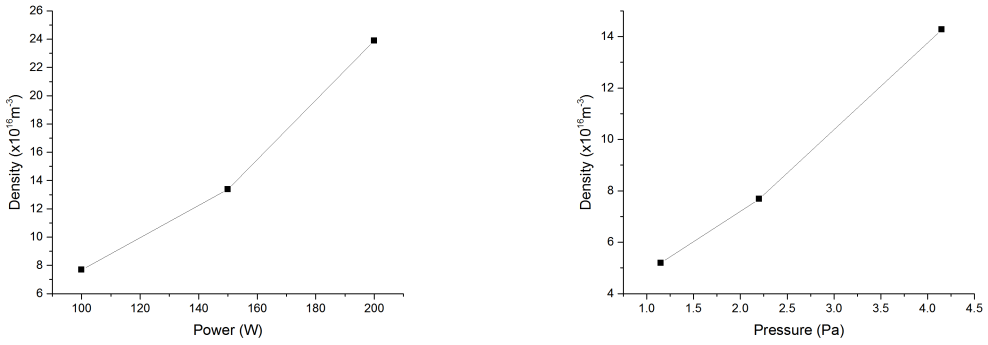


(a) (b)

Figure 4.15: Density values measured in the discharge 200$\mu$s into the activeglow with (a) changing RF power and (b) changing gas pressure.

Plasma densities observed during the quasi-steadysate phase of the pulse agree with Langmuir probe measurements and calculations conducted by Zhu *et al* [130] at the centre of a solenoidal

ICP discharge. For a 100W discharge, they observed electron densities of $5\times10^{10}cm^{-3}$ at 2Pa and 1-1.5$\times10^{11}cm^{-3}$ at 4Pa, whilst at 200W 1-1.2$\times10^{11}cm^{-3}$ with a gas pressure of 2Pa. These values are consistent with that measured at 300$\mu$s in this experiment. Kiehlbauch *et al* [131] simulated a planar coil argon ICP with (dimensions similar to this experiment) and compared with experimental measurements, which report similar values of electron density and temperature to the quasi-steadysate plasma properties observed here. $T_e$ and density measured in this experiment also are consistent with results obtained by Seo *et al* [132], though their work is at a slightly lower pressure of 5mTorr (0.67Pa). Godyak *et al* [133] also reports similar plasma properties measured from a planar coil ICP when operated at comparable gas pressures. Although in this experiment the ICP is driven by a 6.78MHz RF signal, the results are still useful/relevant to this work. A change in the RF frequency affects the high temperature, stochastic heating component of the electron temperature. They report that at 13.56MHz this stochastic component of the electron population is decreased and as a result the effective electron temperature measured is also reduced. However this reduction is small from 6.78MHz to 13.56MHz, decreasing from around 4eV to around 3eV at 1mTorr, so comparison of these results with plasma parameter measurements in this experiment should be valid.

Time evolution of the density is similar to that reported by Ashida *et al* [134], who simulated a planar coil ICP. However their densities are slightly larger than those measured for a 7mTorr discharge in this experiment, most likely due to the fact they recorded the *time averaged* absorbed power of the plasma, so 50W at 10% duty factor would correspond to 500W continuous wave. This is the same case for results reported by Hebner and Fleddermann [135], where a larger plasma density was found for lower pulse duty factors with a constant time averaged power deposited into the plasma. However depositing the same amount energy into the plasma within a shorter time frame will likely not produce the same densities as those measured in a continuous wave plasma. The evolution of the electron temperature observed in these measurements is also similar to that found by Ashida *et al* [136]. Their findings also show that a higher frequency pulse recorded slightly smaller peak values of plasma density in the discharge which could imply that the decrease in plasma density recorded in these measurements may not be entirely due to uncertainties in the probe measurements themselves. As previously discussed, the measured decay of the electron

temperature in the afterglow agrees with the analytical solution to the evolution of $T_e$ presented by Lieberman.

### 4.2.4 Electron Energy Distribution Functions

The EEDF is related to the second derivative of the IV characteristic, as discussed in section 3.1.1. At the plasma potential, there is no potential barrier between the probe tip and the bulk plasma. After subtracting the ion current from the curve (by taking a linear fit of the ion region and using the value of the intercept), the region of the curve biased negatively with respect to the plasma potential, the potential barrier screens lower energy electrons from reaching the tip as the tip is made increasingly negative. The EEDF can provide useful insight into the nature of the electron population in the plasma. An important feature of the EEDF for ICP discharges is determination of whether temperature distribution is maxwellian or bi-maxwellian, as at lower gas pressures stochastic heating of electrons provides a larger component to the effective electron temperature and can become the dominant heating mechanism. Significant stochastic heating will result in two-temperature bi-maxwellian distributions.

As the EEDF relies on the use of the second derivative of the curve, it is intrinsically very noisy and usually the IVs require smoothing before any useful information can be extracted. Argon IV curves were initially interpolated before applying a Savitzky-Golay smoothing function with a second order polynomial to reduce noise before calculating derivatives of the curve.

Figure 4.16 shows the EEDFs calculated from a the afterglow of a 200W argon H mode discharge at 2.4Pa, pulsing at 2kHz with a duty factor of 90%. Even after applying smoothing functions, the second derivative curves are still noisy. This resulted in EEDFs which allow some qualitative observations as to how the energy distribution of the electrons is evolving during the afterglow of the pulse, but with limited ability to extract an electron temperature from the curves. As expected, the high energy tail of the distribution decays away during the afterglow as higher temperature electrons are lost to the walls. The peak of the distribution shifts to lower temperatures and becomes narrower as cold electrons begin to form the dominant portion of the distribution. The rate of decay of the electron temperature also slows as the colder electron temperatures suppress

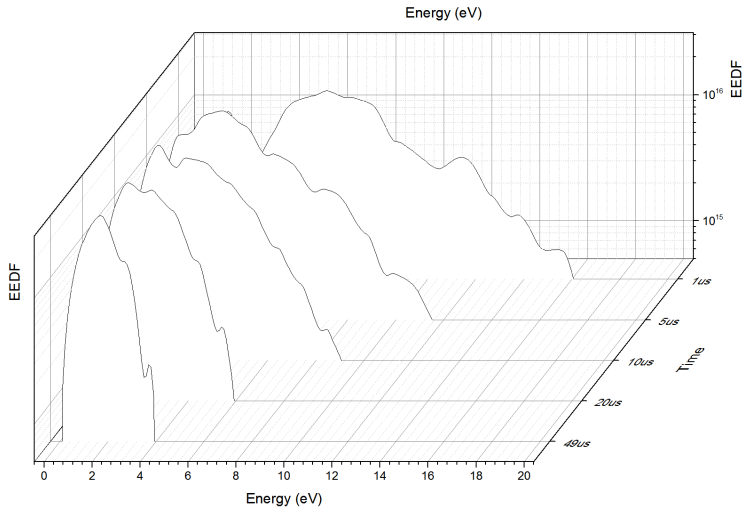


Figure 4.16: EEDFs calculated from the second derivatives of Langmuir IV characteristics measured in the afterglow of a 200W,2.4Pa discharge with a modulation frequency of 2kHz with a duty factor of 90%.

most of the inelastic collision processes.

Whilst the extraction of the EEDF is a powerful tool for characterisation of the plasma source, the accuracy of the probe measurements and large amount of noise in the second derivative curves (even with smoothing) ultimately means no quantitative information can be extracted.

## 4.3 Effect of Grid Bias on Plasma Properties

When functioning as an ion source a bias is applied to the extraction grid in order to draw a current of charged species through into the chamber below. The energy distribution of particles which propagate through the grid is determined by the bias applied and how the plasma above the grid responds to the presence of the bias. As discussed in section 2.5.4 using the correct bias can tailor the shape of the energy distribution and can produce a nearly mono-energetic beam of ions. Measurements were conducted with a constant DC bias applied to the extraction grid at the base of the plasma chamber. In the centre of the plasma the electron temperature should be largely unaffected by the introduction of the electric field from the grid. The equilibrium ion-electron

flux to the chamber walls established by the plasma is perturbed by the presence of an applied continuous DC bias to the plasma grid. [137] demonstrated that the plasma potential in the bulk can be controlled by the use of a biased electrode.

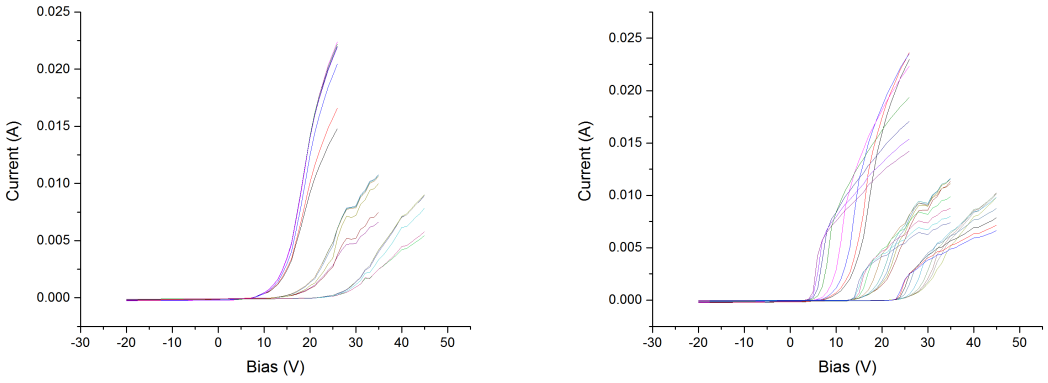


(a) (b)

Figure 4.17: IV characteristics measured with increasing DC grid bias taken in the (a) activeglow of the discharge and (b) the afterglow. Different coloured lines are representative of IVs measured at different times during the activeglow or afterglow, where each set of curves are the IVs measured with a different grid bias applied to the extraction grid continuously throughout the pulse.

Figures 4.17 show the IV characteristics measured in an argon discharge with a floating grid, -10V, 10V, and 20V applied to the grid. The plasma potential of the curves respond to the presence of the electric field established by the extraction grid, causing the floating potential and the plasma to shift to greater values. Figures 4.19 and 4.18 show the electron temperature and plasma potential throughout an RF pulse cycle with different applied grid biases. For positive grid biases, the plasma potential of the discharge essentially increases to the plasma potential plus the applied grid bias, i.e. the potential difference between the plasma and the extraction grid remains constant with increasing applied grid bias. The case is different when a negative bias is applied to the grid as the plasma is unable to shift its potential to be negative with respect to the grounded walls as the electron flux to the walls is still large compared to the ion flux incident onto the biased plasma grid.

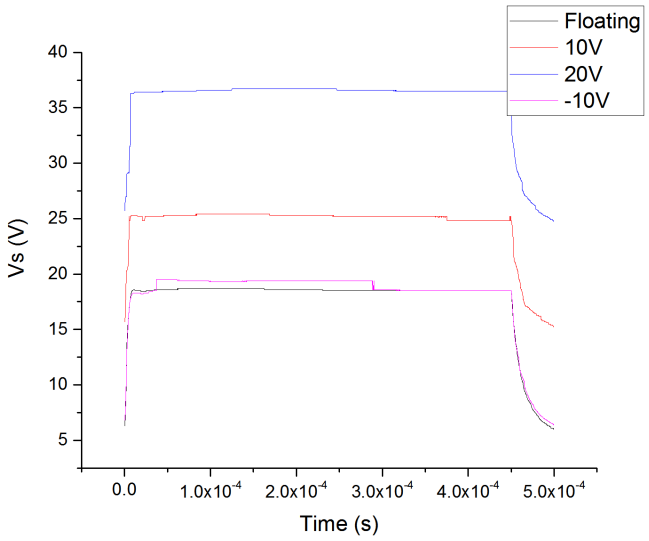


Figure 4.18: Plasma potential measurements in the centre of the discharge with increasing extraction grid bias.

Whilst the plasma potential shifts in response to the grid bias, the electron temperature of the discharge should remain largely unaffected by the presence of the electric field. The grid bias will establish an increased drift of charged species towards the extraction grid, and whilst the losses to the walls has an effect on the electron temperature, the mean free path due to scattering interactions with neutrals has a much larger influence. As the pressure remains constant so should the measured electron temperature. However as the DC bias applied to the extraction grid will establish an electric field between the grid and the grounded chamber around 5.4cm away. The presence of this extra capacitive field could provide some extra heating to electrons near the extraction grid, such as the capacitive heating of the electrons during the late afterglow [87, 88].

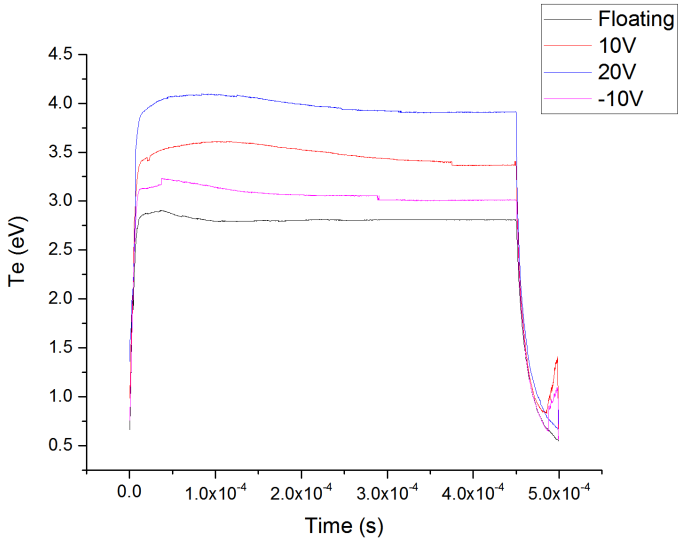


Figure 4.19: Effect of extraction grid bias on the effective electron temperature measured in the centre of the discharge.

Hong *et. al.* [138] measured a change of electron temperature which varied with grid bias in an argon ICP discharge. The source plasma was situated above the biased grid and the recorded temperature change was measured below the grid. They attribute the change in $T_e$ with a reduction in the low energy electron population causing a shift in the measured EEDF. Perhaps if the lower energy electrons are more easily lost to a positively biased grid in this experiment, it could result in an increase in the average energy of electrons in the discharge which would manifest itself as an increase in the measured effective electron temperature.

## 4.4 Retarding Field Energy Analyser Measurements

Ion velocity distribution function measurements were carried out in the plasma bulk using a retarding field energy analyser (RFA). An electron repulsion bias removes electrons and accelerates ions through to a collection electrode which is biased increasingly positively such that only ions with sufficient energies can reach the collector. The RFA was initially positioned inside the bulk plasma, situated close to the edge of the chamber. The electron repulsion grid was biased to -50V, and the bias applied to the collection electrode was swept from -50V up to 30V. As this RFA did not

have a separate grid for collection of ions and filtering of the ion energies, the ions hit the collection electrode with the energy they acquired traversing the sheath into the RFA plus the energy acquired moving the the electric field used to repel electrons. This means that ions collide with the collection electrode with relatively large energies of around 50-70eV in this case.

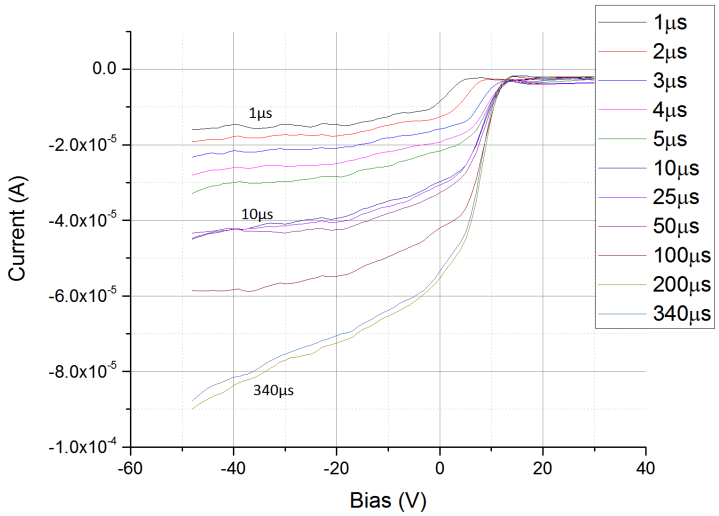


Figure 4.20: Typical IV characteristics measured by the collection electrode of the RFA when positioned in the plasma bulk during the activeglow of the pulse.

IVDFs were measured using a similar technique to the Langmuir probe measurements. The collection electrode was biased and the current collected throughout the RF pulse was measured through an oscilloscope. all of the individual biases were then concatenated, which allowed the IV characteristic for each time step to be extracted.

The IVDF for that time step was then obtained by differentiating the Langmuir curves. Assuming a collisionless trajectory into the RFA the current collected by the electrode is given by

$$I_c = \eta A e \int_{v_{min}}^{\infty} v_i f_i(v) dv \tag{4.2}$$

where $\eta$ is the transmission of the grids within the RFA and A is the collection surface area. The ion velocity distribution $f_i(v)$ can then be obtained through the expression [139]

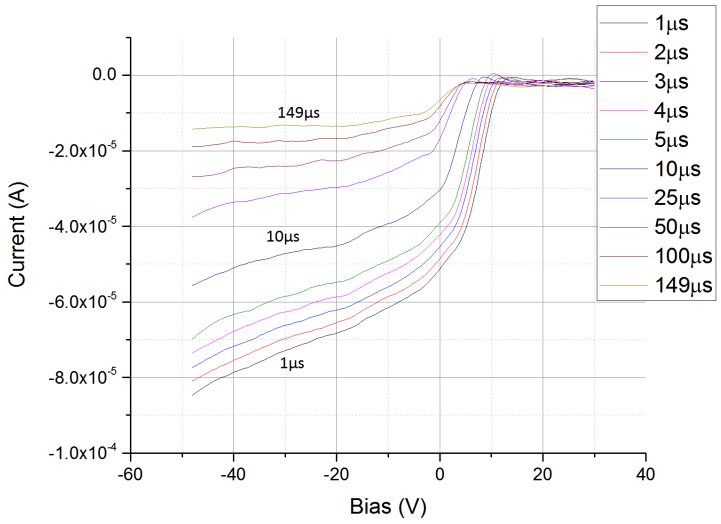


Figure 4.21: RFA collection electrode IV characteristics measured during the afterglow of the pulse

$$f_i(v) = \frac{m_i}{\eta e^2 A}\frac{dI_c}{dV_d} \tag{4.3}$$

Where $V_d$ is the applied collection electrode bias. This results in a set of time resolved IVDFs throughout the RF pulse. Figure 4.22 shows the behaviour of the IVDFs is generally in agreement to that observed in the Langmuir probe measurements. The activeglow IVDFs initially are broad peaks around 50eV as the plasma potential has fallen to close to zero. As power is injected into the plasma the energy peak narrows and shifts to higher energies. Around 4-5$\mu$s the peak is positioned at a higher energy than that measured in the quasi-equilibrium state. This is due to the initial peak/overshoot of the electron temperature and plasma potential as the power is deposited into the initially small electron population. After around 200$\mu$s the plasma has achieved quasi-equilibrium and the velocity peak is situated at the plasma potential (plus the energy acquired as the ions are accelerated through the electron repulsion). The slightly lower energy peak is most likely caused either by noise/some collisions in or close to the sheath resulting in a low energy tail in the distribution or is due to ions being generate inside the RFA itself through collisions of ions with background neutral atoms. The mean free path for charge exchange of $Ar^+$ and Ar at the gas pressure of 2Pa should be on the order of 1cm at thermal energies, which means that the population

of low velocity ions created inside the RFA due to charge exchange should be small.

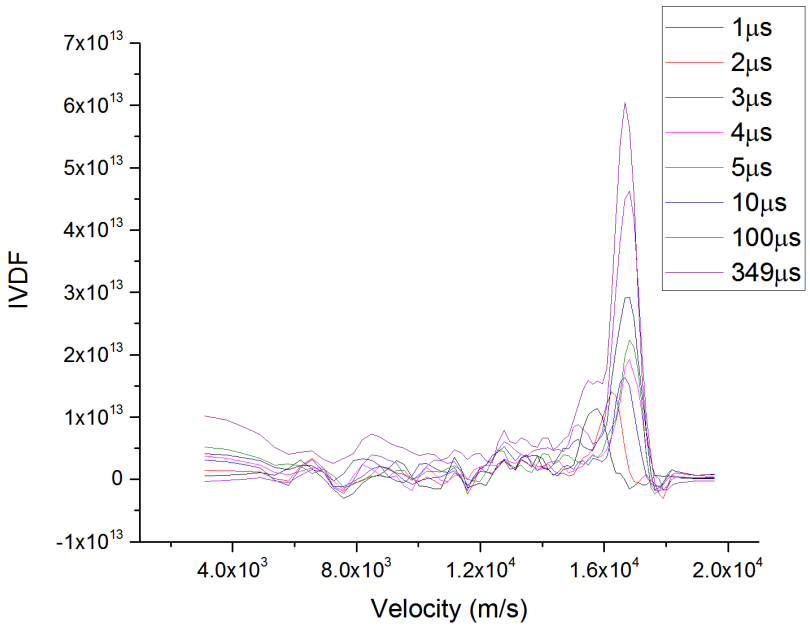


Figure 4.22: IVDFs measured at various time steps throughout the activeglow period of a 2kHz 70% duty factor discharge at 2.4Pa and RF power of 180W.

The ion energies in the afterglow also behave as expected with average velocity and height of the peak decreasing as the plasma potential and electron temperature decay, leading to less acceleration of ions through the sheath into the RFA as shown in figure 4.23. Decrement of the plasma density during the afterglow results in the reduced signal measured. FWHM of the distribution also decreases throughout the afterglow, suggesting that the energy spread of ions collected by the RFA is decreasing. After around 50-100$\mu$s the peak position of the peak changes very little, which corresponds to the time required for the electron temperature to fall below 0.5eV as shown by the Langmuir probe measurements. After this time the decay of the plasma density and potential slows as the population of high energy electrons present at the start of the afterglow have almost entirely vanished to the walls.

In RF plasmas ion velocity/energy distributions are often bimodal distributions with two peaks corresponding to the RF oscillation of the sheath. The IVDFs observed here have a single peak in the distribution which most likely means that the RF oscillations are very small (they are expected

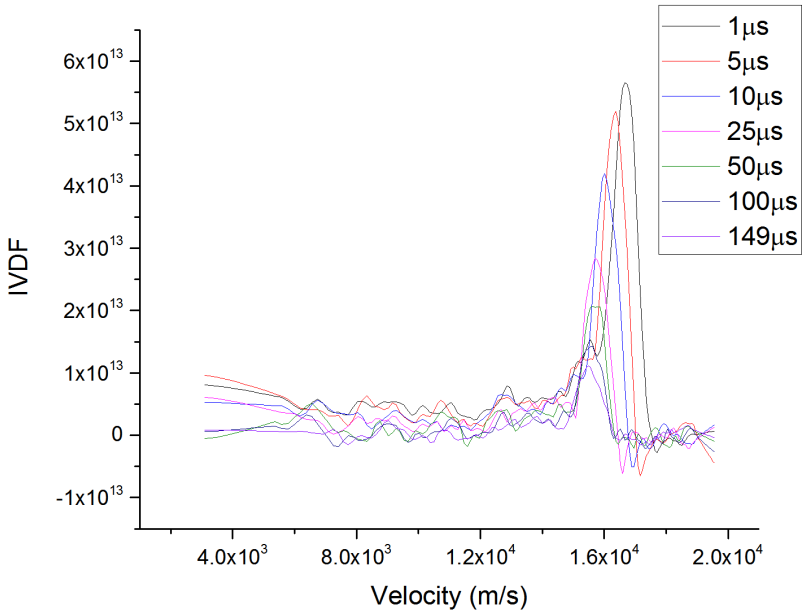


Figure 4.23: Decay of the IVDF during the afterglow of a 2kHz 70% duty factor discharge with 180W at 2.4Pa

to be small in ICP discharges) or the ions traverse the sheath in a time which is much larger than the period of oscillation for the RF field. The Debye length for this discharge can be estimated to be on the order of $4\times10^{-5}$m for 3eV and $10^{17}\mathrm{m}^{-3}$, which gives an estimate for the sheath length on the order of one to a few mm [121]. The Bohm speed for this discharge

$$v_B = \sqrt{k_b T_e / M}, \tag{4.4}$$

where M is the ion mass, gives an estimate for time taken for the ions to traverse the sheath of $4\times10^{-7}$s. RF will complete around 5 oscillations in the time it takes for the ions to move across the sheath, implying ions will only experience a time averaged potential.

The density can be extracted from the distribution function as an integral over the whole curve

$$n = \int_0^\infty f_i(v) dv \tag{4.5}$$

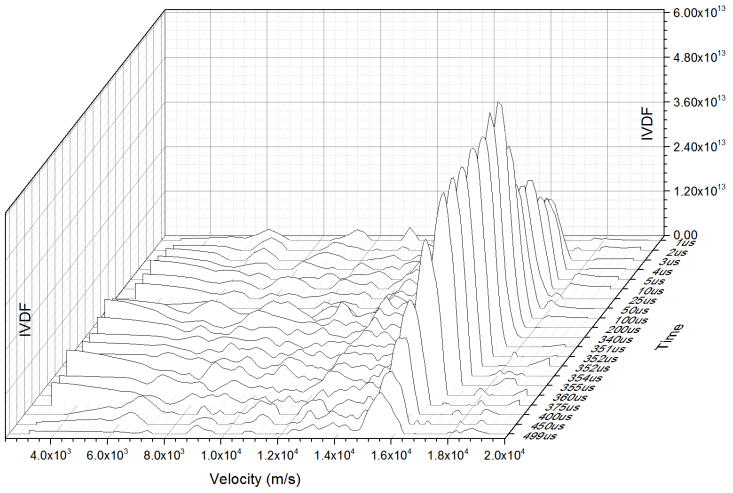


Figure 4.24: Evolution of the IVDF throughout the modulation cycle.

When applied to these IVDFs, the density values obtained for each step in the activeglow and afterglow the RF pulse were found to be largely in agreement with those measured by the OML analysis of the Langmuir probe IV characteristics as shown in figure 4.25b. The larger discrepancy between the probe measurements and the RFA during the quasi-equilibrium phase of the pulse could be due to production of secondary electrons at high negative biases, as if the electrons escape to the walls of the RFA then it will lead to an anomalous larger positive current. This will affect the gradient of the collected current and hence the velocity distribution calculated using equation 4.3.

## 4.5 Conclusion

A temporally filtered ion source based on an ICP discharge has been developed and characterisation of an argon discharge was carried out using a combination of Langmuir probe and RFA diagnostics. Time resolved measurements of $T_e$, plasma density, and $V_p$ with changing pressure, power, duty factor, and pulse frequency were performed. The results show that the plasma properties behave as expected in the pulsed power environment. The initial heating of a small population of electrons

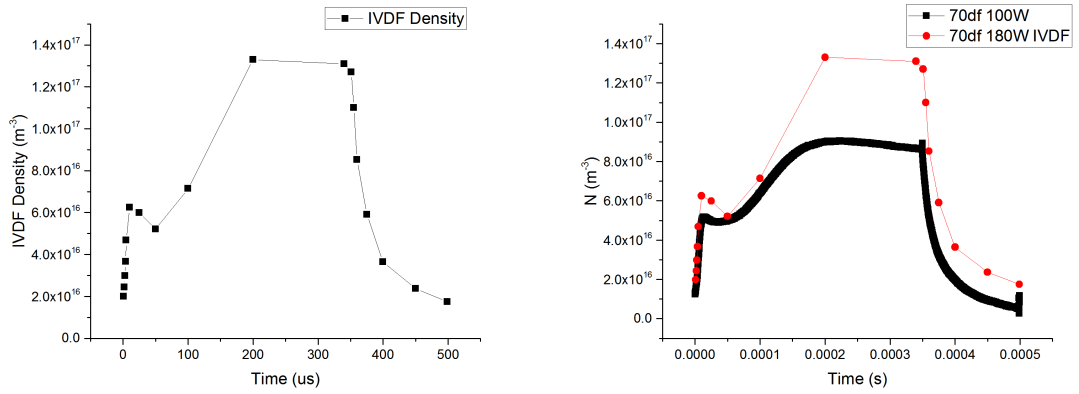


(a) (b)

Figure 4.25: (a) density values calculated from integrals of the IVDFs, and (b) comparison of the RFA calculated density value to the density calculated using OML for similar discharge conditions.

at the start of the pulse cycle results in a small peak or overshoot of the electron temperature and plasma potential. As the plasma then transitions into its quasi-steadystate period of the pulse, $T_e$ and $V_p$ decrease to values representative of those found in a continuous wave discharge. The density slowly climbs to its quasi-steadysate value. During the afterglow $T_e$ and $V_p$ rapidly decayed, with $T_e$ falling to below 0.5eV in around 50$\mu$s. The rate of electron temperature loss in the afterglow slows as the number of inelastic collision processes available to electrons diminishes. The plasma density decays away more slowly as $V_p$ decreases and ambipolar diffusion of charge carriers to the walls slows. EEDF measurements could only provide qualitative insight but indicated that the high energy tail of electrons in the distribution is rapidly lost during the early stages of the afterglow.

Larger RF power increases plasma density with little effect on $T_e$ or $V_p$. Increasing gas pressure reduces $T_e$ and $V_p$ due to increased collisionality whilst increases the measured charge carrier density. Lower pulse duty factor has little effect on the final quasi-steadystate values of $T_e$, $V_p$, and density but increases the overshoot $T_e$ and $V_p$ initial stages of the pulse, and the increase in the density of discharge at the start of the pulse is also shown to be affected by the extended afterglow period. Lastly $T_e$ and $V_p$ are largely unaffected by a change of pulse frequency (within the range of frequencies used in this experiment), whilst the final value of plasma density measured decreases at larger frequencies, most likely due to reduced amount of power deposited in the discharge during each pulse cycle. The decay of the electron temperature agreed with analytical calculations based

on the decay being largely controlled by the loss of particles and kinetic energy through diffusion to the chamber walls, which implied that the primary loss mechanism in this discharge in the afterglow was through diffusion cooling.

When a bias is applied to the extraction grid the plasma potential in the centre of the discharge shifts so that the potential difference between the discharge and the grid remains constant. During the afterglow the plasma potential decays until it matches the bias applied to the grid. The behaviour of the plasma potential throughout the pulse is crucial in determining the energy distribution of any ions extracted from the ion source, which in turn is essential in tailoring the ion energies to fulfil the requirements for dry etching of a substrate or for use in NBI systems.

RFA measurements in the plasma bulk show a sheath potential which agrees with that measured using the Langmuir probe. The single large peak could imply that the RF oscillations in the bulk are indeed small, and Langmuir probe measurements should not require additional filtering, but the more likely explanation is that the ions only experience a time averaged sheath potential as they enter the RFA. The evolution of the Ion velocity distribution also agrees with that observed with the Langmuir probe: a small overshoot in the early stages of the activeglow followed by establishment of a quasi-stable plasma where the distribution changes very little throughout the remainder of the activeglow. The afterglow also demonstrates a rapid decay consistent with that observed with the Langmuir IV characteristics. Finally the density of the discharge calculated by integrating the IVDFs agreed with probe measurements.

The results presented in this chapter have shown that a time modulated argon discharge is capable of large plasma densities during the activeglow with reduced electron temperatures during the afterglow. Whilst argon is not a useful gas for fusion NBI sources the characteristics of high density and a rapidly cooling electron temperature during the afterglow demonstrated by the time modulated ICP discharge shows that this plasma system could prove to be relevant for fusion NBI applications.

# Chapter 5

# Hydrogen Characterisation

## 5.1 Introduction

This chapter investigates the effectiveness of a hydrogen time modulated ICP discharge for use as a volume based ion source/negative ion source. A significant amount work has been carried out in time modulated ICP discharges for highly electronegative gases such as chlorine and fluorine which are often used for dry etching of silicon devices in the semi-conductor industry. A large quantity of both experimental research and modelling have been used to describe the time evolution of charged and neutral species in the pulsed plasma environment[82, 140]. As a result the effect of gas pressure, power, and changing modulation parameters is well documented for these gases. However relatively little effort has been made to investigate pulsed hydrogen discharges.

$H^-$ ion sources require cooling of the electrons in order to reduce collisional detachment losses and maximise negative ion density. Fusion NBI $H^-/D^-$ ion sources make use of magnetic filters to remove the high temperature electrons from the extraction region of the source, in order to limit collisional detachment losses and create optimal conditions for negative ion production and extraction. In time modulated discharges the electron temperature in the plasma bulk rapidly decreases in the afterglow as high temperature electrons are quickly lost to the walls. This creates an ideal environment for the volume production of negative ions and maximises their lifetime in

the discharge. As such temporally filtered $H^-/D^-$ ion sources may be of some relevance as fusion NBI sources.

The objective for this work was the characterisation of a time modulated hydrogen ICP discharge, with measurements to investigate the effect of extracting ions with a DC bias on the plasma properties throughout the chamber. In this chapter the same data acquisition techniques are used as the previous chapter in order to obtain time resolved measurements of a temporally filtered hydrogen discharge. The first section evolution of the plasma properties during the modulation cycle is measured using Langmuir probes in the centre of the discharge and in the extraction region at the base of the chamber. The response of the plasma to a DC bias applied to the extraction grid throughout the pulse both in proximity to the extraction grid and in the centre of the chamber is then discussed. Finally the last section discusses the ion velocity distribution functions recorded in the bulk plasma.

### 5.1.1 Comparison of Hydrogen and Argon Discharges

In contrast to argon, hydrogen gas exists as a diatomic molecule. Molecules have a more complicated electronic structure compared to monatomic gases. In addition to the usual ionisation and excitation of electrons into higher energy bands, the molecule itself can be excited into higher vibrational and rotational energy states as discussed previously in section 2.3.1. The molecular nature of hydrogen also means that there is a more complicated distribution of neutral and ionic species in the discharge.

The possibility for rovibrational excitation means that there is a greater number of electron energy loss mechanisms available through collisions with molecules other than ionisation. This results in a lower efficiency for power deposited into the plasma by the coil resulting in the production of charged species in the gas. As a result hydrogen will have a lower plasma density than argon for similar pressures and input powers. This lower electron density for similar discharge conditions and greater number of inelastic collision channels available means that it is more difficult to reach the threshold electron density required to bring about the E to H transition in the plasma, more input power is generally required for the hydrogen discharge compared to argon.

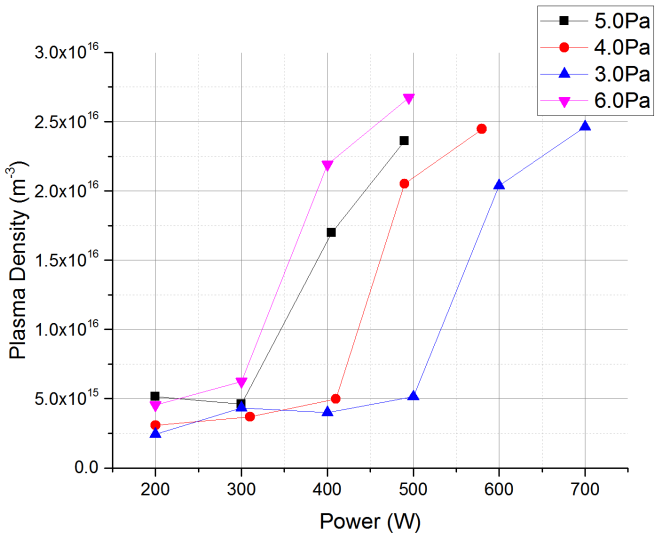


Figure 5.1: Density measurements in the centre of the discharge with changing power at various gas pressures. The sharp rise in plasma density at some threshold value is indicative of a transition to H mode.

Measurements of the plasma density at different powers for various gas pressures were conducted and are shown in figure 5.1. The graph demonstrates the threshold value at which the plasma density rapidly increases as the plasma moves from the capacitive to the inductive mode. A large increase in the emission from the plasma also accompanies this process. The E-H transition is easier to achieve at higher pressures, but higher pressures also leads to increased collisionality within the plasma and reduced the validity of the IV characteristic analysis techniques, as they assume a collisionless sheath. This work was carried out in the parameter space in which the plasma is in the inductive H mode for the increased plasma density and intrinsically smaller RF oscillations in the plasma bulk.

The possibility of negative ion production and there presence in the plasma also affects the behaviour of the discharge when the RF power is time modulated compared to argon. As discussed in section 2.5.3, a large population of negative ions in the plasma affects the decay of the plasma during the afterglow [81]. Electrons quickly lose their energy and are lost to the walls in the initial stages. This process occurs more rapidly in hydrogen because of the larger number of available inelastic energy loss mechanisms. With a large enough $H^-$ density in the discharge, negative ions can become

the dominant negative charge species and an ion-ion plasma can form. This was unlikely to occur during the characterisation stage of the ion source as the plasma was not being operated in order to optimise $H^-$ production. Negative ion densities produced through volume processes such as rovibrational excitation of molecules followed by dissociative attachment will be small, as whilst higher electron temperatures promote excitation of hydrogen molecules to higher vibrational levels they also will easily neutralise negative ions and have reduced DA cross sections.

The naturally lower electron densities in hydrogen leads to larger RF oscillations in the plasma bulk, as the skin depth will be larger than that for argon [25]. In this case the presence of RF obscured the knee of the IV characteristics, in some cases there almost no knee was visible. Whilst the presence of larger RF oscillations will have an effect on the uncertainty in measured plasma parameters, the oscillations are still small enough such that filtering of the RF is not essential.

## 5.2 Evolution of Time Modulated Plasma Properties

### 5.2.1 Data Acquisition for Langmuir Probe IV Characteristics

The same data acquisition process was carried out for hydrogen as the argon discharge, with electron temperature, plasma density, and plasma potential measurements being made for a similar set of pressures, pulse frequencies, pulse duty factors, and input power. The differences predicted between the hydrogen and argon discharges are the reduced plasma density for similar input powers, and a more rapid decay of the electron temperature and charge carrier density during the afterglow due to the greater number of inelastic collision processes available with the molecular hydrogen chemistry.

Characterisation in hydrogen was carried out using two Langmuir probes: one situated in the centre of the discharge chamber, and another positioned approximately one centimetre above the extraction apertures on the plasma grid. All of the initial measurements were carried out with a floating aluminium extraction grid. No Cs alternative materials were applied to the grid at this time. Most of the characterisation was carried out at a gas pressure around 5-6Pa, as the lower power required to achieve H mode reduced the heat load on the matching unit. Unless otherwise stated (i.e. the frequency or duty factor of the pulse is the changing parameter), the plasma was

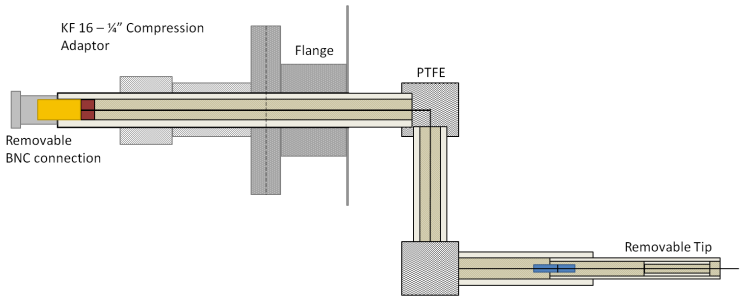


Figure 5.2: Schematic of the probe used to measure plasma properties in the extraction region of the chamber above the plasma grid.

pulsed with a frequency of 2kHz and duty factor of 70%.

The uncertainty/error in the Langmuir probe measurements was estimated by measuring $T_e$, $V_p$, and n in the same discharge conditions repeated over several days. Figures 5.3a, 5.3b, and 5.4 show the resulting average plasma parameter values with the standard deviation calculated from the variance between the different data sets. Larger errors are found on the temperature and plasma potential measurements, in the region of 10% with larger errors in the afterglow as expected due to the decreased signal and fewer number of points available to make fits to the data to extract these parameters. The density was found to have a small error, but one should consider the fact that the OML technique used to calculate the plasma density is an overestimation [124] as the theory itself makes assumptions that may not be entirely valid in this discharge (such as collisionless sheaths). However [126] suggests that OML can still be useful in situations outside of the assumptions the theory makes.

### 5.2.2 Plasma Property Measurements in the Centre of the Discharge

Measurements of plasma properties in the central region of the plasma were carried out using the centrally positioned Langmuir probe. The typical evolution of the electron temperature and density for a hydrogen discharge is shown in figure 5.5. During the initial stages of the pulse the loss rate of ions is negligible, and as the ionisation rate is also initially small due to the low electron temperature (ionisation rate is strongly dependent on $T_e$), the electron temperature very sharply rises at a rate

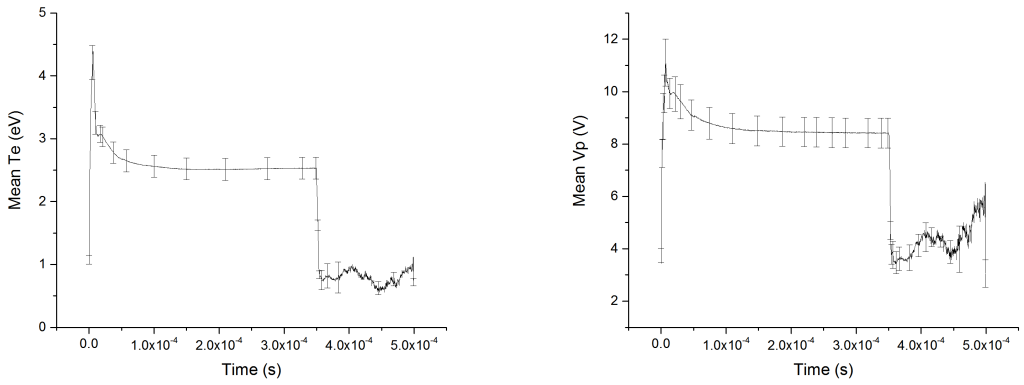


(a) (b)

Figure 5.3: Average (a) $T_e$ and (b) $V_p$ measured in the centre of the plasma along with the standard deviation of those measurements throughout the pulse.

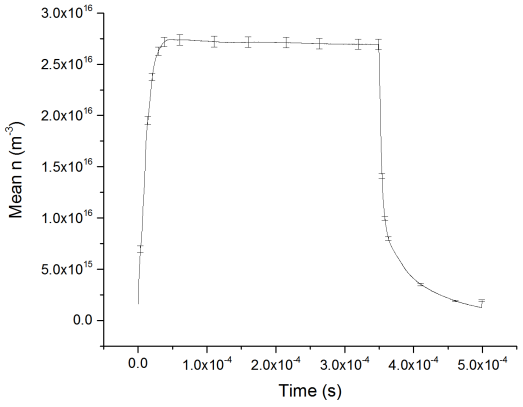


Figure 5.4: Average OML density calculations and the standard deviations throughout the pulse in the centre of the plasma.

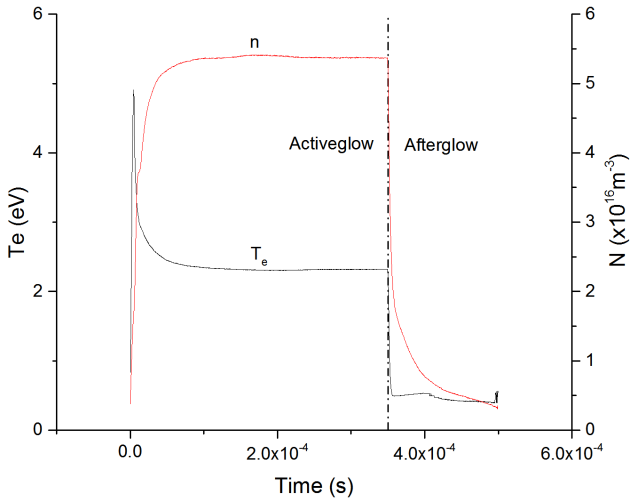


Figure 5.5: Evolution of $T_e$ and density in the centre of the chamber throughout the modulation cycle of a 2kHz 70% duty factor 690W discharge, with a gas pressure of 5.9Pa.

$$\frac{1}{T_e}\frac{dT_e}{dt} \approx \frac{P_{max}}{W_e}, \tag{5.1}$$

to a maximum as discussed in section 2.5.2. After moving through a sharp peak and achieving some maximum value, $T_e$ will then decrease down to its quasi-steadystate value. The plasma density increases more slowly and smoothly until it plateaus at the equilibrium value [77, 78]. During the afterglow high temperature electrons are rapidly lost to the walls and $T_e$ cools quickly. The rate of temperature decrease is then reduced as cooler electrons are diffuse to the walls much more slowly, and other energy loss mechanisms such as ionisation are no longer accessible. The plasma density decreases at a slower rate as the plasma potential decays and the ions are no longer accelerated towards the chamber walls. Typically the electron temperature will fall below 0.5eV in around 10$\mu$s.

Figures 5.6 show the evolution of the electron temperature, plasma density and plasma potential with changing input power. The response of these parameters in similar to that observed in argon: $T_e$ and $V_s$ are weakly coupled and so largely unaffected by an increase in power, whilst the charge carrier density of the discharge increases with larger input power. Electron temperature depends

weakly on the power deposited into the plasma and is affected more by the particle losses to the effective chamber dimensions. $T_e$ may decrease at high powers as the charge carrier density of the discharge becomes larger. Although [141] suggests that electron temperature may have stronger coupling to plasma power then previously thought, and that gas heating must also be considered.

During the initial peak in the electron temperature of the early activeglow, it should be noted that the assumption that the electron population is Maxwellian is likely to be invalid. At this stage in the pulse the electron density is small and the average energy of these electrons is large compared to that observed in the quasi-equilibrium phase of the pulse. To define the electron population at this point with a Maxwellian temperature may be incorrect. As we assume a Maxwellian distribution of electron energies when calculating $T_e$, the accuracy of these measurements during the first few microseconds of the pulse may not be completely reliable. However this region is small relative to the period of the activeglow and should not affect measurements made throughout the rest of the activeglow/quasi-steadystate phase of the discharge.

The decay rates of $T_e$ and $V_p$ in the afterglow are also much more rapid for hydrogen than for argon with the electron temperature falling to below 0.5eV typically after 50$\mu$s in an argon discharge, whilst the decay of Te in a hydrogen plasma takes closer to 10$\mu$s to fall to less than 0.5eV. Typical density values measured are in the low $10^{16}m^{-3}$. The uncertainty in the measured electron temperature becomes larger during the later stages of the afterglow, this is because the temperature is taken as the inverse of the gradient of a linear fit between the floating potential and the plasma potential. Since $V_p$ rapidly decays in the afterglow, the number of points available for the linear fit diminishes which results in a larger uncertainty in the gradient as the fit becomes more sensitive to fluctuations in the current measured by the probe. This can lead to erratic behaviour of the calculated value of $T_e$ at later times in the afterglow.

Figures 5.7 are the results from measurements made at different gas pressures. As expected, the electron temperature and plasma potential increase as the pressure is reduced due to decreased collisionality in the discharge and a larger mean free path for electrons. Fewer average collisions will result in a larger high energy population of electrons and increased average electron temperature. The decrease in pressure also leads to a more prominent peak in $T_e$ and the $V_p$ during the initial heating stages of the pulse due to lower electron populations at the end of the afterglow. The

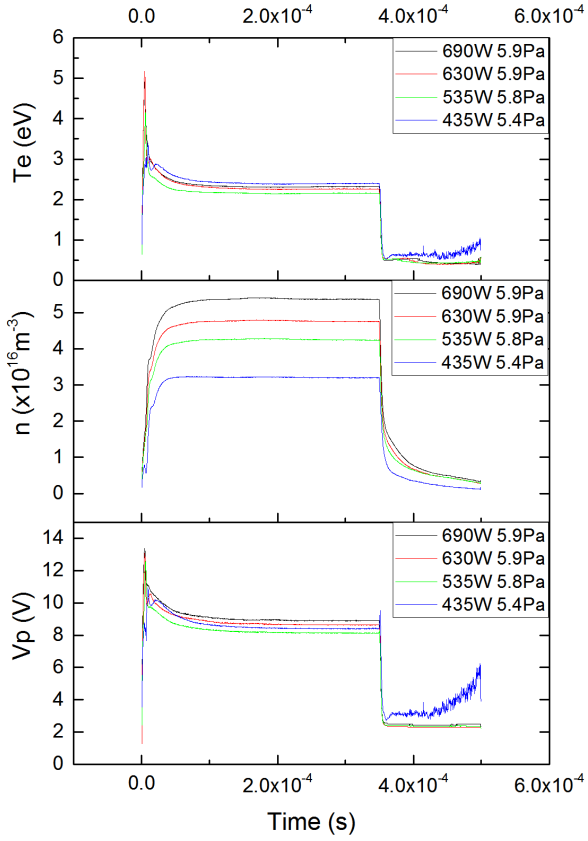


Figure 5.6: Measured effect of increasing power on plasma properties in a 2kHz 70% duty factor pulse, with a gas pressure of 5.4-5.9Pa in the centre of the plasma.

overshoot is not entirely visible for the electron temperature at 3.4Pa, but this is due to the analysis method used to extract the plasma parameters from the IV characteristics being unable to find enough points to find a linear fit in the semi-log plot of the transition region. Data at 3.4Pa also displays a greater plasma density than the IV characteristics measured at higher pressures, but this is due to the fact that this discharge required a higher power in order to maintain a stable inductive mode throughout the time taken to measure the IV characteristics.

In a hydrogen discharge increasing gas pressure also affects the ratio of ion populations in the discharge. Molecular hydrogen dominates the neutral species population and it could be expected that $H_2^+$ composes the majority of ions present in the plasma. The rate coefficient for the production of $H_3^+$ ions is large, which resulting in a significant population of $H_3^+$. At large gas pressures, $H_3^+$ can

begin to be the dominant ion (see for example [142], operating at 90mTorr or 12Pa) present in the plasma, whilst at lower pressures $H_2^+$ can dominate with a larger fraction of $H^+$ also in the discharge. OML relies on the mass of the incident ion for the calculation of the ion density. If the average ion mass has shifted due to the change in the ratio of charged species, this could result in a larger uncertainty or underestimation/overestimation in the calculated density. From [143, 144] it can be estimated that the dominant species in the discharge at the pressures used in these measurements will be $H_3^+$. It is difficult to know the absolute number densities of the ionic species in the plasma as the ionic lines are small and difficult to resolve relative to the neutral spectral lines, and require a model in order to extract quantitative information on the species ratios. As a result the average ion mass had to be estimated for this work.

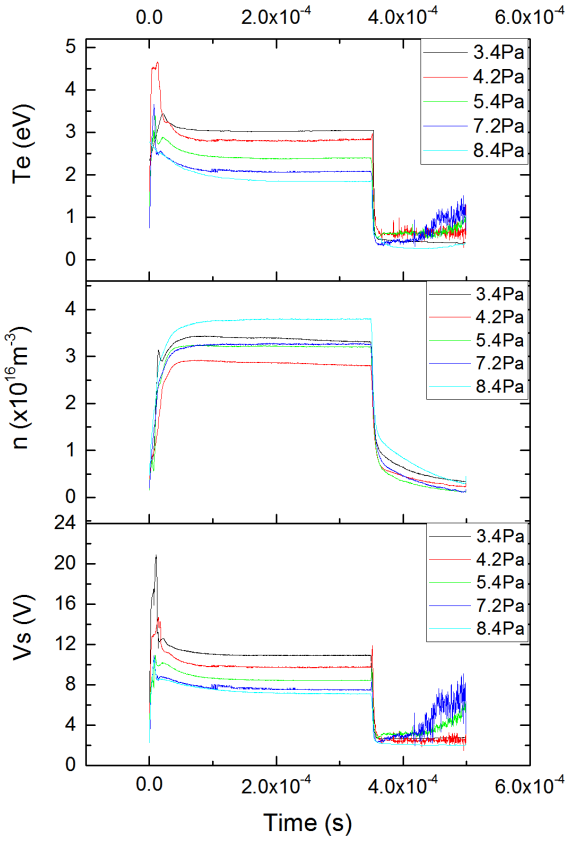


Figure 5.7: $T_e$, $n$, and $V_p$ measurements in the centre of the plasma with increasing gas pressure throughout a 2kHz 70% duty factor pulse. Power is kept fixed at around 420W.

Variation of Te, Vs, and $n$ with changing pulse frequency are shown in figure 5.8. $T_e$ and $V_p$ remain consistent and largely unaffected by the changing pulse frequency, with quasi-equilibrium values of 2.5eV and 9V respectively. Provided that the pulse frequency is low enough such that the period of the activeglow and afterglow do not detrimentally affect the initial heating of electrons and enough time is provided for the plasma to establish an equilibrium, then changing of the pulse frequency should have little affect on the activeglow values of $T_e$, n, and $V_p$. At these relatively low pulse frequencies of 1-10kHz, the 70% duty factor provides an activelgow period long enough to establish the quasi-equilibrium phase of the pulse. Maximum density values measured during the pulse remain constant for pulse frequencies of 1-5kHz. 10kHz density is smaller than other frequencies, this is either due to uncertainty in the probe measurements or the short activeglow period leading to a smaller rovibrationally excited molecule density in the plasma. Vibrationally excited molecules have a long lifetime in the plasma, on the order of 1ms. Ionisation and collisions with these excited molecules can result in high energy particles which can assist with further ionisation in the discharge. The peak during the initial heating in the afterglow decreases at larger frequencies due to the shorter afterglow period and larger plasma density at the beginning of each pulse.

Duty factor of the 2kHz pulse was varied from 30-90%, with a gas pressure of around 5.5Pa and input power of 420-435W. Figure 5.9 shows the final electron temperature achieved in the plasma's quasi-equilibrium state was observed to be the same for duty factors ranging of 90% to 30% at around 2.5eV. The same trend is observed for the plasma potential, with all duty factors achieving similar steady state values of 9V. Provided the discharge has enough time to enter the quasi-stable phase of the pulse, then the pulse duty factor should not have a significant effect on the plasma parameters, as is observed in figure 5.9. The pulse frequency in these measurements is 2kHz and so even at low duty factors of below 50% the time scale of the activeglow period will be on the order of hundreds of microseconds, which is large compared to plasma heating and ambipolar diffusion time scales. The effect of low duty factors on these parameters may become more apparent when operating at higher pulse frequencies. The initial overshoot of the $T_e$ and $V_p$ becomes more pronounced as the duty factor decreases, largely due to a reduced electron density remaining from the end of the previous pulse.

The plasma density measurements in figure 5.9 are less consistent but are still reasonably within

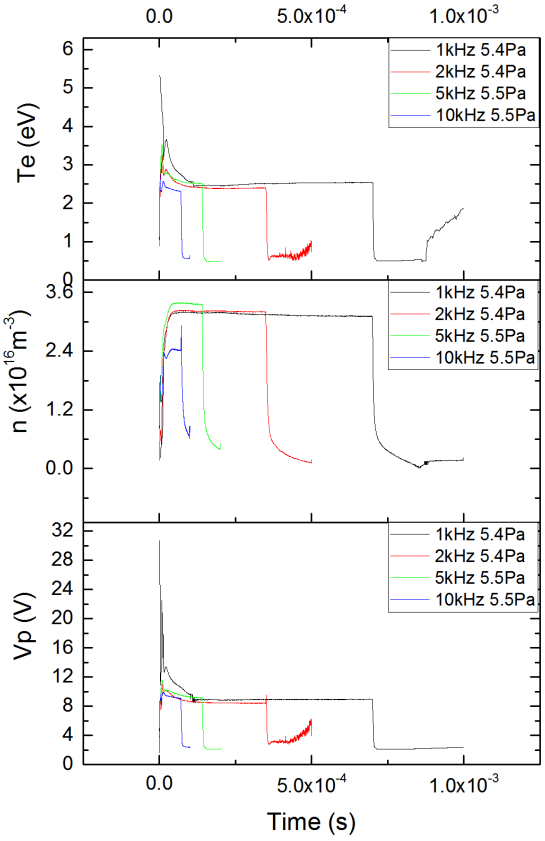


Figure 5.8: The effect of changing modulation frequency on plasma properties in the centre of the discharge. Pulse duty factor remained fixed at 70%, with a gas pressure of 5.4-5.5Pa and 420-430W.

error of each other. Data was taken for a discharge with a 30% duty factor, but there was a much greater difficulty maintaining H mode at low duty factors. As a result this data had to be measured at a much higher power, around 570W. Even at this power it could be easily seen that the discharge was struggling to remain in H mode. The density of the plasma will be affected by changes in pulse duty factor as the populations of certain charged species in the plasma can only be increased during the activeglow period. It has been reported that for lower pulse duty factors the measured electron density in a chlorine discharge was larger relative to that measured in a plasma with a longer activeglow period. This was due to the changing population ratio of Cl to $Cl_2$ at lower duty factors and their lower ionisation energy results in more ionisation during the activeglow, and larger measured electron densities [6]. $H^+$ ions are largely produced through the

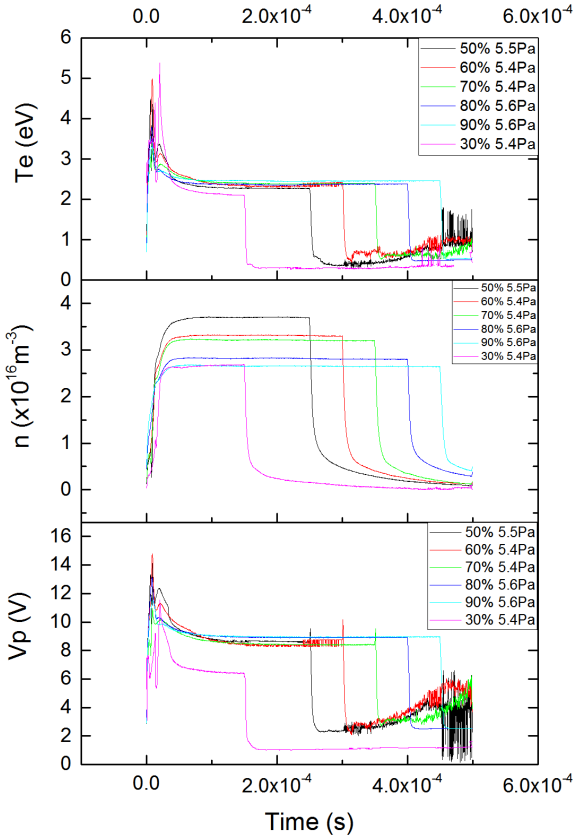


Figure 5.9: Plasma property measurements with changing pulse duty factor in the centre of the chamber. Modulation frequency was fixed at 2kHz, with a gas pressure of around 5.5Pa and input power of 420-430W.

dissociation of $H_2$ molecules by high energy electrons and the subsequent ionisation of the neutral H atoms. At lower pulse frequency and duty factor, the short activeglow and proceeding extended afterglow may result in a significantly smaller $H^+$ density in the discharge compared to discharges with shorter afterglow periods.

Due to the presence of some distortion due to RF in probe measurements meaningful second derivatives of IV characteristics could not be extracted, even with interpolation and smoothing. This meant that electron energy distribution functions or electron energy probability functions could not be measured with the Langmuir probes. It was assumed that the distribution of electron energies were Maxwellian when performing the probe analysis. Typically ICP discharges are bi-

Maxwellian with two populations of electrons with different temperatures: one population due to collisional Ohmic heating, and a high energy tail from collisionless heating as electrons interact with the RF field in the skin depth. At lower pressures the collisionless heating has a much greater contribution as the energy relaxation length is larger than the chamber dimensions and the energy distribution measured by the probe is affected by the global kinetics of the electrons. At higher pressures collisional heating will dominate and the energy acquired by electrons through sheath interactions will be lost collisionally before they are able to reach a probe positioned at the centre of the discharge.

The energy relaxation length of electrons in the discharge is given by [145]

$$\lambda_e \approx 2\sqrt{D_e \left(\nu_{ee} + \delta\nu_a + \nu^*\right)^{-1/2}} \tag{5.2}$$

where $\nu_{ee}$, $\nu_a$, and $\nu^*$ are the collision frequencies for ionisation, elastic collisions, and inelastic processes, and $\delta = 2m_e/M$. $D_e$ is the electron diffusion coefficient given by

$$D_e = \lambda_e \nu / 3 \tag{5.3}$$

Without the inclusion of inelastic processes (which form a substantial contribution) this gives a relaxation length of around 30cm when operating at 1Pa, which is the same as the chamber diameter. Including the inelastic terms and operating at higher pressures will shorten this length, i.e. the higher energy electrons lose their energy collisionally and suppress the bi-Maxwellian distribution.

### 5.2.3 Measurements in the Extraction Region

When the ICP discharge is operated as an ion source, the current density and composition of the beam will be determined by the plasma parameters and population of charged species in proximity to the extraction grid. As a result it is essential to also carry out a set of plasma parameter measurements both in the centre of the discharge and close to the plasma grid. Due to the nature of the planar coil set-up of the plasma, the RF power is deposited into the plasma within the skin

depth close to the coil and quartz window on the opposite side of the chamber to the extraction system. the pressure with which the source was operated the mean free path for electrons and recombination path length for ions was smaller than the chamber dimensions. As a result the plasma density is expected to be slightly lower in close proximity to the extraction grid compared to the densities recorded at the centre of the chamber. If the energy relaxation length of the electrons is larger than the chamber dimensions the electron temperature should be homogeneous throughout the plasma, however elastic and inelastic collisions will affect this relaxation length and result in an inhomogeneous $T_e$. Again, unless otherwise stated the pulse parameters used in the following measurements were 2kHz with a 70% pulse duty factor. All of the measurements presented in this section were conducted with a floating extraction grid.

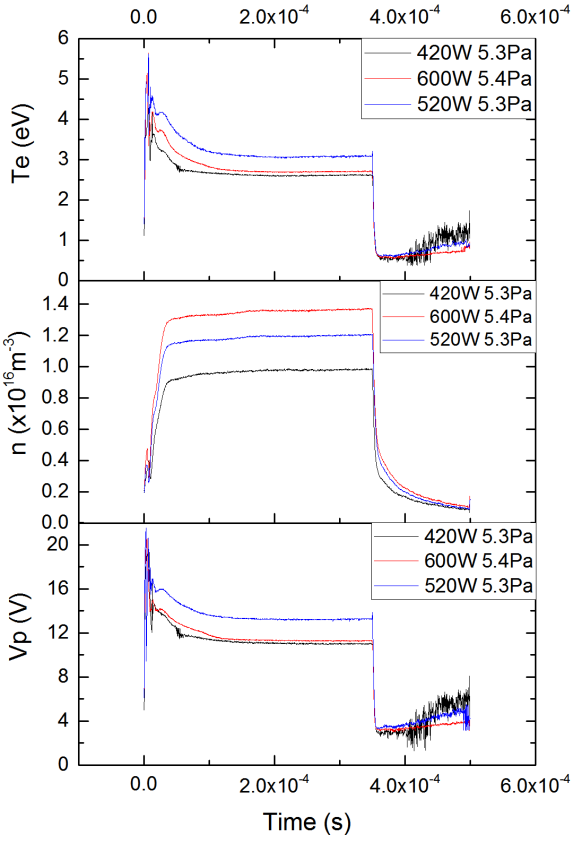


Figure 5.10: Measured effect of increasing power on plasma properties in a 2kHz 70% duty factor pulse in the extraction region of the plasma.

Figure 5.10 shows $T_e$, the plasma density $n$, and plasma potential $V_p$ measured next to the extraction grid for various input powers. Similar to that measured in the centre of the discharge, $T_e$ and $V_p$ are largely unaffected by changes in RF power and achieve similar final values during the quasi-equilibriated phase of the pulse. As expected, plasma density is observed to increase with power. At 200$\mu$s into the activeglow, $T_e$ and $V_p$ were measured to be around 3eV and 12-14V respectively. Equilibrium values of density increased with power, but remained consistently smaller than the densities found in the centre of the chamber.

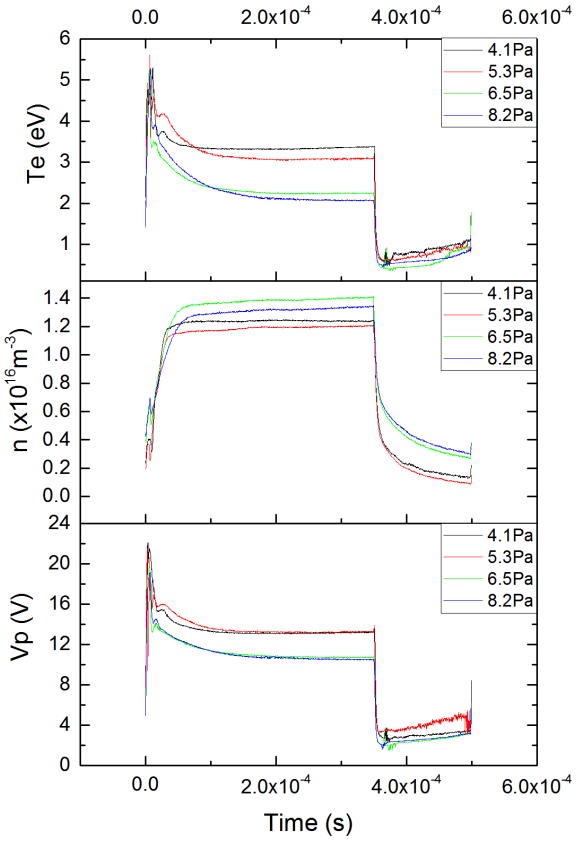


Figure 5.11: Measured effect of increasing power on plasma properties in the extraction region of the plasma for a 2kHz 70% duty factor pulse with 420-460W.

The changes in $T_e$, n , and $V_p$ again follow expected trends for changing gas pressure, as shown in figure 5.11. The reduced mean free path resulting from an increased density in background neutrals again leads to a decrease in the final values of $T_e$ and $V_p$ achieved during the quasi-equilibrium

phase of the pulse. Density also increases with gas pressure as the ionisation mean free path is reduced by the larger neutral density. As explained in the previous section, the density calculation may be affected by a shift in the ratios of ionic species in the plasma as at higher pressures $H_3^+$ can begin to dominate, and at lower pressures the higher average electron energy can result in more dissociation of hydrogen molecules and a larger population of $H^+$ ions.

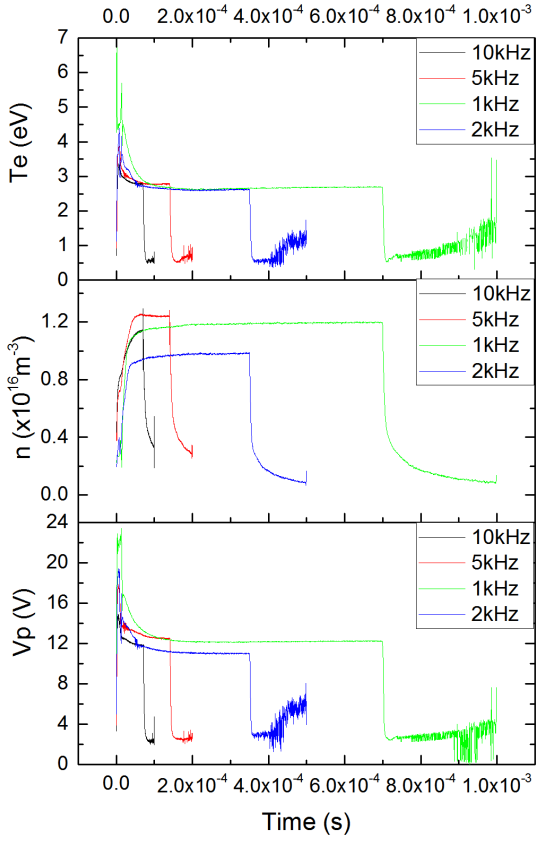


Figure 5.12: $T_e$, $n$, and $V_p$ with changing modulation frequency in the extraction region of the plasma with a fixed duty factor of 70%, operating at 425W 5.0Pa.

Pulse frequency has the same effect as observed in the centre of the plasma, little effect on the quasi-steadystate values measured for $T_e$, n , and $V_p$ within the frequency range of 1-10kHz. Again this is likely due to the activeglow period being long enough to not significantly affect the establishment of the quasi-equilibrium phase or the ratios of charged particle species or ground state/excited neutral particles in the discharge. The overshoot in $T_e$ and $V_p$ is larger for lower frequency modulation

due to the extended afterglow.

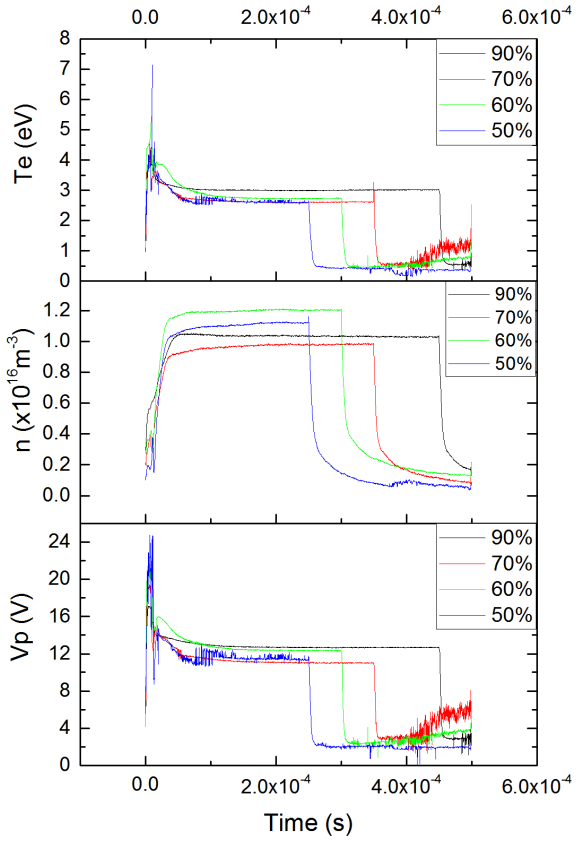


Figure 5.13: Effect of changing pulse duty factor on plasma properties in the extraction region of the discharge. Pulse frequency remained constant at 2kHz with a gas pressure of 5.0-5.2Pa and 425W.

The response of $T_e$, n , and $V_p$ to changing duty factor also remains consistent with that observed in the centre of the chamber. For duty factors ranging from 50-90%, or activeglow period of 250-500$\mu$s, the final equilibrium values of electron temperature and plasma potential remain constant. However the overshoot in $T_e$ and $V_p$ during the early stages of the activeglow increases with decreasing duty factor as the increasing afterglow periods leads to an increasingly smaller electron population at the start of the next pulse as the plasma is being heated.

The Debye length for this plasma estimated using an electron temperature of around 3eV and density on the order of $10^{16}m^{-3}$ is around $10^{-4}$- $10^{-5}$m. From the calculations in [121] we can

estimate of the sheath size in the discharge to be around $10^{-2}$- $10^{-3}$m (assuming some collisionality in the plasma) in the centre of the discharge. This will increase close to the extraction grid due to the reduced plasma density.

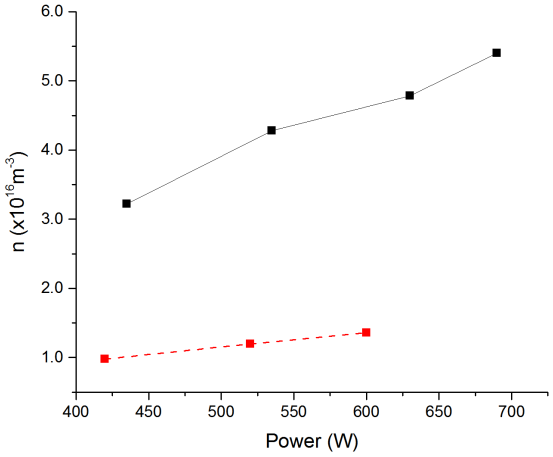


Figure 5.14: Measurements of the plasma density in with increasing power in the centre of the discharge and next to the extraction grid 200$\mu$s into the pulse. Solid line and dashed line are measurements for the centre and extraction grid region respectively.

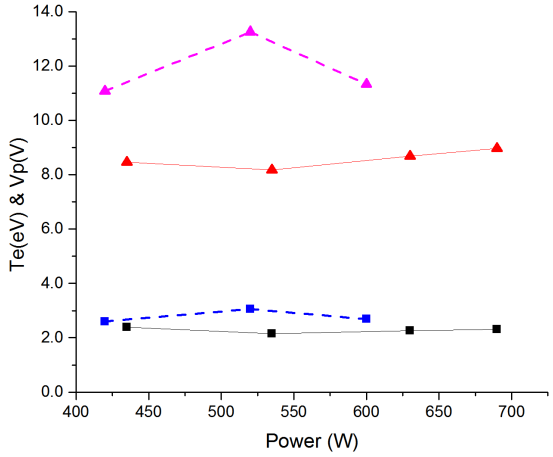


Figure 5.15: Measurements of $T_e$(squares) and $V_p$(Triangles) with increasing power in the centre of the discharge and next to the extraction grid 200$\mu$s into the pulse. Solid line and dashed line are measurements for the centre and extraction grid region respectively.

Figures 5.14 and 5.15 depict the behaviour of $T_e$, density, and $V_p$ both in the centre of the discharge

and in the extraction region with varying input power. All of these measurements were recorded with a 2kHz pulse frequency and 200$\mu$s into the activeglow period to ensure the plasma had reached its equilibrium. As previously discussed the temperature and plasma potential remain largely unaffected by the increasing RF power. The electron temperature is the same in the centre of the discharge as it is in the extraction region which is a good indication that the electron energy relaxation length of the discharge is on the order of or larger than the chamber dimensions. $V_p$ appears to increase in the extraction region of the plasma. It is unclear what the cause of this is, as it would imply that a potential barrier for ions has formed in front of the extraction grid. As the estimation of the sheath size (around 1cm) is close to the distance between the extraction grid and the probe (also around 1cm) it could mean that the probe is positioned partially or in the sheath or pre-sheath region. The grid was also floating during these measurements so the existence of some potential build up onto the surface of the grid affecting the plasma in the immediate vicinity and modify the plasma potential.

Another potential explanation for the difference in $V_p$ between the centre and extraction regions of the discharge could be due to the presence of negative ions. Due to the higher mobility of the electrons the negative ions are confined to the centre of the discharge. This process can result in a plasma with an electronegative core and electropositive outer regions near the walls. The transition from the core to the electropositive edge leads to a change in the positive ion flow velocity closer to the walls of the chamber. Assuming the negative ions have a much lower temperature than the electrons, they only require a small field to confine them to the core and the change in Bohm criterion moving between electropositive and electronegative regimes could result in a discrepancy between the plasma potential measured by the probe in the centre of the discharge and the probe positioned in the extraction region.

Even with the disagreement in the actual value of the plasma potential between the two probes the relationship with RF power is the same: increasing power has little effect on $V_p$. The density of the discharge falls to around 30% of its value measured at the centre when in the extraction region.

steady state values of $T_e$ and $V_p$ in both the centre and extraction regions demonstrate the same trend with increasing pressure, as shown figure 5.16. Density should show a clearer increase but as discussed above the assumption that the dominant ion in the discharge for OML calculations

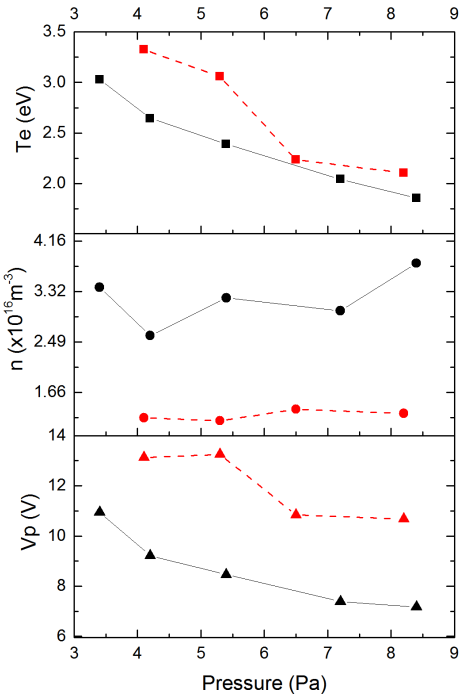


Figure 5.16: Central and grid measurements of $T_e$, density, and $V_p$. Solid lines represent values recorded in the centre of the plasma, dashed lines are for those measured next to the extraction grid.

remains the same is likely to be incorrect.

$T_e$, $n$, and $V_p$ are all unaffected during the quasi-stable phase of the pulse by changing duty factor, both in the centre and in the extraction region as shown in figure 5.17. Grid densities remain at 30-40% of those found in the bulk plasma, and $T_e$ remains constant across both probes. A disparity still exists between the grid and the bulk for $V_p$ as discussed previously, but both sets of measurements remain constant at different duty factors during the activeglow.

For both the centre and extraction regions, during the afterglow the electron temperature and $V_p$ decay rapidly for around 10$\mu$s after which the decrease slows down as electrons are now only lost through recombination and diffusion to the walls. As the uncertainty in these values increases at later times in the afterglow, it is difficult to determine quantitatively if there is any differences in the decay rates between the two regions. The decay of the plasma density begins to slow down after 10$\mu$s for both the extraction region and the centre of the plasma, which agrees with the time

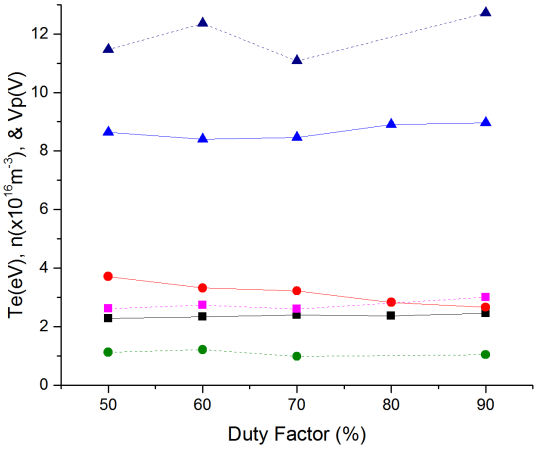


Figure 5.17: $T_e$, density, and $V_p$ measured both in the centre of the discharge and next to the extraction grid 200$\mu$s into the pulse. solid lines represent measurements from the centre of the plasma, dashed lines were recorded by the extraction grid. The squares, circles, and triangles correspond to $T_e$, density, and $V_p$ respectively.

required for the rapid decay of $T_e$ and $V_p$ to slow. The rate of density decay is insensitive to changing RF powers, but does depend on gas pressure most likely due to collisions with neutrals slowing diffusion to the walls of the chamber (figures 5.18a and 5.18b ).

A lot of work has been carried out in time modulated ICP discharges for highly electronegative gases such as chlorine and fluorine which are used frequently for dry etching of silicon devices in the semi-conductor industry. As a result the effect of gas pressure, power, and changing modulation parameters is well documented for these gases. However relatively little effort has been made to investigate pulsed hydrogen discharges.

The densities measured in an RF ICP hydrogen discharge reported in [65] agree with the results presented here across the range of gas pressure and input power. The evolution of the electron temperature and plasma density measured in a time modulated discharge also agrees with the trends observed in the probe measurements carried out in this experiment and in results presented in [64], though these experiments were carried out at higher powers in a filamented plasma source.

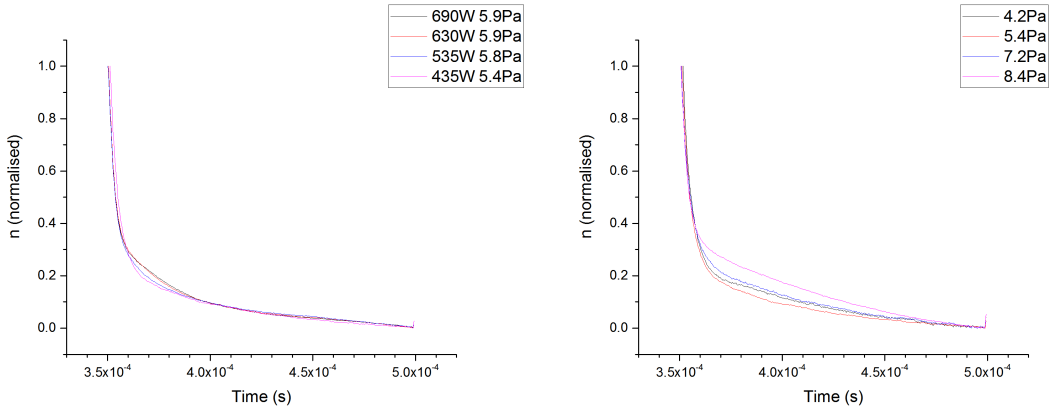


(a) (b)

Figure 5.18: Effect of changing discharge conditions (a) power (b) pressure on the decay of the density during the afterglow in the centre of the chamber

### 5.2.4 Effect of Grid Bias on Plasma Properties

All of the measurements carried out in the centre of the plasma and close to the extraction apertures were conducted with the plasma grid electrically floating. When extracting ions from the discharge DC or RF biases are applied to the plasma grid to generate a flow of charges towards a sample or substrate (or an acceleration system in the case of NBI beamlines). When applying a continuous DC bias to the plasma, the equilibrium ion-electron flux to the chamber walls is perturbed. The plasma potential of the system is expected to increase in response to the presence of the applied bias as shown in [137], where the plasma potential of the bulk was controlled by a biased electrode. The potential difference between the plasma bulk and the plasma grid remains constant during the activeglow. However as the plasma potential quickly falls away during the afterglow $V_p$ and the potential difference between the grid and the plasma does not remain constant. $V_p$ rapidly changes to match the DC bias applied to the extraction grid and allows control of the ion energy distribution during the afterglow. Measurements of discharge were carried out in the centre of the chamber and in the extraction region of the system with various DC biases applied continuously to the plasma grid. If the surface area of the extraction grid is of a similar size to the surface area of the chamber walls, then an application of a bias to the grid could alter the plasma parameters of the discharge. It has been suggested [138] that biasing of a grid within the plasma allows some control over the

electron temperature and density of the discharge as well the plasma potential. This is usually in the diffusion plasma away from the further downstream from the source

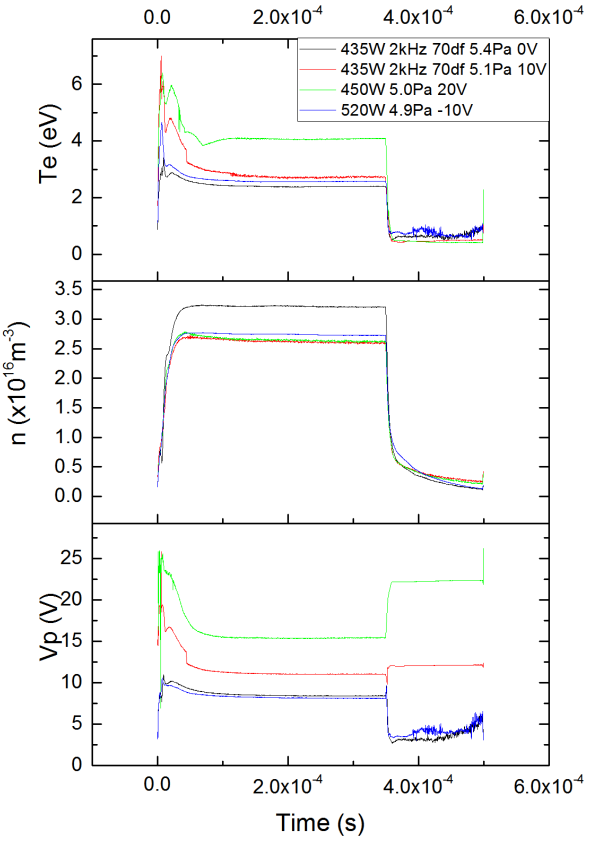


Figure 5.19: Plasma property evolution with changing extraction grid bias for a 2kHz 70% duty factor modulation cycle, measured in the centre of the discharge.

Figure 5.19 shows the plasma parameters measured in a 2kHz 70% duty factor discharge with various DC biases applied continuously to the extraction grid throughout the pulse, measured with a Langmuir probe positioned in the centre of the plasma. As expected the plasma potential is measured to increase with larger grid biases. However in contrast to that observed with an argon plasma, $V_p$ does not increase to maintain a constant potential difference between the grid and the plasma during the activeglow. However this behaviour changes during the afterglow where the potential difference now is constant with increasing positive grid bias. The plasma potential remains unchanged by the application of a negative grid bias to the extraction grid, including during the

afterglow. $T_e$ and $n$ remain unaffected by the presence of the grid bias.

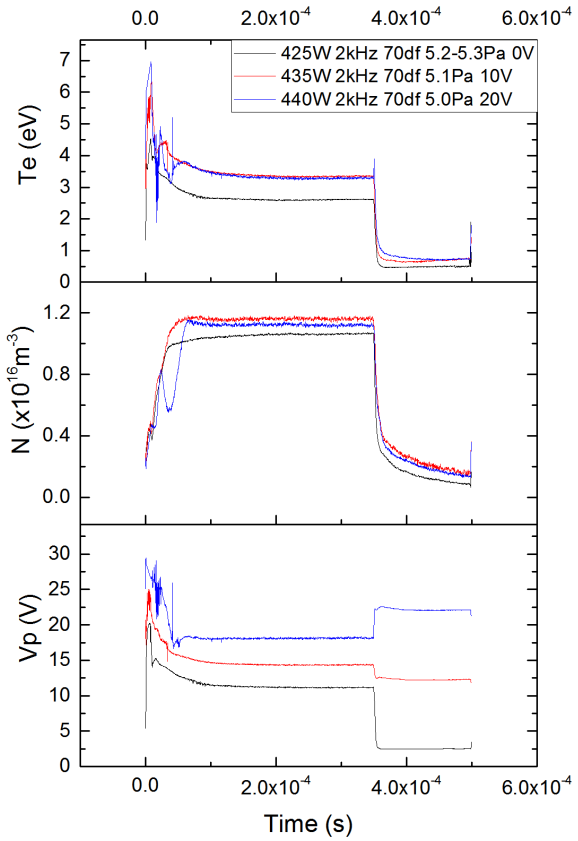


Figure 5.20: Effect of grid bias on plasma properties measured above the extraction grid in a 2kHz 70% duty factor.

The response of the plasma parameters to the DC bias close to the extraction grid is shown in figure 5.20. Similarly to the centre of the discharge $n$ and $T_e$ remain essentially constant with increasing grid bias. Behaviour of the plasma potential is also the same as observed in the centre of the discharge: increasing with larger applied bias, but the potential difference between the plasma potential and the extraction grid does not remain constant. Optical emission spectroscopy measurements of line ratios for the Balmer series also remained constant, implying that the temperature of the electrons was unperturbed by the grid bias.

The source characterisation in argon demonstrated that the plasma potential measured by the probe in the centre of the discharge increased by an amount which matched the positive bias applied to the

grid, i.e. the potential difference between the plasma and the grid remains constant. The response of the plasma potential to the DC bias in hydrogen is observed to be different. When a positive bias is applied to the extraction grid the measured plasma potential in the centre of the discharge and in proximity to the grid increases, and this shift is larger for increasingly positive grid biases. However the increase of $V_p$ does not match the applied bias and the potential difference between the grid and plasma is not constant. During the afterglow $V_p$ quickly changes to match the grid potential. It is expected that the hydrogen discharge is more collisional than argon, estimation of mean free paths is on the order of 1cm for momentum exchange for the gas pressures used in this experiment (using cross sections from [146, 147]) This could provide an explanation to the less pronounced effect of the grid bias on the plasma potential as collisions could reduce the ability of the electric field established by the grid to penetrate into the plasma, in a similar fashion in Langmuir probe theory where collisions affect sheath formation and the sheath's ability to affect the local plasma parameters .

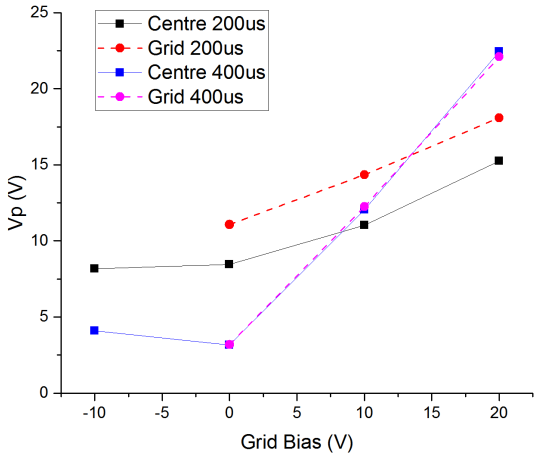


Figure 5.21: Comparison of the plasma potential measured in the centre of the discharge and in the extraction region 200$\mu$s into activeglow, and 50$\mu$s into the afterglow of a 2kHz 70% duty factor discharge.

Sirghi *et. al.* [148] discusses strong or weak coupling of the grid bias to the plasma potential, and in the case of weak coupling the ion saturation current collected by a negatively biased grid is smaller than the electron saturation current collected by the chamber walls. This means that the

plasma potential is unable to follow the grid bias and remains constant as the DC grid bias becomes increasingly negative. Figures 5.19 and 5.21 show $V_p$ changes very little when applying a negative bias to the extraction grid. This implies that the grid is indeed weakly coupled to the plasma. Figure 5.21 also shows that the measured difference in $V_p$ between the centre and grid regions of the plasma disappears during later stages of the afterglow. This could be due to negative ions no longer being confined to the core and the plasma is no longer separated into an electronegative core and electropositive outer regions. As a result there is no longer a shift in the ion flow velocities and a more homogeneous plasma potential.

During the afterglow the plasma potential now increases or decreases in order to maintain a small but constant potential difference between $V_p$ and the grid bias. In slight contrast to the activeglow this behaviour more closely matches that observed when biasing an argon discharge. This can be explained by the decay of the plasma in the afterglow leading to larger sheath sizes and the plasma reduced ability to effectively screen the field produced by the DC bias. For collisionless sheaths the sheath width depends more strongly on the plasma density than $T_e$ [121] , so the plasma density decay in the afterglow will result in an increase in the sheath width. For collisional regimes the coupling of the sheath width to the plasma density and electron temperature is more complicated, but generally the sheath width will still increase as the charge carrier density diminishes.

## 5.3 Measurements of IVDFs in the Plasma Bulk

Similarly to the measurements conducted in argon, the retarding field energy analyser (RFA) was used to measure the velocity distribution of ions in the plasma bulk. The RFA was positioned a few centimetres away from the centre of the plasma chamber. The electron repulsion grid bias was set to -30V. The bias applied to the collection electrode was swept from -30V to 30V in 1V steps, with larger voltage steps taken in regions with less information, i.e. most of the region where the collector was negatively biased. In the RFA used in these measurements the electrode which collects the ion current and the electrode which screens lower energy ions with an increasingly positive bias are the same electrode. This means that the velocities/energies of incident ions onto the collector are shifted by 30eV as they are initially accelerated through the electric field established by the

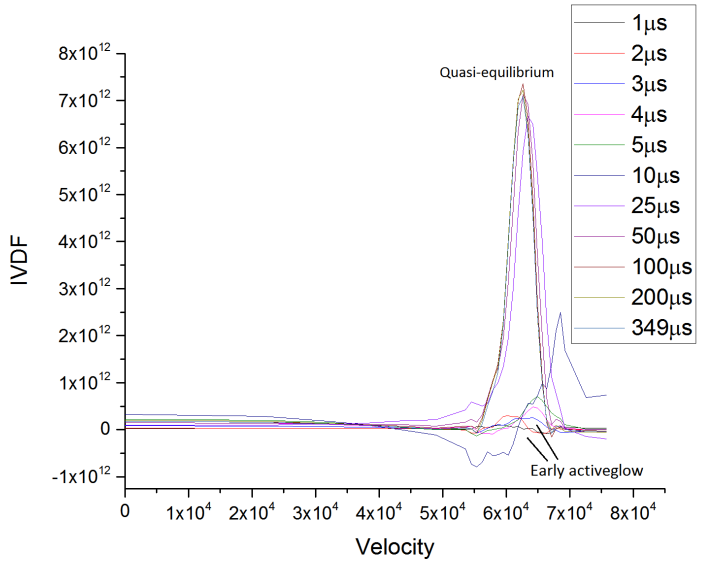


Figure 5.22: IVDFs measured in the plasma bulk of a 2kHz 70% duty factor discharge operated at 2.7Pa with 580W. The centre of the peak corresponding to the sheath potential rapidly increases during the early stages of the activeglow. after around 25$\mu$s the plasma moves into the equilibrium stage of the activeglow and there is little change in the IVDF at later time steps.

electron repulsion grid.

The presence (or lack) of a low energy tail in the IVDFs give a qualitative indication of the amount of collisionality in the plasma, which provides more information on the validity of the OML technique used to extract ion densities from probe characteristics. As OML assumes a collisionless sheath, a significant low energy region in the IVDFs would imply that this assumption is incorrect.

IVDFs were measured in hydrogen at feeding gas pressures of 3Pa,4Pa, and 5Pa. A pulse frequency of 2kHz with a 70% duty factor, and an forward power of 580W was maintained for the measurements. At all three pressures the IVDFs largely exhibit the same behaviour for the activeglow and afterglow of the RF pulse. Figure 5.22 shows as the pulse begins and power is deposited into the plasma, a small peak in the IVDF begins to emerge as the electrons are heated and ionisation processes begin. This peak has a higher average velocity and is broader than the distribution measured in the quasi-equilibriated plasma. The IVDF becomes noisy with no real discernible peak at 10$\mu$s as the plasma moves into the initial period of low density, high electron temperature. After this period the plasma moves into quasi-equilibrium, where the average velocity decreases slightly and

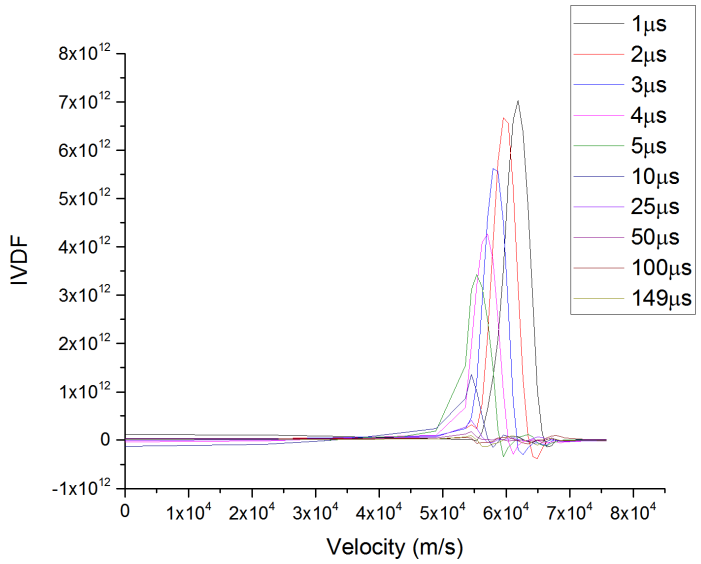


Figure 5.23: IVDF during the decay of the plasma in the afterglow of a 2kHz 70% duty factor discharge operated at 2.7Pa with 580W measured in the plasma bulk.

the peak intensity increases to its maximum, see figure 5.22. These observations agree with the evolution of the plasma parameters found with the Langmuir probe characteristics.

The evolution of the IVDF in the afterglow demonstrates similar traits to those observed in argon. Figures 5.23, 5.24b, and 5.25b shows the measured IVDF throughout the afterglow of 3Pa, 4Pa, and 5Pa discharges. The height and centre of the distribution peak decreases rapidly as the density of the discharge and plasma potential decay away. The full width half maximum (FWHM) of the peaks is also decreasing with time implying a reduction in the energy spread of the ions entering the RFA. The peak of the distribution increases as the gas pressure is lowered due to the increase in the increase in electron temperature and plasma potential accelerating ions to higher energies as they move through the pre-sheath and sheath outside the grounded grid of the RFA.

At higher pressure runs (4Pa & 5Pa) the peak of the IVDF is distorted by contributions from lower velocity ions, implying increased collisionality in the plasma bulk as more charge exchange collisions between ions and background neutrals will result in a larger population of lower velocity ions in the discharge. Some noise from the RF sheath oscillations will exist on top of the signal due to low energy ions, so it is difficult to say with absolute certainty how collisional the plasma is

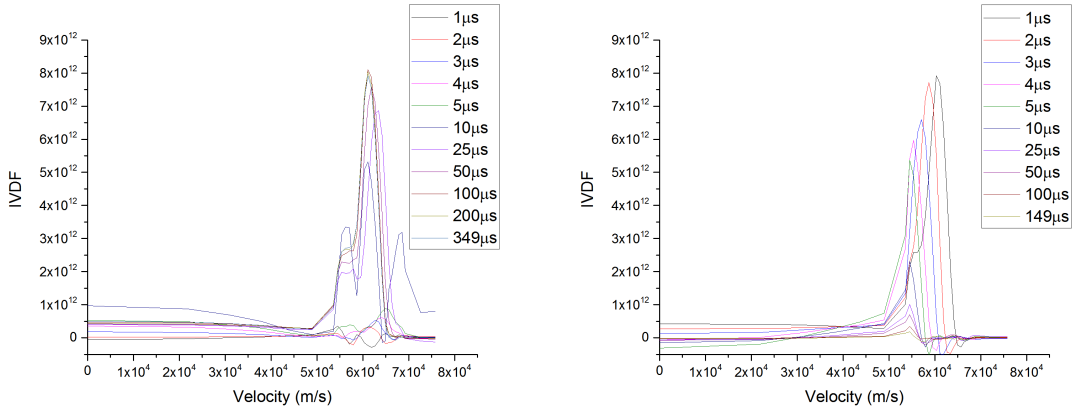


(a) Activeglow (b) Afterglow

Figure 5.24: IVDFs measured in the bulk of a 3.9Pa 70% duty factor, 3.9Pa, 590W discharge in the (a) activeglow and (b) afterglow.

based purely on these IVDFs. Secondary electron emission from the collection electrode will also contribute to uncertainty in the current measurements at lower collection grid bias due to a large flux of high energy ions colliding with the surface. This should be suppressed by the negative bias on the repulsion grid forcing these electrons back to the collector surface.

The energy distribution of the ions collected by the RFA should be the energy acquired by ions moving through the sheath plus the energy gained as the ions are accelerated by the negative potential of the repulsion grid. This allows an estimation of the time averaged sheath potential in front of the RFA's grounded grid. Figure 5.26 shows a comparison between the calculated plasma density and sheath potential in front of the RFA to those measured using the Langmuir probe positioned in the centre of the chamber for two discharges with similar conditions. The probe and RFA measurements are found to be largely in agreement throughout the pulse. Some discrepancy appears at later stages in the afterglow but the uncertainty in both measurements becomes larger as the plasma density decreases and signal to noise diminishes.

If the RF oscillations of the sheath are large, one would expect the energy/velocity distribution of the ions to have a bi-modal distribution with two peaks due to the ions moving through the sheath as the RF oscillates between the two extrema, as discussed in section 2.5.4. The distributions measured here do not have any obvious saddle structure which would imply that either the RF

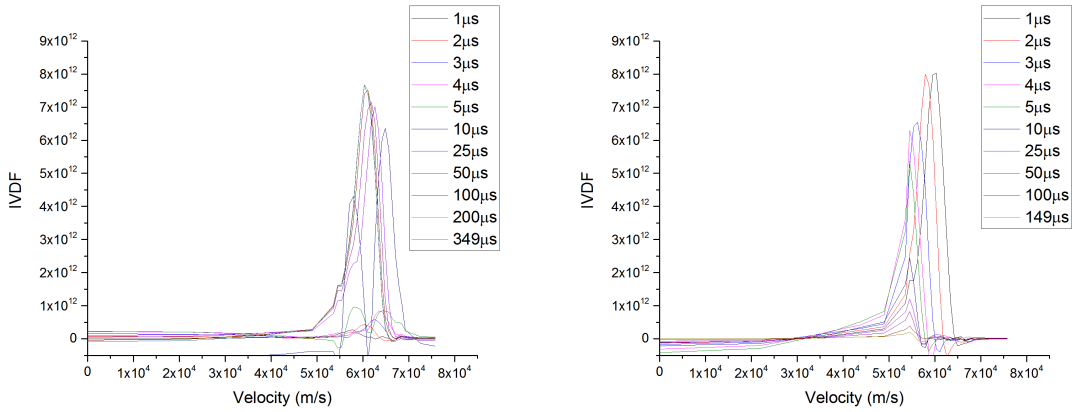


(a) Activeglow (b) Afterglow

Figure 5.25: IVDFs measured in the bulk of a 2kHz 70% duty factor, 4.8Pa, 580W discharge in the (a) activeglow and (b) afterglow

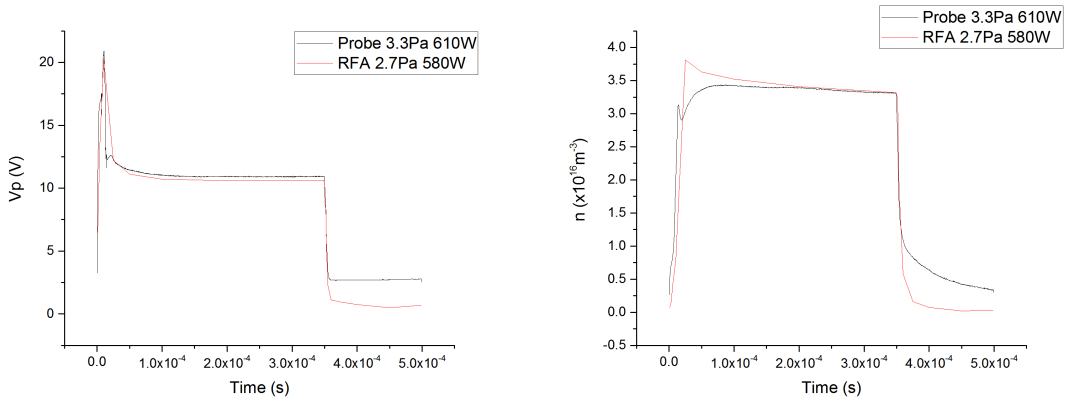


(a) (b)

Figure 5.26: Comparison of the evolution of (a) the sheath potential and (b) density from Langmuir probe measurements and IVDF measured in the plasma bulk for similar discharge conditions.

oscillations are small (which is expected due to the ICP plasma damping the radiation) or that the transit time of the ions across the sheath is large compared to the time scale of the RF oscillations, causing the ions to only experience a time averaged sheath potential. The sheath thickness decreases with increasing collisonality in the plasma which reduces the crossing time for the ions, however if the plasma is highly collisional then the ions will not enter the sheath with the sound speed as the short path length prevents ions from accelerating to full speed. The Debye length in this discharge with an electron temperature of around 3eV and plasma density of $10^{16}$ is on the order or $10^{-4}$m, which when assuming a collisionless sheath gives an estimated sheath length of around $10^{-2}$m using calculations based on [121]. In a collisionless discharge the ions will approach the sheath with a velocity greater than the sound speed (or Bohm speed) of the plasma

$$v_B = \sqrt{k_b T_e / M}, \tag{5.4}$$

where M is the ion mass. Using typical electron temperature of around 3eV from the Langmuir probe measurements yields a sound speed around $10^4$ ms$^{-1}$. Even without the acceleration provided by the sheath the ions will cross the sheath in $10^{-6}$s, around ten times the period of the RF oscillation at 13.56MHz. This means that the ions will only see a time averaged sheath potential, and explains why the ion velocity distributions contain only a single peak.

## 5.4 Conclusion

Characterisation of a time modulated planar coil hydrogen ICP discharge has been conducted using time resolved Langmuir probe and RFA diagnostic techniques. The temporal behaviour of the plasma parameters followed the expected trends throughout the pulse cycle. As power is deposited into the plasma at the beginning of the pulse, the electron temperature and plasma potential increase rapidly due to the low initial electron population and small electron loss rate. This results in a large overshoot in $T_e$ and $V_p$ before they decrease down to their equilibrium values for the remainder of the activeglow period. The plasma density increases more slowly and more smoothly reaches its equilibrium value. During the afterglow, high temperature electrons are quickly lost

to the walls resulting in a rapid decay of the plasma potential and electron temperature. This decay rate slows as the cold electron population remains and loss processes such as ionisation cease. The plasma density decays more slowly in the afterglow as ions and cold electrons are lost to the walls and through recombination processes. The loss rate of ions to the walls also slows as $V_p$ quickly decreases and the ambipolar electric field diminishes. $T_e$ cools to less than 0.5eV in around 10$\mu$s, whilst plasma density decays more slowly as ions and cold electrons diffuse to the walls. The initial faster rate of density decrease is slowed after 10$\mu$s due to the loss of the high temperature component of the electron population and flux of particles to the walls decreases.

Langmuir probe characteristics were recorded in the centre of the discharge and close to the extraction grid. Increasing the RF power results in larger plasma density, with little effect on $T_e$ or $V_p$. As the feeding gas pressure is increased $T_e$ and the plasma potential decrease as the electrons experience more collisions in the discharge and their average energy decreases. The large spike in $T_e$ and $V_p$ also becomes more pronounced at lower pressures due to the reduced electron densities at the end of each pulse. Plasma density increases with larger gas pressures. Changes to pulse frequency and duty factor also were observed to have little effect on the evolution of $T_e$ and $V_p$ in the frequency range of 1-10kHz. Lower pulse frequencies or reduced duty factors resulted in a larger peak in $T_e$ due to the extended afterglow period leading to small electron populations at the beginning of the next pulse.

Probe measurements were also conducted in the extraction region of the discharge, in close proximity to the extraction grid. Plasma density in this region was found to be 30-40% of the density found in the centre of the discharge, whilst electron temperature was constant across the vertical dimensions of the chamber. A discrepancy was found between $V_p$ measured in the centre and close to the plasma grid, which was likely due to the floating potential on the grid affecting the local plasma properties, though may have some connection to the difference in electronegativity between the core of the plasma and the outer extraction region.

Application of a positive DC bias to the extraction grid resulted in an increase in the measured plasma potential. However the potential difference between the plasma and the extraction grid did not remain constant. Negative biases resulted in no change in $V_p$. This is probably due to a weak coupling of the electric field from the grid to the plasma, as the currents moving to the grounded

walls are always much larger than that drawn by the grid.

RFA measurements of the discharge were performed in the plasma bulk to obtain IVDFs of the plasma at various gas pressures. The resulting IVDFs contained a single peak centred around the energy acquired by ions as they move through the sheath and the electron repulsion field. The evolution of the distribution, the calculated plasma density, and sheath potential agree with the trends observed from measurements made with Langmuir probes.

The results presented demonstrated a high plasma density in the activeglow, together with temporal filtering of the electron temperature in the afterglow. These features of the discharge mean that time modulated hydrogen discharges may be of use as fusion NBI ion sources. Whilst many modelling and experimental studies have been carried out in the area of pulsed ICP discharges with high electronegativity, there has been relatively little work conducted into time modulated hydrogen discharges. The research carried out in this project into the time evolution of hydrogen plasma properties and their response to an extraction bias in the pulsed environment should form a useful contribution to the field.

# Chapter 6

# Boron Doped Diamond as a Cs Alternative Material

## 6.1 Introduction

ITER will make use of Cs in its NBI negative ion sources, however large amounts of Cs will not be sustainable for long term NBI operation and will inevitably lead to increased reactor down time. Cs must be used much more efficiently or alternative materials to Cs have to be identified and utilised for enhancing surface production of $H^-/D^-$ ions. One of the candidates which has shown some promise is boron doped diamond (BDD) [100]. The aim of work conducted in this chapter was to test the effectiveness of BDD as an enhancer of negative ion production in a time modulated plasma environment. The structure of this chapter is as follows: Section 6.2 discusses measurements of the plasma properties in the extraction region of the chamber with BDD surrounding the extraction apertures, as well as a comparison to measurements without BDD; section 6.2.2 reports the effect of a DC extraction bias on the plasma properties; 6.3 then discusses IV characteristics measured of the extracted beam below the grid; IVDF measurements near the extraction grid (plasma grid) are then presented in section 6.4; finally the effect of exposure to the hydrogen discharge on the BDD samples is then reported in section 6.6.

The boron doped diamond used in this study was a synthetic polycrystalline diamond produced through chemical vapour deposition (CVD) with a micro-crystalline structure. CVD uses a hydrocarbon gas and a plasma discharge to generate radicals and reactive species to dissociate molecules, where carbon is then collected onto a substrate on which the diamond crystals grow. The conditions usually favour the production of graphite but growth is suppressed as the plasma easily removes graphite from the surface, allowing the creation of very pure polycrystalline diamond samples. Impurities such as boron can also be added during the CVD process in order to produced doped diamond structures. Natural diamond behaves as an electrical insulator, however when doped with boron atoms it begins to act as a conductor.

Carbon is supposed to enhance the surface production of $H^-$ ions through the electronic structure preventing electrons from tunnelling back to the surface once attached to the affinity state of the H atom as beam experiments reported in [95, 96] reported high negative ion yields from high workfunction surfaces. However it has also been suggested that the main channel through which diamond samples enhance the negative ion production in the discharge is actually through enhancement of the conditions required in the plasma for *volume* production of negative ions. Results reported in [149] suggest that the presence of the BDD affects the bulk plasma parameters, measuring a decrease in the ratio of atomic to molecular hydrogen ratio as well as a increase in the vibrational temperature of the molecules. Both of these changes in discharge conditions favours the production of negative ions through dissociative attachment of hydrogen molecules in the plasma volume.

The purpose of this experiment is to test the effectiveness of BDD to enhance the negative ion production in the pulsed plasma environment of a time modulated ICP discharge. BDD samples measuring $1cm^2$ in area and 0.6mm thick were placed around the extraction apertures of the ion source. The surface production of negative ions involves the backscattering of neutral particles from the surface, which through an interaction with their image charge in the surface acquire an electron in the affinity state and propagate away from the surface as a negative ion. This process is dominated by the flux of neutral particles onto the surface due to their significantly larger density. The mean free path of negative ions at these pressures is short as mutual neutralisation and collisional detachment with neutrals has a large rate coefficient, and will be the dominant loss mechanisms for negative ions at later times in the afterglow after the electron temperature has

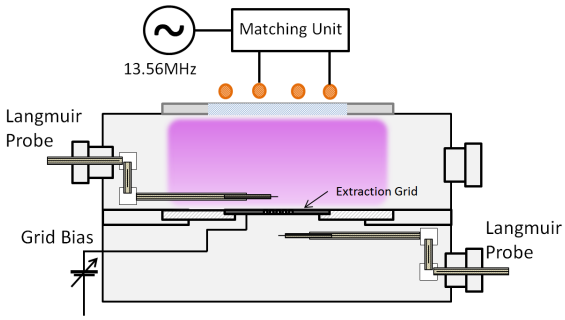


(a)

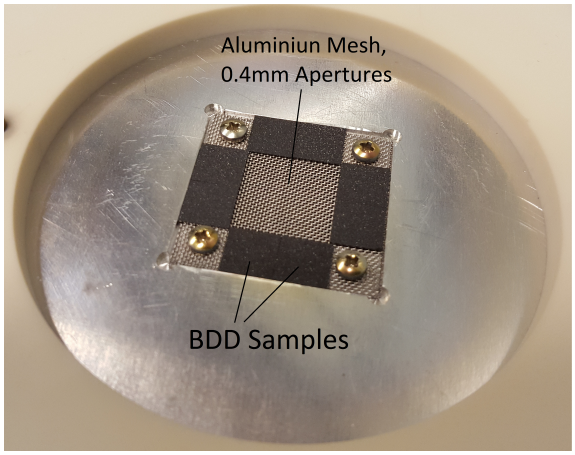


(b)

Figure 6.1: (a) the experimental set-up of the two turn planar coil ICP discharge, and (b) image of the extraction grid with BDD samples in place.

cooled. Any negative ions which are able to be extracted will have been generated close to the extraction area of the grid, either on the grid surface or above the grid through volume production. There have also been few *in situ* measurements of Cs alternatives in a plasma environment, as most results are measured from beam experiments, or mass spectrometers positioned very close to the surface which will affect the plasma surface interaction.

Figure 6.1 shows the experimental set-up of the planar coil time modulated ICP discharge and the the extraction grid with the apertures surrounded by the BDD samples. Measurements of the electron temperature $T_e$, plasma density n, and plasma potential $V_p$ were conducted with a Langmuir probe positioned approximately 2cm above the extraction apertures of the plasma grid. A second probe was positioned 1.5cm under the extraction region in order to provide an initial estimate of the ion and electron current extracted by the plasma grid, as well as the evolution of the ion and electron currents throughout the activeglow and afterglow.

## 6.2 Plasma Properties Above the Plasma Grid with BDD

Measurements of the discharge parameters were carried out above the extraction grid with BDD samples situated around the extraction apertures. The process of acquiring IV characteristics follows

the same procedure as outlined in section 5.2.1. Unless otherwise stated, the pulse frequency used in the following measurements was 2kHz with a pulse duty factor of 70%.

The electron temperature and plasma potential rapidly increase during the initial heating of the plasma due to the low electron population remaining at the end of the previous pulse [77], as discussed in section 2.5.2. After achieving their peak values they then decrease down until some equilibrium value is achieved. The plasma density increases more steadily compared to $T_e$ and $V_p$ until it achieves an equilibrium value. When the change in the plasma parameters is small throughout the remainder of the pulse the plasma has achieved its quasi-equilibrium state, in which the plasma parameters reflect those found in a continuous wave discharge. In the afterglow, hot electrons are rapidly lost to the walls and the electron temperature quickly decays. The decay slows down at later stages in the afterglow as only cold electrons remain and loss mechanisms such as ionisation are no longer available.

Figure 6.2 shows the effect of changing input power on $T_e$, $n$, and $V_p$. $T_e$ and $V_p$ are largely de-coupled to the input power and should remain unaffected by increasing the RF power. In this case the quasi-steadystate values of $T_e$ and $V_p$ are 2eV and 9V respectively, which remain constant at larger power. The plasma density is much more strongly related to the power deposited into the plasma, and as a result the density can be seen to increase from $1.8\times10^{16}\mathrm{m}^{-3}$ at 490W to $2.5\times10^{16}\mathrm{m}^{-3}$ at 680W. 490W was the lower limit of the power scan as at 5.0Pa it proved difficult to maintain an inductive H mode discharge at powers below this threshold.

Probe measurements follow the expected trends for increasing pressure, as shown in figure 6.3. Decreasing mean free path of electrons as gas pressure is increased reduced their average energy, leading to a decrease in the measured electron temperature and plasma potential. From 4-7Pa the quasi-stable value of $T_e$ decreased from 2.2eV to 1.6eV, whilst quasi-equilibrium values of $V_p$ fell from 9.8V to 8V. Plasma density increases due to the larger number density of neutrals available for ionisation, from $1.9\times10^{16}\mathrm{m}^{-3}$ to $2.5\times10^{16}\mathrm{m}^{-3}$ at 200$\mu$s into the activeglow of the pulse.

Figure 6.4 shows $T_e$, n, and $V_p$ in the extraction region with changing modulation frequency. For the frequency range of 2-10kHz the changing modulation frequency has little effect on the plasma parameters during the quasi-stable phase of the activeglow with $T_e$, n, and $V_p$ maintaining constant values. fixed duty factor results in increased afterglow periods at lower frequencies which will lead

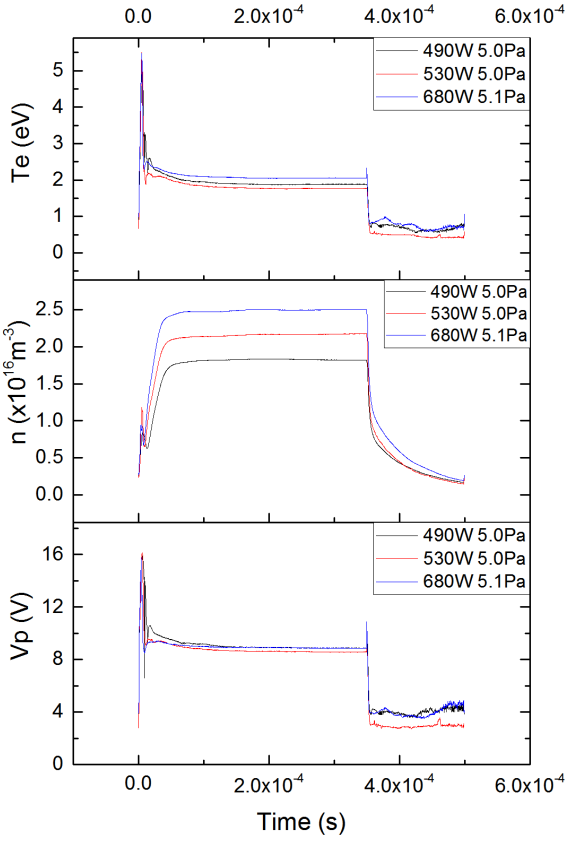


Figure 6.2: Effect of input power on plasma properties for a 2kHz 70% duty factor 5.0-5.1Pa plasma.

to reduced electron densities at the end of the afterglow period. This means the overshoot in the electron temperature and $V_p$ is more pronounced for lower pulse frequencies.

Similarly to measurements made with changing modulation frequency, altering the pulse duty factor has little effect on the equilibrium values of $T_e$ and $V_p$ most likely due to the time scale of the activeglow is still long enough to reliably achieve quasi-equilibrium. As shown in figure 6.5, $T_e$ and $V_p$ vary from 1.77-1.99eV and 8.6-9.3V respectively at 200$\mu$s into the activeglow, in the range of 50-90% duty factor. Similarly to the changing frequency measurements lower duty factors result in extended afterglow periods and a reduced electron density at the end of the pulse which result in a more pronounced spike in $T_e$ and $V_p$ during the initial heating of the plasma. Density measurements all follow the same trends but there is a discrepancy as the 70% duty factor measurements

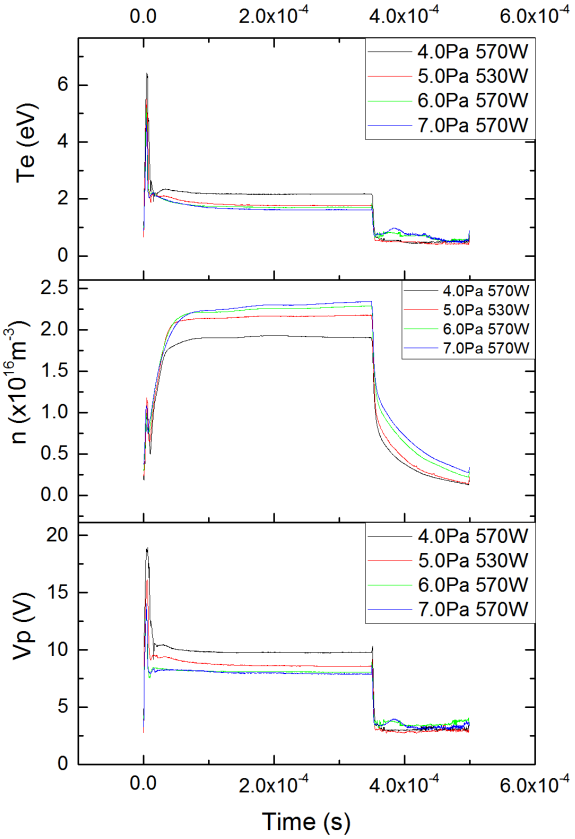


Figure 6.3: Effect of pressure on plasma properties for a 2kHz 70% duty factor 530-570W plasma.

record larger densities during the activeglow. The disagreement/discrepancy between the maximum density measured during the pulse is most likely due to a change in the power transfer efficiency due cleaning after a previous experiment.

Evolution of parameters during the afterglow remains consistent between discharge conditions: $T_e$ and $V_p$ rapidly decay as higher energy electrons are quickly lost to the walls. After around 10$\mu$s the decay slows as the remaining lower energy population can no longer collide inelastically with neutrals and are lost through diffusion to the walls. Density decreases more slowly as ions and low energy electrons recombine and propagate to the walls. Again this process is slowed by the decay of the plasma potential and loss of the high energy electron population.

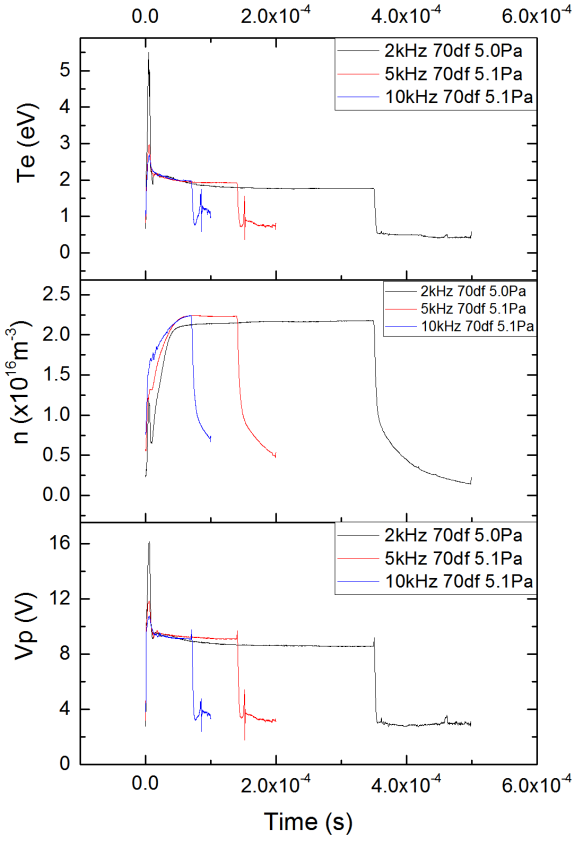


Figure 6.4: Plasma property evolution with changing pulse frequency in a 70% duty factor 5.0-5.1Pa 570W discharge.

### 6.2.1 Comparison to Measurements Without BDD

The results discussed in the previous section were compared to probe measurements taken in the extraction region without the BDD samples present around the plasma grid apertures. The IV characteristics were measured in the extraction region 2cm above the grid with a 2kHz 70% duty factor discharge operated at 4.9Pa with 530W of RF power. Figures 6.6a and 6.6b display the results of electron temperature and density measurements together with plasma properties observed whilst using BDD for almost identical discharge conditions.

plasma properties follow the same trends throughout the modulation cycle as those discussed in the previous section. Quasi-steadystate values of $V_p$ and $T_e$ were measured to be 8.6V and 1.9eV

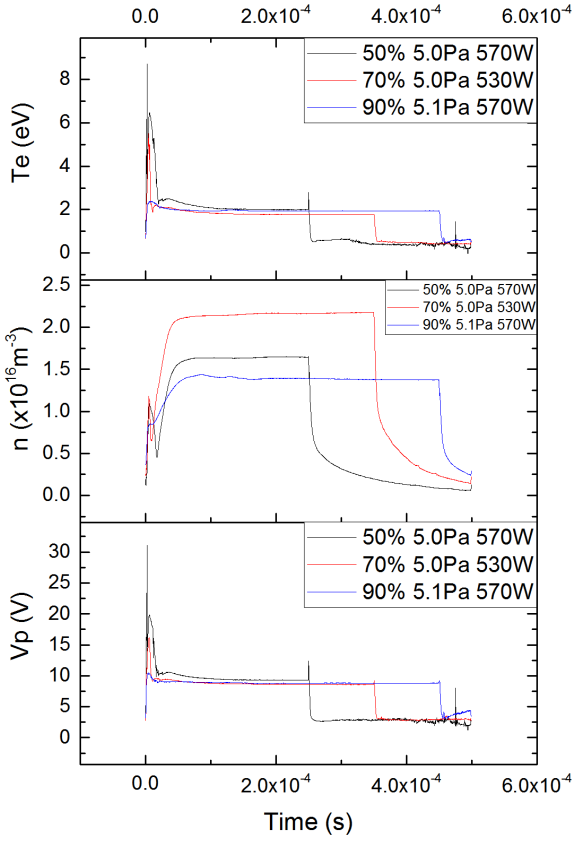


Figure 6.5: Effect of changing duty factor on plasma parameters in a 2kHz 530-570W 5.0-5.1Pa discharge

respectively, which match closely to that observed with BDD samples present in the discharge for similar gas pressures and RF power. The density is slightly lower at $1.8\times10^{16}\mathrm{m}^{-3}$, but still has a reasonable agreement and within 20% of the density measured with BDD.

The peak of the negative ion density is expected to be during the afterglow of the discharge when the dissociative attachment rate is enhanced by the reduced electron temperature. The afterglow of the discharge also exhibits the same characteristics as measured previously, with $T_e$ and $V_p$ rapidly decreasing during the initial stages of the afterglow before the decays slows in $<10\mu$s as diffusion losses to the walls begins to dominate. Figures 6.7a and 6.7b show the decay of the plasma density and potential in the afterglow with and without the use of BDD around the extraction grid. There is little difference in the decay of plasma properties throughout the afterglow, and implies that there

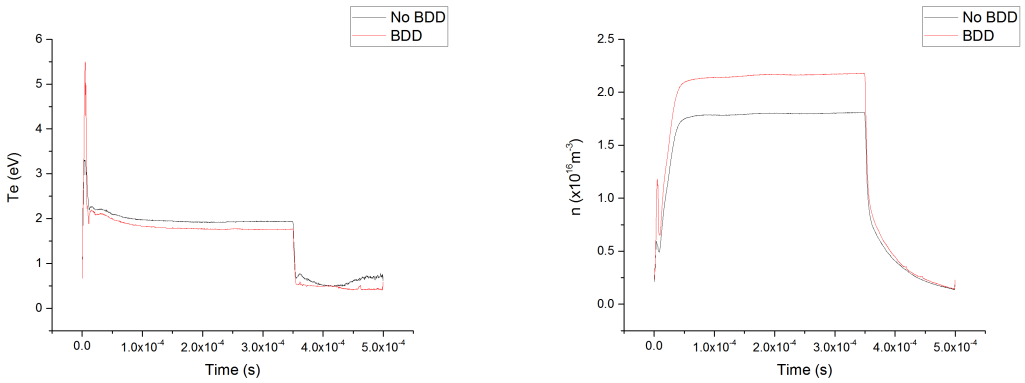


(a) (b)

Figure 6.6: Comparison of the evolution of $T_e$ (a) and $n$ (b) in the extraction region of two 2kHz 70% duty factor 5.0Pa 530W discharges, one with BDD and one without.

is almost no difference between the extraction regions of the two discharges which is resolvable with the accuracy of these Langmuir probe measurements. This demonstrates that the presence of the BDD samples have little effect on the plasma properties in the vicinity of the extraction grid.

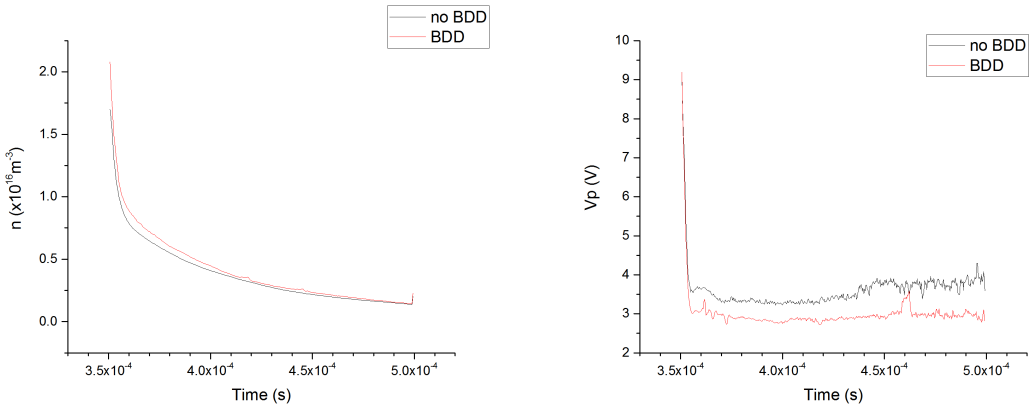


(a) (b)

Figure 6.7: Comparison of the evolution of plasma density (a) and $V_p$ (b) in the extraction region during afterglow of two 2kHz 70% duty factor 5.0Pa 530W discharges, one with BDD and one without.

### 6.2.2 Plasma Property Measurements with DC Bias Applied to the Extraction Grid

The sheath through which the charged species have to propagate on their trajectory through the extraction grid also is crucial in determining the energy distribution of the particles. As a result the use of the correct grid bias allows control of the final velocity/energy distribution of particles as they leave the plasma. Probe measurements were conducted with a continuous DC bias applied to the extraction grid in order to gain an understanding of the response of the plasma properties in the extraction region with a BDD covered plasma grid.

The potential difference between the BDD sample and plasma is an important parameter for surface produced negative ions. If the potential difference is small, then ions arrive at the sample surface with less energy and the resulting negative ions also have less energy with which to overcome the electric field and propagate back into the plasma. However if the current of negative ions leaving the surface is too large it can result in the formation of a virtual cathode which limits the negative ion current away from the surface. [101] also observed an increase in negative ion yield at larger ion bombardment energies of the surface.

Figure 6.8 shows the effect of applying a DC bias to the extraction grid on measured plasma properties for a 2kHz 70% duty factor modulated discharge, operated at 5.0Pa with an RF power of 530W. The grid bias modifies the plasma in a similar way to that observed in the previous chapter: The bias has little effect on the electron temperature, and the plasma potential increases in response to a positive bias. Negative grid bias has little effect on $V_p$, most likely due to the ion current drawn by the grid being small with respect to the electron current incident on the walls of the chamber resulting in a weak coupling between the plasma and the extraction grid bias. Density measurements with a floating extraction grid are not shown in figure 6.8 as they were anomalously large.

During the afterglow the plasma potential appears to shift to a value close to $V_p + V_g$, where $V_g$ is the grid bias, to in order to maintain a constant small potential difference between the grid and the discharge. This is likely due to expanding sheaths and less collisional processes available to the remaining population of low energy electrons. Collisional processes reduce the current drawn by

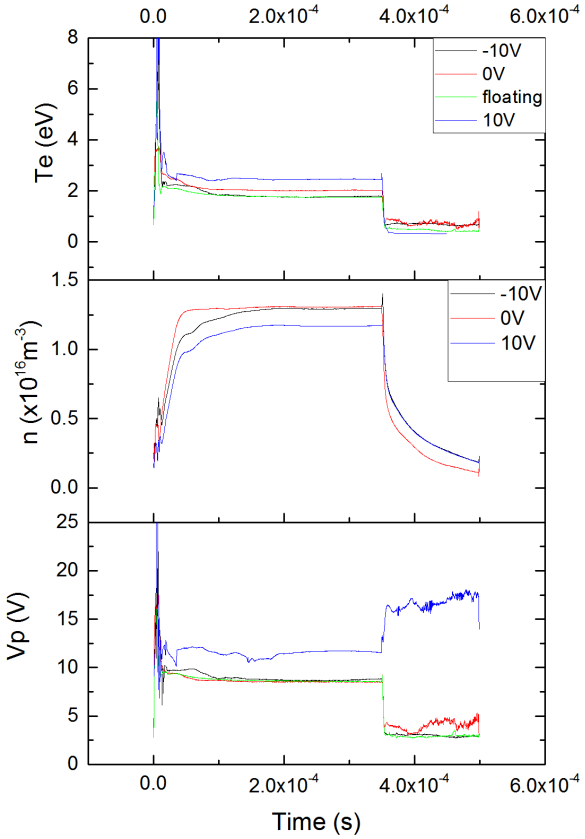


Figure 6.8: Evolution of $T_e$, $n$, and $V_p$ throughout a single pulse of a 2kHz 70% duty factor 5.0Pa 530W discharge. Different colour curves represent different DC biases applied to the extraction grid.

the sheath compared to ideal collisionless situations, and an expanding sheath surface area could result in the bias providing a greater perturbation to the plasma and an increased coupling between the discharge remaining in the afterglow and the extraction grid.

## 6.3 IV Characteristics of Extracted Beam

In addition to probe measurements conducted above the plasma grid, IV characteristics were measured under the extraction apertures to observe how electron and ion currents evolve during a pulse cycle, and their response to changing applied grid bias. Initially the intention was to implement

the RFA beneath the plasma grid in order to measure the IVDF of extracted ion beams, however the signal was too small to be able to extract any useful information. A second Langmuir probe was positioned approximately 1cm below the extraction grid with a 9mm long, 0.25mm diameter tungsten wire tip. The tip for this probe was made slightly longer in order to maximise the current drawn in the intrinsically lower charged particle density below the grid. The measurements were repeated using the same set of discharge conditions and grid biases with BDD surrounding the plasma grid. Whilst the use of a Langmuir probe was a back-up to RFA measurements and was not the ideal scenario, it was capable of providing useful information.

Measured currents under the grid were much smaller than in the bulk plasma leading to a reduced signal to noise ratio and larger uncertainty in the recorded IV characteristics, especially in the activeglow phase during which the current has an added RF component. The pressure in the chamber below the extraction grid was typically around 50-60% of that recorded in the upper chamber, resulting in larger mean free paths for collisions with neutrals.

The main focus of these measurements was the behaviour of the plasma during the afterglow of the pulse cycle, as the decreased electron temperature reduces negative ions losses through collisional detachment and the drop in plasma potential allows the propagation of volume produced negative ions out of the central core region of the plasma. Reduced electron temperatures also lead to increased volume production of ions due to a larger dissociative attachment cross section and result in enhanced negative ion densities during the afterglow. These processes plus any contribution from surface production should result in the peak negative ion density occurring sometime during the afterglow of the pulse.

Figure 6.9 shows the measured IV characteristics with different applied DC biases at 100$\mu$s into the afterglow, both with and without the use of BDD. Typical values obtained from OML density calculations were 0.3-1 $\times 10^{15}\mathrm{m}^{-3}$, around an order of magnitude difference with respect to the densities measured in the extraction region during the afterglow. These densities are only estimates as OML assumes an isotropic discharge and the flow of charges from the extraction grid apertures will result in some directionality to the current drawn by the probe tip, and the low density/ionisation fraction leads to greater uncertainty in the current measurement. Saturation currents and densities estimated are consistent between IVs with and without BDD surrounding the extraction grid. If the

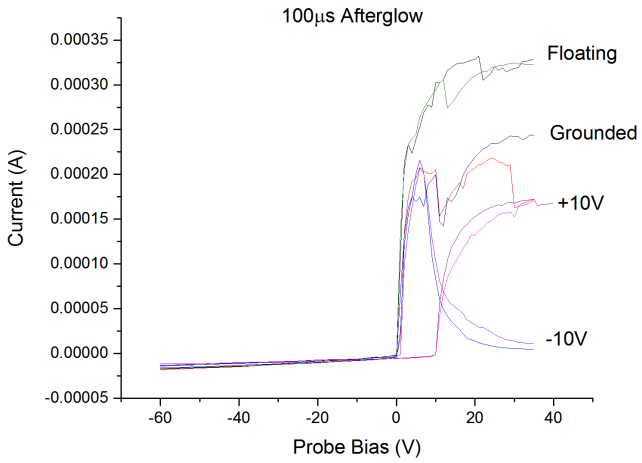


Figure 6.9: IV characteristics both with and without BDD below the extraction grid with various grid biases applied. Measurements were taken 100$\mu$s into the afterglow of a 2kHz 50% duty factor 5.0Pa discharge at 610W.

densities of $H^-$ were already small in the extraction region, then it will be challenging to confidently isolate a feature of the IVs indicating the presence of negative ions in the lower chamber where the densities are significantly smaller.

When applying a negative bias to the extraction gird the IV characteristics exhibit a peak in the electron current before the collected electron current begins to *decrease* as shown in figure 6.10. It is unclear what the driving mechanism behind this unusual behaviour of the IV curve is, but one plausible explanation is when the probe bias is small the flux of particles moving towards the probe is more isotropic in nature. However when the potential difference between the grid and the probe tip becomes large the probe collects a current from a much more collimated beam of charge particles resulting in a much smaller collection radius of the biased probe tip, decreasing the saturation current measured as the probe bias becomes increasingly positive.

## 6.4 IVDF Measurements with BDD

In situations where the negative ion density in the discharge is significant and they begin to become the dominant negative charge carrier in the plasma, the ambipolar electric field begins to weaken

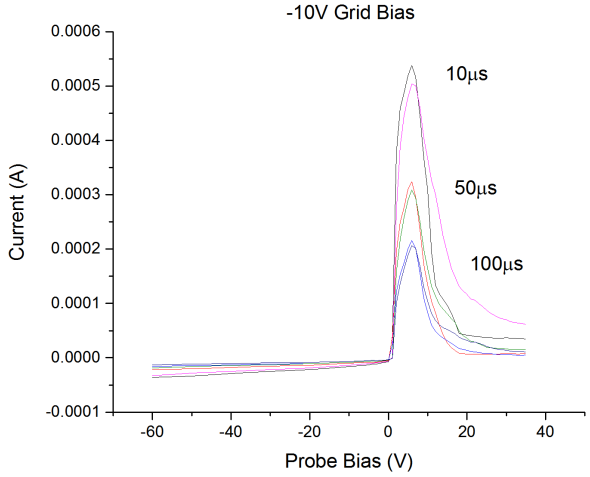


Figure 6.10: IV characteristics at various times during the afterglow with -10V DC bias applied to the extraction grid. Each line for each time step represents the IV curve with and without BDD.

as the mobilities of the positive and negative species are much more closely matched. In the case of identical mobility the electric field can vanish all together and charged species can diffuse freely in the plasma bulk. This process can alter the velocity distribution of the ions as the formation of the sheath and the Bohm criterion changes into a more complicated situation compared to the conventional ion-electron plasma. Even if the negative ions are still confined to the core, the transition from an ion-ion region in the core to an electron-ion region near the walls will affect the formation of the sheath and the IVDF of the plasma bulk. Although the negative ion density in the plasma bulk is likely to be small, even during the afterglow when the density is expected to be at its peak, their presence in the plasma should still have a measurable effect on sheath formation.

An RFA was positioned close to the extraction apertures and the BDD samples around them in order to measure the effect of the BDD on the IVDFs in the extraction region of the system. As surface produced negative ions have to traverse the potential barrier across the sheath in order to leave the surface, the potential difference between the discharge and the plasma grid is important for the optimisation of surface negative ion production. With this in mind measurements were made with various DC biases applied to the extraction grid with and without the apertures surrounded by the BDD samples. All of the following IVDFs were measured with a modulation frequency of 2kHz with a 50% duty factor, at a gas pressure of 4Pa and RF power of around 670W. The repulsion

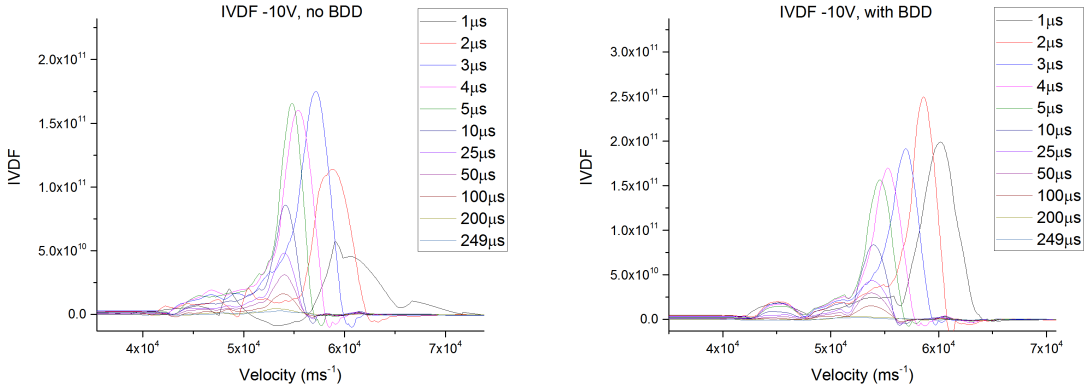


(a) (b)

Figure 6.11: IVDFs measured in the extraction region of a 2kHz 50% duty factor discharge operated at 670W and a gas pressure of 4.0Pa, with a -10V DC bias applied to the extraction grid. Figure (a) is without the use of BDD, and (b) with BDD present on the extraction grid.

electrode in the RFA was set to -30V in order to remove the electron component of the particle flux, whilst the collection electrode was swept from -30V to 30V to slowly filter out ions incapable of traversing the potential barrier between the repulsion grid and collector surface. Similarly to the previous section the afterglow of the pulse was the focus of these measurements as the peak of the negative ion density is expected to appear during this period of the modulation cycle.

It should be noted that whilst positioning the RFA close to the extraction region allows measurements of the IVDFs in proximity to the grid, the casing and stem of the RFA are grounded surfaces which will inevitably perturb the plasma in this area. Increased particles losses to the grounded surfaces will lead to some changes in the plasma properties observed in this region compared to that measured using the Langmuir probes.

The IVDFs in the afterglow follow the same basic pattern: the width of the peak narrows as the higher energy electron population is lost and ambipolar diffusion slows, whilst the velocity the peak is centred around decreases as the plasma potential decays and the voltage drop across the sheath positioned in front of the entrance of the RFA diminishes. When a positive DC bias is applied to the extraction grid the position of the peak shifts to reflect the increase or decrease of $V_p$ as it shifts to maintain a constant positive potential difference between the plasma and the extraction grid, as discussed in the biased probe measurements of the previous chapter. Typically IVDFs/IEDFs in

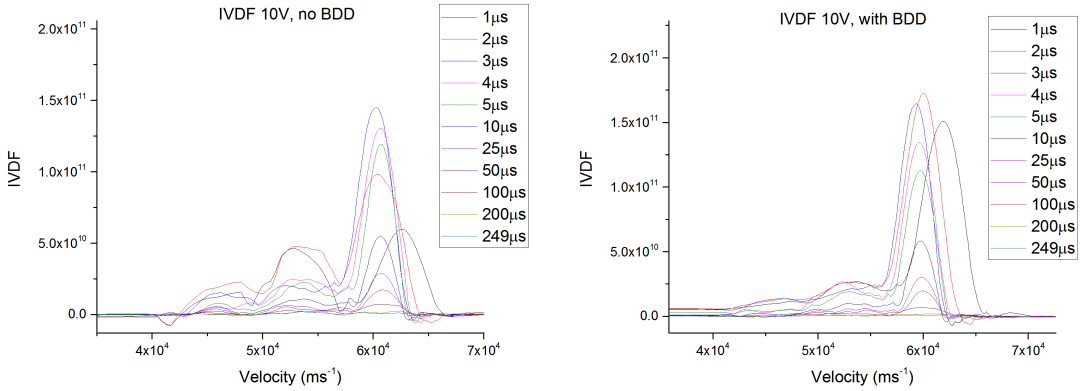


(a) (b)

Figure 6.12: IVDFs measured in the extraction region of a 2kHz 50% duty factor discharge operated at 670W and a gas pressure of 4.0Pa, without BDD (a) and with BDD (b). A 10V DC bias was applied to the extraction grid for these IVDFs.

ICP discharges will have a saddle-like bi-modal distribution corresponding to the two extrema of the RF oscillation on top of the sheath potential. However in this case there is only a single well defined peak in the distribution. This is likely due to the timescale over which ions in the plasma cross the sheath into the RFA being much longer than the period of RF oscillation for 13.56MHz. In this situation ions only experience a time averaged sheath potential as they propagate into the RFA, resulting in a single peak in the IVDF. As discussed in the previous chapter, the estimated time taken for the ions to traverse the sheath is roughly 10 times the RF period of oscillation when assuming a collisionless sheath, and as a result the IVDF will not have the typical bi-modal structure. The IVDF is also proportional to the mass of the ions, which in hydrogen will include contributions from $H^+$, $H_2^+$, and $H_3^+$.

Both sets of data contain some noise at lower velocities which is due to a combination of noise from the current measurements and ions which have lost energy collisionally being drawn into the RFA. Collisions and inelastic processes inside the RFA between the grounded grid at the entrance and the collection electrode, around 3mm. For the pressure at which these measurements were made (4Pa) the estimated mean free path for charge exchange of ions is on the order of a few centimetres which implies that there should be very little collisional processes occurring within the ion's trajectory between the entrance of the RFA and the collection electrode.

The data without the use of BDD produces noisier IVDFs during the first two microseconds of the afterglow. After 3$\mu$s into the afterglow of the pulse there is little difference in the IV characteristics measured by the RFA between experiments with BDD and those without. IVs for the first two microseconds of the afterglow consistently draw less ion current and are noisier than their counterparts involving the use of BDD. The density of the discharge can be calculated by integrating the IVDF over all velocities, and allows insight into the decay of the plasma during the afterglow. The density values calculated are an order of magnitude smaller than that measured from OML calculations of the Langmuir probe ion region, most likely due to the perturbation of the plasma caused by the grounded RFA stem and casing being positioned in the plasma bulk. Despite this the IVDF density calculation still allows for some insight into the evolution of the plasma density in the afterglow and a comparison between the density decay with and without the BDD samples on the extraction grid.

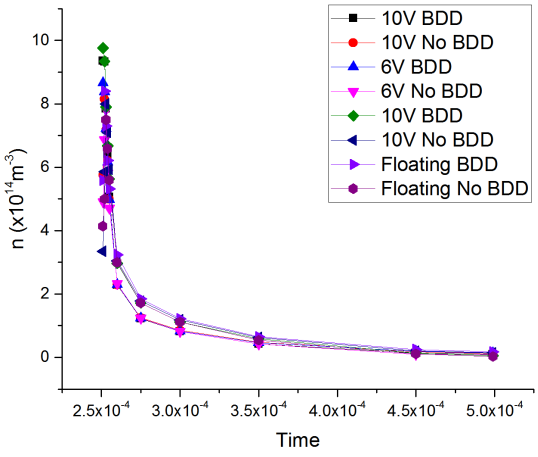


Figure 6.13: Decay of the density in the afterglow, calculated from the IVDFs both with and without the presence of BDD on the extraction grid.

Figure 6.13 shows the evolution of the plasma density calculated from the IVDFs measured with the extraction grid floating and with a continuous DC bias of -10V,6V, and 10V respectively. There is little observable difference between the density values calculated throughout the afterglow, appearing to be independent of the DC bias applied to the grid and the use of BDD in the extraction region of the plasma.

## 6.5 Discussion

The results presented have shown that the BDD has had no measurable effect on the plasma properties in the extraction region of the discharge. however this is likely due to the diagnostics implemented not having a high enough sensitivity to identify features which indicate the presence or increasing density of negative ions. With good enough sensitivity the diagnostics used should detect an increasing negative ion presence or estimate the concentration of negative ions in the plasma.

If the density of negative ions is large enough, the IV characteristics will become symmetric about the floating potential as the negative ions become the dominant negative charge carrier at later stages in the afterglow. For the time modulated filament discharge investigated by [64], the negative ion peak in the afterglow due to the enhancement of dissociative attachment of $H_2$ molecules takes around $90\mu$s to appear . In the case of these measurements no such transition was observed in the IV characteristics which implies that either the negative ion production rate/density is too low for $H^-$ to become the dominant negative charge around the grid probe, or that losses of $H^-$ are significant over the distance between the probe and the ion's point of production on the BDD surface. Based on the pressure range in which these probe measurements were conducted the cross section for $H^-$ mutual neutralisation with $H^+$ is large at $\approx 10^{-17}m^2$ [150, 151], but due to the low $H^+$ densities still results in a large mean free path, which again suggests that the concentration of negative ions in the discharge was too small.

Amemiya suggests that it is possible to determine the density of negative ions in a discharge with a low negative ion to electron ratio using Langmuir probes by using the second derivative of the IV characteristics [152, 153]. If $T_- \ll T_e$, where $T_-$ is the negative ion temperature, then a secondary peak can appear in the second derivative of the probe characteristics close to the plasma potential as the negative ion current increases rapidly with probe bias just below the plasma potential as the negative ions are quickly repelled once the probe bias starts to become negative with respect to $V_p$ [154]. However second derivatives of the IV characteristics measured in this experiment are too noisy to be able to resolve details such as the peak due to the negative ion current drawn by the probe, even after applying smoothing to the data. The concentration of negative ions in the plasma

can also be estimated by the ratio of electron and ion saturation currents in IV characteristics [155], however the difference between saturation currents with and without the use of BDD is small, and the presence of noise means that it is not possible to reliable determine any difference between the two for a concentration calculation.

As the peak of the negative ion density rises during the afterglow, if the density is large enough one would expect to see an effect on the ion velocity distribution due to the changing sheath formation physics and Bohm criterion. Zhang *et. al.* found that the sheath voltage decreased for increasing negative ion concentrations of up to 20% [156]. In some cases it is possible to treat the plasma as if it has two electron populations corresponding to a high temperature population representing the electrons and the negative ion cold population. Negative ions can be "captured" by the flow of positive ions where they are able to reach the sheath but are repelled by the sheath potential drop, leading to the formation of a double layer in the discharge [157]. The separation of the plasma into a negative ion populated electronegative region and electron-ion region near the walls can affect the IVDFs and sheath formation. Franklin also suggests that the separation of the plasma in this way leads to a potential structure that cannot be described by a simple double layer [158].

Measurements show that the central position of the peak in the IVDF is unaffected by the presence of the BDD on the extraction grid implying the potential drop across the sheath in front of the RFA through which the ions have to propagate is also unaffected by the BDD samples, at least to within the uncertainty of these measurements. Densities calculated from the IVDFs also demonstrate that there is little difference between measurements taken with and without BDD at all DC biases applied to the grid.

Studies have shown that the temperature of the Cs free alternative has an affect on the negative ion yield from that surface [101]. Some carbon types out-perform other allotropes at low temperatures, yet have the worst negative ion yield at elevated temperatures. According to these experiments BDD has the highest production of negative ions when heated to around $400^{o}$C. For the previous probe measurements the extraction grid was not actively heated, however a flux of electrons and ions naturally arises during the activeglow which will providing some heating as the particles impart their kinetic energy onto the grid. Measurement of the grid temperature increase due to this particle flux provides an estimate as to whether the BDD is at its optimal temperature for the largest surface

production yields. Surface temperature may also affect the recombination rate of atoms on the surface and affect the density of rovibrationally excited molecules in the extraction region.

A thermocouple was attached to the grid surface in order to estimate the heating effect of the plasma on the extraction grid and the final temperature achieved by the grid during operation. The temperature change during operation of the discharge was recorded with various DC biases applied to the extraction grid. After 10 minutes of pulsed operation the extraction grid achieved a maximum temperature of around $110^oC$. Whilst this temperature increase will lead to larger $H^-$ yields, the optimal conditions for BDD is a surface temperature close to $400^oC$.

Time modulated discharges used in plasma etching systems will usually make use of gas which have a much higher electronegativity than that of hydrogen, such as gases containing chlorine or fluorine. Larger electronegativity and increased binding energy for electrons in the affinity state mean that typically chlorine and fluorine discharges can have large negative ion densities in the discharge, greater than 20% of the charged species [81]. Hydrogen's relatively low electronegativity results in a much lower volume produced negative ion densities in the plasma. As such it is difficult to measure their presence or effect on the plasma using the techniques outlined above within the diagnostic sensitivity available in this experiment. BDD may have provided a large enhancement to the negative ion density in the extraction region of the chamber either through enhancement to the surface production through the backscattering of neutrals or through increasing the population of rovibrationally excited molecules, but this improvement was still beneath the threshold measurable using Langmuir probes or through IVDFs.

## 6.6 Effect of Plasma on BDD Samples

One crucial aspect of the feasibility of caesium alternative materials is the affect of the plasma on the material surface. A useful advantage of Cs evaporation into the ion source is that the Cs layer is easy to replenish during operation. Cs atoms can be sputtered from the plasma grid, and atoms from the wall can be removed and redeposited on top of the Cs layer. Over time this will affect the workfunction of the surface and affect negative ion production rates from the plasma grid. However this can be readily corrected by evaporating more Cs into the chamber to replenish the Cs layer on

the plasma grid. In systems where the negative ions are accelerated to high energies, such as fusion NBI beamlines, the resulting back scattered positive ion beam can sputter Cs from the backplate of the ion source. These Cs atoms can propagate through the ion source and assist in replenishing the Cs layer on the plasma grid.

This is not the case for carbon based Cs alternatives. If the discharge rapidly erodes the carbon surface then production rates of negative ions will be adversely affected. However even in the case these carbon atoms are redeposited onto the surface it is unlikely that it will lead to the formation of the same carbon allotrope. Access to the interior of the ion source would be required in order to restore the plasma grid surface. If this occurs regularly then it would not be feasible for use inside a fusion reactor due to the resulting increased reactor downtime. The surface must have a low erosion rate in order to be suitable for use in fusion NBI ion sources.

The surface of a BDD sample which had been present in the discharge chamber throughout the measurements conducted in sections 6.2 and 6.4 was compared with a sample which had not been exposed to the hydrogen plasma using SEM imaging. The samples were in contact with a hydrogen plasma with the set of varying discharge parameters as detailed in section 6.2 and 6.4. The total exposure time is on the order of 2 hours, with time in between each experiment in which some annealing processes could have occurred.

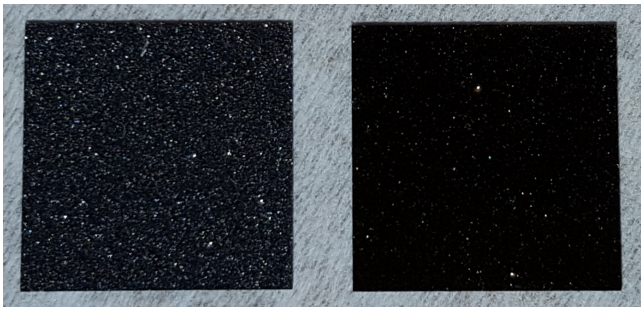

Figure 6.14: Image to show the visible difference between an untreated (left) and plasma treated (right) BDD sample.

Figure 6.14 shows the observable effect of the plasma with the naked eye. The amount of reflected light from the plasma treated surface has dramatically decreased. This could have been due to etching of the surface, deposition of other materials sputtered from the plasma grid/from the chamber walls, or an increase in the surface roughness.

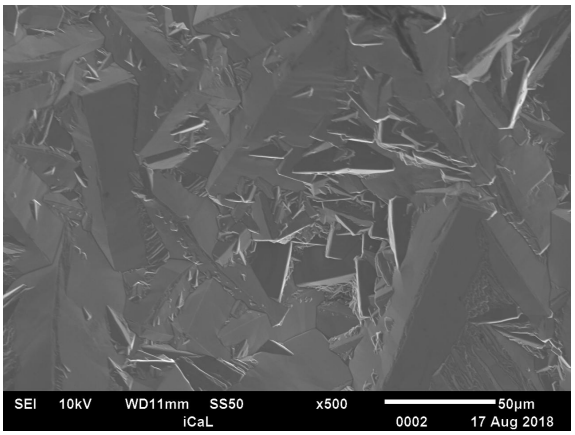


(a) Untreated BDD sample at 500 times magnification.

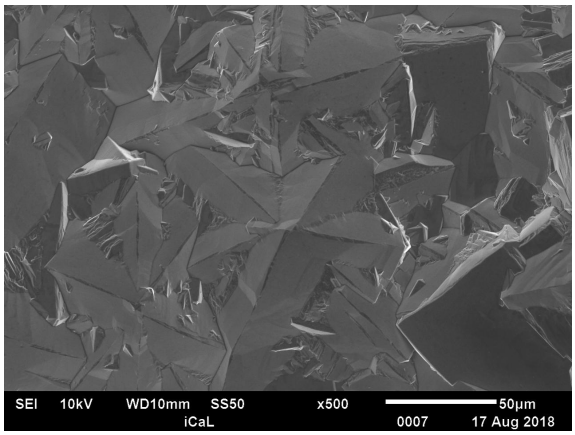


(b) After exposure to the plasma at 500 times magnification

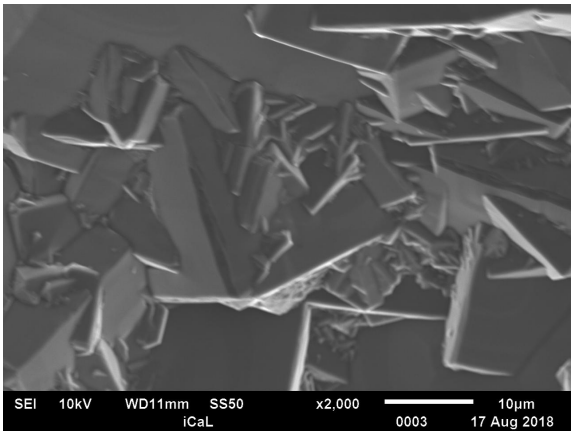


(c) Untreated BDD sample at 2000 times magnification.

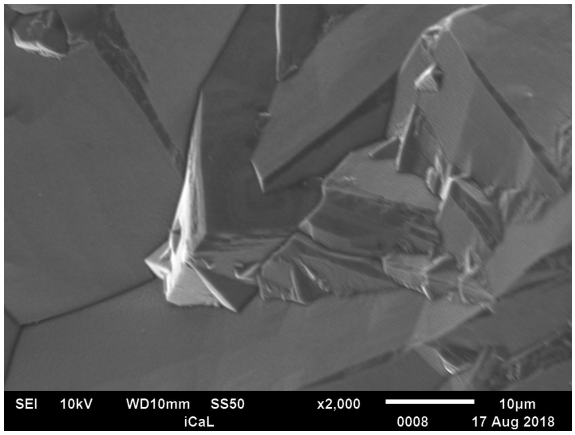


(d) After exposure to the plasma at 2000 times magnification

Figure 6.15

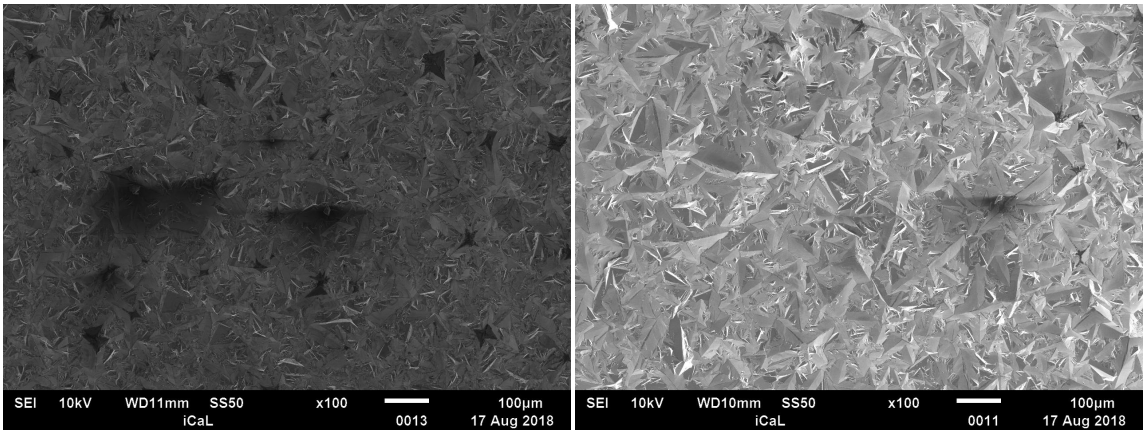


(a) Untreated BDD sample. (b) After exposure to the plasma

Figure 6.16

Figure 6.15 demonstrates that there is little difference between the surface structure of the two samples at several magnification levels. There are no obvious indications of the diamond surface having been coated in another material, and there is no discernible difference in the surface crystal structure between the two samples.

The unexposed sample had a large number of dark regions covering the surface which were not present in the BDD placed inside the ion source, as shown in figure 6.16 and in more detail in figure 6.17. Energy dispersive X ray diffraction element analysis indicated that these were not due to contamination as they were dominated by a carbon signal. These spots could be from the manufacturing or doping process, however in this case the machine is unable to resolve any signal from boron over the carbon as they are so similar in mass. The lack of their presence on the BDD exposed to the plasma suggests has removed these regions, or that the temperature increase caused by exposure to the plasma has affected the surface structure. One possible explanation is that the CVD production process usually favours the growth of graphite structures on the substrate, but graphite is easily removed from the surface by the plasma. If some deposition/growth processes can continue to occur on the surface after the CVD process has stopped, then this could manifest as the growth of graphite on top of the BDD structures. As there are far fewer of these impurities on the surface of the BDD sample placed in the plasma, it could suggest that these impurities were composed of a material easily removed by the plasma, such as graphite.

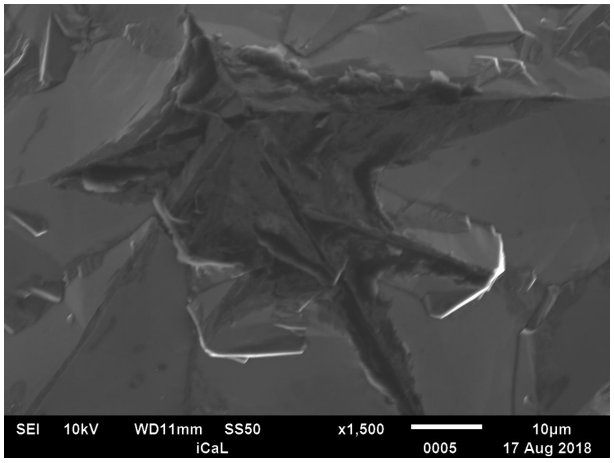


Figure 6.17: Impurity site on the untreated BDD sample.

In order to observe whether exposure to the plasma has had an effect on the surface roughness of the BDD, SEM images of the samples from the side were also taken as shown in figure 6.18. Again at several magnifications the surface feature sizes of the larger crystal structures remain consistent between the treated and untreated samples. However in figure 6.18 it appears as though the untreated sample has a larger number of smaller structures on its surface. If these have been removed by the plasma such that light is now reflected predominantly in one orientation, it could provide an explanation for the colour change of the treated BDD samples. The SEM images of the BDD samples have demonstrated that exposure to the pulsed $H_2$ has done little to modify the surface structure of the samples, after >2h total treatment time with an average discharge power in the range of 500-700W.

Kurutz *et. al.* [149] also reported relatively small erosion rates of $10^{-3}gh^{-1}$ for >10h of exposure time for BDD samples in a 300W ECR discharge operated at 0.3Pa, significantly lower pressures than this experiment. Whilst this erosion rate seems low, ion sources for commercial fusion reactor NBI systems will operate at much higher plasma densities which will result in an increased etch rate and will be required to operate for thousands of hours without replacement. The source used in [149] is a continuous wave source so naturally the etching rates will be higher compared to pulsed operation. The significantly lower source pressure will also result in higher electron temperatures and increased energies of ions incident on the surface. For this experiment there was no difference in mass between treated and untreated BDD samples outside of the manufacturing tolerance which

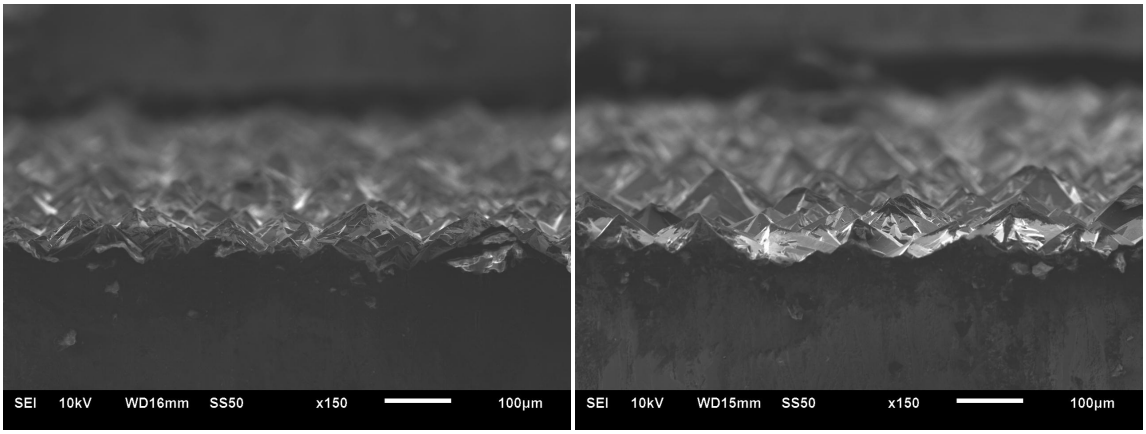


(a) Side view of an untreated BDD sample. (b) Side view of treated BDD sample.

Figure 6.18

implies that the erosion or deposition rate of BDD in the time modulated discharge is small, though a more dedicated investigation into this is required for more quantitative information.

These erosion rates are for ion sources operating with powers <1kW, typical ion sources used or planned for use in fusion NBI systems will utilise powers on the order of tens of kW. Significantly larger plasma densities will lead to much larger erosion rates and shorter lifetimes of BDD surfaces. With this in mind it appears unlikely that BDD based alternatives to Cs will be a viable option for use in negative ion sources for a commercial reactor when the source is operated in CW without reduction to the erosion rate or a mechanism for replenishing the diamond surface without significant reactor downtime

## 6.7 Conclusion

Fusion negative ion sources in DEMO and commercial reactors will have to dramatically increase the efficiency at which they use Cs or find alternative materials to enhance negative ion surface production in order to reduce reactor maintenance and be economically competitive. One of the promising candidates for Cs free enhancement of $H^-$ surface production is BDD. BDD has previously been tested for its ability to enhance the surface production of negative ions in continuous wave discharges. The purpose of this work was to evaluate the performance of BDD in a time modulated

plasma environment.

Langmuir probe and RFA measurements were conducted in the extraction region of a time modulated hydrogen ICP discharge with and without BDD samples surrounding the apertures of a biased extraction grid, in order to observe and changes in the plasma properties which may indicate an increased negative ion density. A second Langmuir probe was positioned beneath the extraction grid in order to measure IV characteristics of extracted particles.

Time evolution of plasma properties in the extraction region followed the expected trends. Power deposition into an initially small electron population leads to a peak in the electron temperature and plasma potential before decreasing down to quasi-steadystate values as the plasma achieves equilibrium. The density of the discharge increases smoothly to the its equilibrium value. In the afterglow $T_e$ and $V_p$ rapidly decay as high temperature electrons are lost to the walls and slows after around $10\mu$s as inelastic processes stop and diffusion to walls dominates. Density decays more slowly as cold electrons and ions diffuse to the walls and recombine.

No significant difference was found in the extraction region plasma properties between discharges with the BDD samples present and those without. Ultimately this meant that effect of the BDD samples on the extraction region of the could not be determined through probe and RFA diagnostics likely due to negative ion densities in the region being too small for the measurement techniques to be able to identify confidently outside of the uncertainty in those measurements. This does not mean that BDD has no effect on the production rate of negative ions or the maximum negative ion density in the discharge, either due to surface production through backscattering of neutrals or by increasing the density of rovibrationally excited molecules available for dissociative attachment. More accurate probe diagnostics capable of producing second derivatives not dominated by noise or a diagnostic dedicated to directly measuring the negative ion density is required in order to investigate further.

Finally the BDD samples were placed in an SEM microscope to determine if exposure to the hydrogen discharge had resulted in any significant changes in surface morphology or sample mass through chemical etching, sputtering of carbon, or deposition of materials such as silicon from the quartz window beneath the coil.

# Chapter 7

# Conclusions & Future Work

## 7.1 Conclusion

Negative ion sources for NBI systems currently in development for the next step on the fusion roadmap, the ITER tokamak, are based on hydrogen or deuterium ICP discharges which make use of magnetic filtering in order to reduce the electron temperature close to the extraction system and minimise collisional detachment losses of $H^-/D^-$ ions. They also make use of Cs ovens to evaporate a layer of Cs onto the plasma grid, lowering its workfunction and enhancing surface production of negative ions. However the predicted consumption rate and build up of Cs in beamline components will not be tolerable in commercial reactors beyond ITER. Cs must be consumed more efficiently or alternative materials must be found.

Time modulated plasma sources developed for damage free etching of semiconductor devices have demonstrated reduced electron temperatures in the afterglow of the pulse, as a result the collisional loss rate of negative ions is small. However most of this work has been conducted primarily in highly electronegative gases such as chlorine. There has been comparatively little work on temporally filtered hydrogen ion sources, where the reduced collisional loss rates and enhanced volume production of $H^-$ in the afterglow may prove useful for NBI ion sources.

Some potential Cs alternative materials candidates have been identified in allotropes of carbon, such

as BDD and HOPG. Some testing of these materials has taken place in continuous wave plasma environments with little or no filtering of higher temperature electrons in the discharge. Currently no work has been carried out to investigate Cs alternative material performance in a pulse plasma environment.

The aim of this work was to develop and characterise a time modulated hydrogen ion source based on a time modulated ICP discharge. The characterisation process involved a combination Langmuir probe and retarding field energy analyser diagnostics, carried out in both argon and hydrogen discharges. A Cs alternative material candidate, BDD, has also been tested in the pulsed hydrogen plasma environment in order to measure the effect of its presence on plasma properties in the extraction region of the chamber.

In chapter 4 a time modulated argon discharge was characterised. The evolution of plasma properties throughout the modulation cycle agreed with that expected for an electropositive gas such as argon. Langmuir probe measurements in the centre of the discharge showed that the initial heating of a small population of electrons at the start of the pulse cycle results in a small peak or overshoot of the electron temperature and plasma potential. As the plasma transitions into its quasi-steadystate period of the pulse, $T_e$ and $V_p$ decrease to values representative of those found in a continuous wave discharge. The density slowly climbs to its quasi-steadysate value. During the afterglow $T_e$ and $V_p$ rapidly decayed, with $T_e$ falling to below 0.5eV in around 50$\mu$s, whilst density decreased more slowly as ions and colder electrons diffused to the walls.

Larger RF power increases plasma density with little effect on $T_e$ or $V_p$. Increasing gas pressure reduces $T_e$ and $V_p$ due to increased collisionality whilst increases the measured charge carrier density. Lower pulse duty factor has little effect on the final quasi-steadystate values of $T_e$, $V_p$, and density but increases the overshoot $T_e$ and $V_p$ initial stages of the pulse, and the increase in the density of discharge at the start of the pulse is also shown to be affected by the extended afterglow period. Lastly $T_e$ and $V_p$ are largely unaffected by a change of pulse frequency (within the range of frequencies used in this experiment), whilst the maximum value of plasma density measured in the activeglow decreases at larger frequencies, most likely due to reduced amount of power deposited in the discharge during each pulse cycle.

The decay of the electron temperature agreed with analytical calculations based on the decay being

largely controlled by the loss of particles and kinetic energy through diffusion to the chamber walls, which implied that the primary loss mechanism in this discharge in the afterglow was through diffusion cooling.

Results presented in chapter 5 were from the characterisation of a time modulated hydrogen ICP discharge. Evolution of $T_e$, n, and $V_p$ during the pulse and the effect of changing discharge conditions on these properties was recorded in the centre of the discharge and in the extraction region. The time evolution was found to be similar to that of argon during the activeglow, however the molecular nature of hydrogen lead to decreased plasma densities and a larger overshoot in $T_e$ and $V_p$ during the early stages of the activeglow as increased number of inelastic collision channels available resulted in a smaller electron population at the beginning of each pulse. Plasma density measured in the extraction region was on the order of 30-40% of values observed in the centre of the discharge. $T_e$ and $V_p$ more rapidly decayed in the afterglow compared to argon, with electron temperatures falling to below 0.5eV in less than 10$\mu$s.

The time resolved measurements of plasma properties in a time modulated hydrogen ICP discharge has provided new insight into the effect of changing discharge/pulse parameters. The low effective electron temperatures in the afterglow will result in significantly reduced collisional losses of negative ions, and so the afterglow of the pulsed plasma is a suitable environment for the production and subsequent extraction of $H^-$ ions, and may be useful for fusion NBI purposes when the temporal electron cooling is used in combination with surface production of negative ions.

In chapter 6 samples off BDD, a potential Cs alternative material for enhanced surface production of negative ions, was placed around the apertures of the extraction grid. Time evolution measurements of plasma properties were performed in the extraction region above the plasma grid, and compared to measurements taken without the use of BDD. A second Langmuir probe was positioned beneath the extraction grid and IV characteristics of extracted particles were also measured with and without the presence of BDD on the extraction grid.

No significant difference was found in the extraction region plasma properties between discharges with the BDD samples present and those without. Ultimately this meant that effect of the BDD samples on the extraction region of the could not be determined through probe and RFA diagnostics likely due to intrinsic negative ion densities in the discharge being too small for the measurement

techniques implemented to be able to identify. However this does not suggest that BDD has no effect on the production rate of negative ions or the maximum negative ion density in the discharge, either through surface production by increasing the density of rovibrationally excited molecules. More accurate probe diagnostics capable of producing second derivatives not dominated by noise or a diagnostic dedicated to directly measuring the negative ion density is required in order to investigate further.

Whilst determination of the effects of BDD in the discharge were unsuccessful, this work was successful in developing and characterising a time modulated ICP discharge in both argon and hydrogen. A high plasma density was demonstrated in the activeglow, together with temporal filtering of the electron temperature in the afterglow. Whilst many modelling and experimental studies have been carried out in the area of pulsed argon ICP discharges, there has been comparatively less research conducted into time modulated hydrogen discharges. The work conducted in this project into the time evolution of plasma properties and their response to an extraction bias in the pulsed environment should form a useful contribution to the field.

## 7.2 Suggestions for Future Work

For future work, this experiment would benefit greatly from a diagnostic to directly measure the density of negative ions in the plasma, such as laser photodetachment measurements, cavity ring-down, or spectroscopic measurements in combination with an appropriate model. However these techniques can be expensive and would be difficult to implement to obtain $H^-$ density measurements in the extraction region of the discharge or in the lower region beneath the extraction grid after the ions have been extracted. Heat issues in the matching unit also need to be solved so that the discharge can be run consistently at higher powers.

Improvements in the accuracy of probe and RFA diagnostics through RF filtering or more careful construction to maximise signal to noise ratio would also be beneficial. More accurate probe measurements could allow for calculation of EEDFs in the discharge and determine the nature of the distribution which allows one to select the appropriate probe analysis techniques for the most accurate measurements of plasma properties. Increased accuracy of probe measurements may also

allow calculation of the negative ion concentration which is much easier to implement throughout the discharge chamber. These improvements combined with a heating mechanism to control the temperature of the samples on the extraction grid would allow for better testing of the effect Cs alternative material have on negative ion density over a larger parameter space. This experiment would also probably benefit greatly from a model of the discharge. A more detailed *in-situ* study on the etching of material samples and deposition of materials sputtered from surfaces inside the chamber over a range of discharge conditions would also be useful.

Previous works [106] have suggested that BDD doesn't provide an increase in the surface production of negative ions but actually increases the density of rovibrationally excited molecules through the surface recombination of atoms. A model along with optical emission spectroscopy of the vibrational bands of hydrogen to determine if the average vibrational temperature of the discharge is affected by the presence of BDD which could help answer whether any increase in negative ion density is due to surface or volume production. Repeating similar measurements for a deuterium discharge would also a strong insight into the potential of time modulated ICPs as fusion NBI ion sources.

# Bibliography


[1] Francis F. Chen. *Introduction to Plasma Physics and Controlled Fusion Second Edition.* 2006.

[2] M. Vleugels, G. Shama, X.T. Deng, E. Greenacre, T. Brocklehurst, and M.G. Kong. Atmospheric Plasma Inactivation of Biofilm-Forming Bacteria for Food Safety Control. *IEEE Transactions on Plasma Science 33 2*, 2005.

[3] Jrgen Schlegel, Julia Kritzer, and Veronika Boxhammer. Plasma in cancer treatment. *Clinical Plasma Medicine 1*, 2013.

[4] Danhua Mei, Xinbo Zhu, Ya-Ling He, Joseph D. Yan, and Xin Tu. Plasma-assisted conversion of CO2 in a dielectric barrier discharge reactor: understanding the effect of packing materials. *Plasma Sources Sci. Technol. 24 015011*, 2015.

[5] Erik C. Neyts, Kostya (Ken) Ostrikov, Mahendra K. Sunkara, and Annemie Bogaerts. Plasma Catalysis: Synergistic Effects at the Nanoscale. *Chem. Rev. 2015, 115, 1340813446*, 2015.

[6] Demetre J Economou. Pulsed plasma etching for semiconductor manufacturing. *J. Phys. D: Appl. Phys. 47*, 2014.

[7] K. Sarakinos, J. Alami, and S. Konstantinidis. High power pulsed magnetron sputtering: A review on scientific and engineering state of the art. *Surface and Coatings Technology 204 16611684*, 2010.

[8] EFDA. Fusion Electricity, A roadmap to the realisation of fusion energy. *European Fusion Development Agreement*, 2012.

[9] University of Wisconsin-Madison. Inertial Electrostatic Confinement Fusion, 2014.

[10] Stefano Atzeni and Jurgen Meyer-Ter-Vehn. *The Physics of Inertial Fusion: Beam Plasma Interaction, Hydrodynamics, and Hot Dense Matter.* 2004.

[11] John Wesson. *Tokamaks 4th Edition.* 2011.

[12] M. Krychowiak *et. al.* Overview of diagnostic performance and results for the first operation phase in Wendelstein 7-X (invited). *Rev. Sci. Instrum. 87, 11D304*, 2016.

[13] R. Aymar *et. al.* The ITER design. *Plasma Phys. Control. Fusion 44 519*, 2002.

[14] Norbert Rust, Bernd Heinemann, Boris Mendelevitch, Alan Peacock, and Michael Smirnow. W7-X neutral-beam-injection: Selection of the NBI source positions for experiment start-up. *Fusion Engineering and Design 86 728731*, 2011.

[15] W. Kraus. Ion Sources for Fusion. *Powerpoint presentation, CERN Accelerator School Ion Sources*, 2012.

[16] M. Hanada, A. Kojima, Y. Tanaka, T. Inoue, K. Watanabe, M. Taniguchi, M. Kashiwagi, H. Tobari, N. Umeda, N. Akino, M. Kazawa, K. Oasa, M. Komata, K. Usui, K. Mogaki, S. Sasaki, K. Kikuchi, S. Nemoto, K. Oshima, Y. Endo, T. Simizu, N. Kubo, M. Kawai, and L.R. Grisham. Progress in development and design of the neutral beam injector for JT-60SA. *Fusion Engineering and Design 86 835838*, 2011.

[17] Y. Oka, Y. Takeiri, K. Tsumori, M. Osakabe, O. Kaneko, K. Ikeda, M. Hamabe, E. Asano, T. Kawamoto, and L. Grisham. Performance of LHD-NBI H- ion source. *REVIEW OF SCIENTIFIC INSTRUMENTS VOLUME 73, NUMBER 2*, 2001.

[18] D Wunderlich, S Mochalskyy, U Fantz, P Franzen, and the NNBI-Team. Modelling the ion source for ITER NBI: from the generation of negative hydrogen ions to their extraction. *Plasma Sources Sci. Technol. 23 015008 (11pp)*, 2014.

[19] B. Heinemann, H.D. Falter, U. Fantz, P. Franzen, M. Froeschle, W. Kraus, C. Martens, R. Nocentini, R. Riedl, E. Speth, and A. Staebler. The negative ion source test facility ELISE. *Fusion Engineering and Design 86 768771*, 2011.

[20] P. Franzen U. Fantz, D. Wunderlich, B. Heinemann, R. Riedl, W. Kraus, M. Froschle, B. Ruf, R. Nocentini, and the NNBI Team. Progress of the ELISE test facility: results of caesium operation with low RF power. *Nucl. Fusion 55*, 2015.

[21] D. Marcuzzi, P. Agostinetti, M. Dalla Palma, F. Degli Agostini, M. Pavei, A. Rizzolo, M. Tollin, and L. Trevisan. Detail design of the beam source for the SPIDER experiment. *Fusion Engineering and Design 85 17921797*, 2010.

[22] P. Zaccaria, P. Agostinetti, D. Marcuzzi, M. Pavei, N. Pilan, A. Rizzolo, P. Sonato, F. Spada, and L. Trevisan. Progress in the MITICA beam source design. *Review of Scientific Instruments 83, 02B108; doi: 10.1063/1.3670335*, 2012.

[23] E. Speth, H.D. Falter, P. Franzen, U. Fantz, M. Bandyopadhyay, S. Christ, A. Encheva, M. Froschle, D. Holtum, B. Heinemann, W. Kraus, A. Lorenz, Ch. Martens, P. McNeely, S. Obermayer, R. Riedl, R. Suss, A. Tanga, R. Wilhelm, and D. Wunderlich. Overview of the RF source development programme at IPP Garching. *Nucl. Fusion 46 S220S238*, 2006.

[24] U. Fantz, P. Franzen, B. Heinemann, and D. Wunderlich. First results of the ITER-relevant negative ion beam test facility ELISE (invited)a). *Rev. Sci. Instrum. 85, 02B305*, 2014.

[25] P. Chabert and N. Braithwaite. *Physics of Radio-Frequency Plasmas*. 2011.

[26] I M El-Fayoumi, I R Jones, and M M Turner. Hysteresis in the E- to H-mode transition in a planar coil, inductively coupled RF argon discharge. *J. Phys. D: Appl. Phys. 31 (1998) 30823094*, 1998.

[27] M M Turner and M A Lieberman. Hysteresis and the E-to-H transition in radiofrequency inductive discharges. *Plasma Sources Sci. Technol. 8 (1999) 313324*, 1999.

[28] Min-Hyong Lee and Chin-Wook Chung. Observation of inverse hysteresis in the E to H mode transitions in inductively coupled plasmas. *Plasma Sources Sci. Technol. 19 015011*, 2010.

[29] J. C. Rienstra-Kiracofe *et. al.* Atomic and Molecular Electron Affinities: Photoelectron Experiments and Theoretical Computations. *Chem. Rev., 102, 231282*, 2002.

[30] Mainak Bandyopadhyay. Studies of an inductively coupled negative hydrogen ion radio frequency source through simulations and experiments. *PhD Thesis, Max-Planck-Institut fr Plasma physik, Garching, Germany*, 2004.

[31] J. N. Bardsley and J. M. Wadehra. Dissociative attachment and vibrational excitation in low-energy collisions of electrons with H2 and D2. *PHYSICAL REVIEW A VOLUME 20, NUMBER 4*, 1979.

[32] J. M. Wadehra. Rates of dissociative attachment of electrons to excited H2 and D2. *Applied Physics Letters 35, 917*, 1979.

[33] J. Horacek, M. Eizek, K. Houfek, and P. Kolorene. Dissociative electron attachment and vibrational excitation of H2 by low-energy electrons: Calculations based on an improved nonlocal resonance model. *PHYSICAL REVIEW A 70, 052712*, 2004.

[34] J. R. Hiskes, A. M. Karo, M. Bacal, A. M. Bruneteau, and W. G. Graham. Hydrogen vibrational population distributions and negative ion concentrations in a medium density hydrogen discharge. *Journal of Applied Physics 53, 3469 doi: 10.1063/1.331166*, 1982.

[35] M. Capitelli, R. Celiberto, F. Esposito, A. Laricchiuta, K. Hassouni, and S. Longo. Elementary processes and kinetics of H2 plasmas for different technological applications. *Plasma Sources Sci. Technol. 11 A7-A25*, 2002.

[36] M. Capitelli, M. Cacciatore, R. Celiberto, O. De Pascale, P. Diomede, F. Esposito, A. Gicquel, C. Gorse, K. Hassouni, A. Laricchiuta, S. Longo, D. Pagano, and M. Rutigliano. Vibrational kinetics, electron dynamics and elementary processes in H2 and D2 plasmas for negative ion production: modelling aspects. *Nucl. Fusion 46 S260S274*, 2006.

[37] Xianwei Sha, Bret Jackson, and Didier Lemoine. Quantum studies of EleyRideal reactions between H atoms on a graphite surface. *The Journal of Chemical Physics 116, 7158 doi: 10.1063/1.1463399*, 2002.

[38] Bret Jackson and Didier Lemoine. EleyRideal reactions between H atoms on metal and graphite surfaces: The variation of reactivity with substrate. *JOURNAL OF CHEMICAL PHYSICS VOLUME 114, NUMBER 1*, 2001.

[39] J. Amorim, J. Loureiro, and D. Schram. Formation of H- ions via vibrational excited molecules produced from recombinative wall desorption of H atoms in a low pressure H2 positive column. *Chemical Physics Letters 443-448*, 2001.

[40] Peter Vankan. Molecules and Atoms in a Hydrogen Plasma Expansion. *PhD thesis, Eindhoven University*, 2005.

[41] O. Gabriel, J. J. A. van den Dungen, D. C. Schram, and R. Engeln. Nonequilibrium rovibrational energy distributions of hydrogen isotopologues in an expanding plasma jet. *The Journal of Chemical Physics 132, 104305*, 2010.

[42] P. Vankan, D.C. Schram, and R. Engeln. High rotational excitation of molecular hydrogen in plasmas. *Chemical Physics Letters 400 196200*, 2004.

[43] C. T. Rettner, H. A. Michelsen, and D. J. Auerbach. Quantum-state-specific dynamics of the dissociative adsorption and associative desorption of H2 at a Cu(111) surface. *The Journal of Chemical Physics 102, 4625*, 1995.

[44] L. A. Pinnaduwage and L. G. Christophorou. Verification of H formation in ultravioletlaserirradiated hydrogen: Implications for negative ion and neutral beam technologies. *Journal of Applied Physics 76, 46; doi: 10.1063/1.358437*, 1994.

[45] J. R. Hiskes. Molecular Rydberg states in hydrogen negative ion discharges. *: Applied Physics Letters 69, 755; doi: 10.1063/1.117881*, 1996.

[46] L. A. Pinnaduwage, W. X. Ding, D. L. McCorkle, S. H. Lin, A. M. Mebel, and A. Garscadden. Enhanced electron attachment to Rydberg states in molecular hydrogen volume discharges. *J. Appl. Phys. 85, 7064*, 1999.

[47] G. J. Schulz and R. K. Asundi. FORMATION OF H BY ELECTRON IMPACT ON H2 AT LOW ENERGY. *Phys. Rev. 15, 25*, 1965.

[48] G. J. Schulz and R. K. Asundi. Isotope Effect in the Dissociative Attachment in H2 at Low Energy. *Phys. Rev. 158, 25*, 1967.

[49] Yu. N. Demkov. Isotopic Effect in the Resonance Dissociative Capture of an Electron and Quasistationary States of Molecules. *Physics Letters 15, 3 235*, 1965.

[50] Yu.I. Belchenko, G.I. Dimov, and V.G. Dudnikov. A POWERFUL INJECTOR OF NEUTRALS WITH A SURFACE-PLASMA SOURCE OF NEGATIVE IONS. *NUCLEAR FUSION 14*, 1974.

[51] H. Verbeek and W. Eckstein. Positive and negative hydrogen ions backscattered from Au, Ta, and Th02 in the energy range up to 15 keV. *J. Appl. Phys., Vol. 47, No.5*, 1976.

[52] J. Los and J.J.C. Geerlings. Charge Exchange in Atom-Surface Collisions. *PHYSICS REPORTS (Review Section of Physics Letters) 190, No. 3 133190*, 1990.

[53] M. Bacal and M. Wada. Negative hydrogen ion production mechanisms. *APPLIED PHYSICS REVIEWS 2, 021305 (2015)*, 2015.

[54] H. Verbeek, W. Eckstein, and R. S. Bhattacharya. NEGATIVE HYDROGEN ION FORMATION BY BACKSCATTERING FROM SOLID SURFACES. *Surface Science 95, 380-390*, 1980.

[55] M. Bacal, R. McAdams, and E. Surrey. Extracted H ion current enhancement due to caesium seeding at different plasma grid bias. *Review of Scientific Instruments 85, 02B103 doi: 10.1063/1.4825387*, 2014.

[56] D. Wunderlich, R Gutser, and U Fantz. PIC code for the plasma sheath in large caesiated RF sources for negative hydrogen ions. *Plasma Sources Sci. Technol. 18 045031*, 2009.

[57] R McAdams, A J T Holmes, D B King, and E Surrey. Transport of negative ions across a double sheath with a virtual cathode. *Plasma Sources Sci. Technol. 20 035023*, 2011.

[58] L. Schiesko, M. Carrere, J. M. Layet, and G. Cartry. A comparative study of H- and D-production on graphite surfaces in H2 and D2 plasmas. *Plasma Sources Sci. Technol. 19 045016 (7pp)*, 2010.

[59] F. Wyputta, R. Zimny, and H. Winter. H- formation in grazing collisions of fast protons with an Al(111) surface. *Nuclear Instruments and Methods in Physics Research BS8 379-383*, 1991.

[60] U. Fantz, P. Franzen, and D. Wnderlich. Development of negative hydrogen ion sources for fusion: Experiments and modelling. *Chemical Physics 398 716*, 2012.

[61] J. P. Boeuf, B. Chaudhury, and L. Garrigues. Physics of a magnetic filter for negative ion sources. I. Collisional transport across the filter in an ideal, 1D filter. *Physics of Plasmas (1994-present) 19, 113509*, 2012.

[62] J. P. Boeuf, B. Chaudhury, and L. Garrigues. Physics of a magnetic filter for negative ion sources. II. E B drift through the filter in a real geometry. *Physics of Plasmas (1994-present) 19, 113510*, 2012.

[63] K. N. Leung and M. Bacal. H ion density measurement in a tandem multicusp discharge. *Review of Scientific Instruments 55, 338*, 1984.

[64] Kevin Mellon. ENHANCED PRODUCTION OF NEGATIVE IONS IN A PULSED VOLUME ION SOURCE. *PhD Thesis, Dublin City University*, 1993.

[65] Deidre Boilson. Negative Ion Measurements in RF and DC Temporally Modulated Hydrogen Volume Ion Sources. *PhD thesis, Dublin City University*, 2000.

[66] Seiji Samukawa and Tetsu Mieno. Pulse-time modulated plasma discharge for highly selective, highly anisotropic and charge-free etching. *Plasma Sources Sci. Technol. 5 (1996) 132138*, 1996.

[67] Seiji Samukawa, Keisuke Sakamoto, and Katsunori Ichiki. High-Efficiency Low Energy Neutral Beam Generation Using Negative Ions in Pulsed Plasma. *Jpn. J. Appl. Phys. Vol. 40 (2001) pp. L997-L999*, 2001.

[68] Rubin Ye, Takamasa Ishigaki, and Tadahiro Sakuta. Controlled generation of pulse-modulated RF plasmas for materials processing. *Plasma Sources Sci. Technol. 14 (2005) 387396 doi:10.1088/0963-0252/14/2/022*, 2005.

[69] M. B. Hopkins, M. Bacal, and W. G. Graham. Enhanced volume production of negative ions in the post discharge of a multicusp hydrogen discharge. *Journal of Applied Physics 70, 2009 (1991) doi: 10.1063/1.349486*, 1991.

[70] L. J. Overzet, B. A. Smith, J. Kleber, and S. K. Kanakasabapathy. Negative Ion Extraction from Pulsed Discharges. *Jpn. J. Appl. Phys. Vol. 36 (1997) pp. 2443-2449*, 1997.

[71] S. Banna *et. al.* Pulsed high-density plasmas for advanced dry etching processes. *Journal of Vacuum Science and Technology A 30, 040801*, 2012.

[72] Seiji Samukawa. Pulse-time-modulated electron cyclotron resonance plasma etching for highly selective, highly anisotropic, and notch-free polycrystalline silicon patterning. *Appl. Phys. Lett. 64, 3398*, 1994.

[73] Mitsuru Okigawa, Yasushi Ishikawa, Yoshinari Ichihashi, and Seiji Samukawa. Ultraviolet-induced damage in fluorocarbon plasma and its reduction by pulse-time modulated plasma in charge coupled device image sensor wafer processes. *Journal of Vacuum Science and Technology B: Microelectronics and Nanometer Structures Processing, Measurement, and Phenomena 22, 2818*, 2004.

[74] Ankur Agarwal, Phillip J. Stout, Samer Banna, Shahid Rauf, Ken Tokashiki, Jeong-Yun Lee, and Ken Collins. Effect of simultaneous source and bias pulsing in inductively coupled plasma etching. *Journal of Applied Physics 106, 103305*, 2009.

[75] M. V. Malyshev, V. M. Donnelly, J. I. Colonell, and S. Samukawa. Dynamics of pulsed-power chlorine plasmas. *Journal of Applied Physics 86, 4813*, 1999.

[76] JohnB.Boffard, S. Wang, Chun C. Lin, and A. E. Wendt. Detection of fast electrons in pulsed argon inductively-coupled plasmas using the 420.1419.8nm emission line pair. *Plasma Sources Sci. Technol. 24*, 2015.

[77] "M. A. Lieberman and A. J. Lichtenberg". *"Principles of Plasma Discharges and Materials Processing, Second Edition"*. "Wiley", "2005".

[78] M A Lieberman and S Ashida. Global models of pulse-power-modulated high density, low-pressure discharges. *Plasma Sources Sci. Technol. 5 145*, 1996.

[79] I. D. Kaganovich, D. J. Economou, B. N. Ramamurthi, and V. Midha. Negative Ion Density Fronts during Ignition and Extinction of Plasmas in Electronegative Gases. *PHYSICAL REVIEW LETTERS VOLUME 84, NUMBER 9*, 2000.

[80] Martin Lampe Wallace, M. Manheimer, Richard F. Fernsler, Steven P. Slinker, and Glenn Joyce. The physical and mathematical basis of stratification in electronegative plasmas. *Plasma Sources Sci. Technol. 13 1526*, 2004.

[81] Vikas Midha and Demetre J Economou. Spatio-temporal evolution of a pulsed chlorine discharge. *Plasma Sources Sci. Technol. 9*, 2000.

[82] B. Ramamurthi and D. J. Economou. Two-dimensional pulsed-plasma simulation of a chlorine discharge. *J. Vac. Sci. Technol. A 20(2)*, 2002.

[83] I. D. Kaganovich, B. N. Ramamurthi, and Demetre J. Economou. Spatiotemporal dynamics of charged species in the afterglow of plasmas containing negative ions. *PHYSICAL REVIEW E, VOLUME 64, 036402*, 2001.

[84] I. D. Kaganovich, B. N. Ramamurthi, and Demetre J. Economou. Self-trapping of negative ions due to electron detachment in the afterglow of electronegative gas plasmas. *APPLIED PHYSICS LETTERS VOLUME 76, NUMBER 20*, 2000.

[85] D. Smith, A. G. Dean, and N. G. Adams. Space charge fields in afterglow plasmas. *J. Phys. D: Appl. Phys. 7 1944*, 1974.

[86] Tim Baloniak, Rudiger Reuter, and Achim von Keudell. Fundamental aspects of substrate biasing: ion velocity distributions and nonlinear effects. *J. Phys. D: Appl. Phys. 43 (2010) 335201*, 2010.

[87] M. V. Malyshev and V. M. Donnelly. Dynamics of inductively-coupled pulsed chlorine plasmas in the presence of continuous substrate bias. *Plasma Sources Sci. Technol. 9*, 2000.

[88] P. Subramonium and M. Kushner. Extraction of negative ions from pulsed electronegative inductively coupled plasmas having a radio-frequency substrate bias. *J. Vac. Sci. Technol. A 22(3)*, 2004.

[89] Samer Banna, Ankur Agarwal, Ken Tokashiki, Hong Cho, Shahid Rauf, Valentin Todorow, Kartik Ramaswamy, Ken Collins, Phillip Stout, Jeong-Yun Lee, Junho Yoon, Kyoungsub Shin, Sang-Jun Choi, Han-Soo Cho, Hyun-Joong Kim, Changhun Lee, and Dimitris Lymberopoulos. Inductively Coupled Pulsed Plasmas in the Presence of Synchronous Pulsed Substrate Bias for Robust, Reliable, and Fine Conductor Etching. *IEEE TRANSACTIONS ON PLASMA SCIENCE, VOL. 37, NO. 9*, 2009.

[90] Hyungjoo Shin, Weiye Zhu, Lin Xu, Vincent M Donnelly, and Demetre J Economou. Control of ion energy distributions using a pulsed plasma with synchronous bias on a boundary electrode. *Plasma Sources Sci. Technol. 20 (2011) 055001*, 2011.

[91] Lin Xu, Demetre J. Economou, and Vincent M. Donnelly. Extraction of a nearly monoenergetic ion beam using a pulsed plasma. *Appl. Phys. Lett. 87, 041502*, 2005.

[92] R. S. Hemsworth and D. Boilson. Considerations for the development of Neutral Beam Injection for Fusion Reactors or DEMO. *AIP Conference Proceedings 1869, 060001*, 2017.

[93] H.P.L. de Esch and L. Svensson. Negative ion beam halo mitigation at the 1 MV testbed at IRFM. *Fusion Engineering and Design 86 363368*, 2011.

[94] K. Tsumori, W. R. Koppers, R. M. A. Heeren, M. F. Kadodwala, J. H. M. Beijersbergen, and A. W. Kleyn. Large ion yields in hydrogen scattering from a graphite surface. *Journal of Applied Physics 81, 6390*, 1997.

[95] P. Wurz, R. Schletti, and M.R. Aellig. Hydrogen and oxygen negative ion production by surface ionization using diamond surfaces. *Surface Science 373 56-66*, 1997.

[96] J.A. Scheer M. Wieser, P. Wurz, P. Bochsler, E. Hertzberg, S.A. Fuselier, F.A. Koeck, R.J. Nemanich, and M. Schleberger. High negative ion yield from light molecule scattering. *Nuclear Instruments and Methods in Physics Research B 230 330339*, 2005.

[97] G. Cartry, L. Schiesko, C. Hopf, A. Ahmad, M Carrre, J. M. Layet, P. Kumar, and R. Engeln. Production of negative ions on graphite surface in H2/D2 plasmas: Experiments and srim calculations. *Physics of Plasmas (1994-present) 19, 063503*, 2012.

[98] M.A. Gleeson and A.W. Kleyn. Effects of Cs-adsorption on the scattering of low energy hydrogen ions from HOPG. *Nuclear Instruments and Methods in Physics Research B 157 48-54*, 1999.

[99] R.A. Vidal F. Bonetto, J. Ferrn, M.A. Romero, Evelina A. Garca, and E.C. Goldberg. Electron capture and loss in the scattering of H+ from HOPG graphite. *Surface Science 605 1823*, 2011.

[100] Ahmad Ahmad, Cedric Pardanaud, Marcel Carrre, Jean-Marc Layet, and Gilles Cartry *et. al.* Negative-ion production on carbon materials in hydrogen plasma: influence of the carbon hybridization state and the hydrogen content on H- yield. *Journal of Physics D: Applied Physics, Institute of Physics: Hybrid Open Access, 2014, 47, pp.085201. ¡10.1088/0022-3727/47/8/085201¿. ¡hal-00943265¿*, 2014.

[101] P. Kumar, A. Ahmad, C. Pardanaud, M. Carrere, J. M. Layet, G. Cartry, F. Silva, A. Gicquel, and R. Engeln. Enhanced negative ion yields on diamond surfaces at elevated temperatures. *J. Phys. D: Appl. Phys. 44 372002 (4pp)*, 2011.

[102] L. Schiesko, M. Carrre, J.-M. Layet, and G. Cartry. Negative ion surface production through sputtering in hydrogen plasma. *Applied Physics Letters 95, 191502*, 2009.

[103] C. Bandis and B.B. Pate. Photoelectric emission from the negative electron affinity (100) diamond surface- exciton effects. *Surface Science 350 315-321*, 1996.

[104] M. Bacal and M. Wada. Effect due to plasma electrode adsorbates upon the negative ion current and electron current extracted from a negative ion source. *AIP Conference Proceedings 1869, 030025*, 2017.

[105] R. I. Hall, I. ade, M. Landau, F. Pichou, and C. Schermann. Vibrational Excitation of Hydrogen via Recombinative Desorption of Atomic Hydrogen Gas on a Metal Surface. *Phys. Rev. Lett. 60, 337*, 1988.

[106] R. Friedl, U. Kurutz, and U. Fantz. Efficiency of Cs-free materials for negative ion production in H2 and D2 plasmas. *AIP Conference Proceedings 1869, 030022*, 2017.

[107] J. Zacks, I. Turner, I. Day, K. Flinders, B. Crowley, and R. McAdams. H production on a graphite surface in a hydrogen plasma. *Plasma Sources Sci. Technol. 17 035023*, 2008.

[108] J. Zacks, I. Turner, I. Day, K. Flinders, B. Crowley, and R. McAdams. Update on developments at SNIF. *AIP Conference Proceedings 1655, 030012*, 2015.

[109] Seiji Samukawa. Plasma-Induced Damage and Its Control in Plasma Etching Processes. *IEEE 1-4244-0757*, 2007.

[110] Kenji Ishikawa, Mitsuru Okigawa, Yasushi Ishikawa, Seiji Samukawa, and Satoshi Yamasaki. In vacuo measurements of dangling bonds created during Ar-diluted fluorocarbon plasma etching of silicon dioxide films. *APPLIED PHYSICS LETTERS 86, 264104*, 2005.

[111] Seiji Samukawa. Ultimate Top-down Etching Processes for Future Nanoscale Devices: Advanced Neutral-Beam Etching. *Japanese Journal of Applied Physics Vol. 45, No. 4A, pp. 23952407*, 2006.

[112] Koichi Hashimoto. Charge Damage Caused by Electron Shading Effect. *Jpn. J. Appl. Phys. Vol. 33 pp 6013-6018*, 1994.

[113] Tomohiro Kubota *et. al.* 200-mm-diameter neutral beam source based on inductively coupled plasma etcher and silicon etching. *Journal of Vacuum Science and Technology A 28, 1169*, 2010.

[114] Seiji Samukawa and Keisuke Sakamoto. Generating high-efficiency neutral beams by using negative ions in an inductively coupled plasma source. *Journal of Vacuum Science and Technology A 20, 1566*, 2002.

[115] S. N. Abolmasov, Takuya Ozaki, and Seiji Samukawa. Characterization of neutral beam source based on pulsed inductively coupled discharge: Time evolution of ion fluxes entering neutralizer. *JOURNAL OF VACUUM SCIENCE AND TECHNOLOGY A VACUUM SURFACES AND FILMS*, 2007.

[116] Hiroki Kuwano and Hiroki Kuwano. Energy distribution and formation mechanism of fast atoms in a fast atom beam. *Journal of Applied Physics 72, 13*, 1992.

[117] Sang Ki Nam, Demetre J. Economou, and Vincent M. Donnelly. Generation of Fast Neutral Beams by Ion Neutralization in High-Aspect-Ratio Holes: A Particle-in-Cell Simulation Study. *IEEE TRANSACTIONS ON PLASMA SCIENCE, VOL. 35, NO. 5*, 2007.

[118] Alok Ranjan, Vincent M. Donnelly, and Demetre J. Economou. Energy distribution and flux of fast neutrals and residual ions extracted from a neutral beam source. *Journal of Vacuum Science and Technology A 24, 1839*, 2006.

[119] Seiji Samukawa. High-performance and damage-free neutral-beam etching processes using negative ions in pulse-time-modulated plasma. *Applied Surface Science 253 66816689*, 2007.

[120] Francis F. Chen. Langmuir Probe Diagnostics. *Mini-Course on Plasma Diagnostics, IEEE-ICOPS meeting*, 2003.

[121] T. E. Sheridan and J. Goree. Collisional plasma sheath model. *Physics of Fluids B: Plasma Physics 3, 2796*, 1991.

[122] Z. Zakrzewski and T. Kopiczynski. Effect of collisions on positive ion collection by a cylindrical Langmuir probe. *Plasma Physics, Vol. 16, 1195*, 1974.

[123] "P. M. Chung, L. Talbot, and K. J. Touryan". *"Electric Probes in Stationary and Flowing Plasmas: Theory and Application"*. "Springer", "2005".

[124] Isaac D. Sudit and R. Claude Woods. A study of the accuracy of various Langmuir probe theories. *Journal of Applied Physics 76, 4488*, 1994.

[125] K-U Riemann. Kinetic analysis of the collisional plasmasheath transition. *J. Phys. D: Appl. Phys. 36 2811*, 2003.

[126] Francis F. Chen. Langmuir probes in RF plasma: Surprising validity of OML theory. *Plasma Sources Sci. Technol. 18 035012*, 2009.

[127] A. K. Bhattacharya and J. H. Ingold. Diffusion Cooling of Electrons in Afterglow Plasmas. *Journal of Applied Physics 43, 1535*, 1972.

[128] R. E. Robson. Diffusion cooling of electrons in a finite gas. *PHYSICAL REVIEW A VOLUME 13, NUMBER 4*, 1976.

[129] V. I. Demidov, C. A. DeJoseph Jr, and A. A. Kudryavtsev. Ionization kinetics and EH mode transition in a noble gas, low-pressure pulsed ICP discharge. *Plasma Sources Sci. Technol. 13 600*, 2013.

[130] Xi-Ming Zhu and Yi-Kang Pu. A simple collisionalradiative model for low-pressure argon discharges. *J. Phys. D: Appl. Phys. 40, 25332538*, 2007.

[131] Mark W. Kiehlbauch and David B. Graves. Modeling argon inductively coupled plasmas: The electron energy distribution function and metastable kinetics. *Journal of Applied Physics 91, 3539*, 2002.

[132] Sang-Hun Seo, Jung-In Hong, and Hong-Young Chang. Electron energy distribution function and plasma potential in a planar inductive argon discharge without electrostatic screen. *Appl. Phys. Lett., Vol. 74, No. 19*, 1999.

[133] V A Godyak, R B Piejak, and B M Alexandrovich. Electron energy distribution function measurements and plasma parameters in inductively coupled argon plasma. *Plasma Sources Sci. Technol. 11, 525*, 2002.

[134] Sumio Ashida, C. Lee, and M. A. Lieberman. Spatially averaged (global) model of time modulated high density argon plasmas. *Journal of Vacuum Science & Technology A 13, 2498*, 1995.

[135] G. A. Hebner and C. B. Fleddermann. Characterization of pulse-modulated inductively coupled plasmas in argon and chlorine. *Journal of Applied Physics 82, 2814*, 1997.

[136] Sumio Ashida, M. R. Shim, and M. A. Lieberman. Measurements of pulsed-power modulated argon plasmas in an inductively coupled plasma source. *Journal of Vacuum Science & Technology A 14, 391*, 1996.

[137] D. Marinov, Z. el Otell, M. D. Bowden, and N. St. J. Braithwaite. Extraction and neutralization of positive and negative ions from a pulsed electronegative inductively coupled plasma. *Plasma Sources Sci. Technol. 24 065008 (9pp)*, 2015.

[138] J. I. Hong, S. H. Seo, S. S. Kim, N. S. Yoon, C. S. Chang, and H. Y. Chang. Electron temperature control with grid bias in inductively coupled argon plasma. *Physics of Plasmas 6, 1017*, 1999.

[139] Christian Bohm and Jrome Perrin. Retarding-field analyzer for measurements of ion energy distributions and secondary electron emission coefficients in low-pressure radio frequency discharges . *Review of Scientific Instruments 64, 31*, 1993.

[140] P. Subramonium and M. Kushner. Pulsed plasmas as a method to improve uniformity during materials processing. *Journal of Applied Physics 96, 82*, 2004.

[141] Hyo-Chang Lee, B. H. Seo, Deuk-Chul Kwon, J. H. Kim, D. J. Seong, S. J. Oh, C.-W. Chung, K. H. You, and ChaeHo Shin. Evolution of electron temperature in inductively coupled plasma. *Appl. Phys. Lett. 110, 014106*, 2017.

[142] Snejana Iordanova and Tsvetelina Paunska. A collisional radiative model of hydrogen plasmas developed for diagnostic purposes of negative ion sources. *Review of Scientific Instruments 87, 02B110*, 2016.

[143] A. Ahmad, J. Dubois, T. Pasquet, M. Carrere, J. M. Layet, J. B. Faure, G. Cartry, P. Kumar, T. Minea, S. Mochalskyy, and A. Simonin. Negative-ion surface production in hydrogen plasmas: modeling of negative-ion energy distribution functions and comparison with experiments. *Plasma Sources Sci. Technol. 22 025006*, 2013.

[144] R. Zorat and D. Vender. Global model for an rf hydrogen inductive plasma discharge in the deuterium negative ion source experiment including negative ions. *J. Phys. D: Appl. Phys. 33 17281735*, 2000.

[145] V. I. Demidov, S. V. Ratynskaia, and K. Rypdal. Electric probes for plasmas: The link between theory and instrument. *Review of Scientific Instruments 73, 3409*, 2002.

[146] Jung-Sik Yoon, Mi-Young Song, Jeong-Min Han, Sung Ha Hwang, Won-Seok Chang, BongJu Lee, and Yukikazu Itikawa. Cross Sections for Electron Collisions with Hydrogen Molecules. *Journal of Physical and Chemical Reference Data 37, 913*, 2008.

[147] H. Tawara, Y. Itikawa, H. Nishimura, and M. Yoshino. Cross Sections and Related Data for Electron Collisions with Hydrogen Molecules and Molecular Ions. *Journal of Physical and Chemical Reference Data 19, 617*, 1990.

[148] L. Sirghi, Y. Hatanaka, and G. Popa. Control of plasma parameters and wall sheath voltage in radio frequency magnetron discharge by grid bias. *Journal of Applied Physics 91, 4026*, 2002.

[149] U. Kurutz, R. Friedl, and U. Fantz. Investigations on Cs-free alternatives for negative ion formation in a low pressure hydrogen discharge at ion source relevant parameters. *Plasma Phys. Control. Fusion 59 (2017) 075008*, 2017.

[150] M. Stenrup, sa Larson, and Nils Elander. Mutual neutralization in low-energy H++H collisions: A quantum ab initio study. *Physical Review A 79, 012713*, 2009.

[151] S. Szucs, M. Karemera, M. Terao, and F. Brouillard. Experimental study of the mutual neutralisation of H+ and H- between 5 and 2000 eV. *J. Phys. B: At. Mol. Phys. 17 1613*, 1984.

[152] H. Amemiya. Plasmas with negative ions-probe measurements and charge equilibrium. *J. Phys. D: Appl. Phys. 23 999*, 1990.

[153] H. Amemiya. Probe Diagnostics in Negative Ion Containing Plasmas. *J. Phys. Soc. Jpn. 57 no. 3*, 1988.

[154] H. Amemiya and Y. Sakamoto. Negative Ions and Energy Distribution in a Hydrogen Plasma Device. *Jpn. J. Appl. Phys. 26 1170*, 1987.

[155] R. Ichiki, Shinji Yoshimura, Tsuguhiro Watanabe, Yoshiharu Nakamura, and Yoshinobu Kawai. Experimental observation of dominant propagation of the ion-acoustic slow mode in a negative ion plasma and its application. *Physics of Plasmas 9, 4481*, 2002.

[156] J. Y. Zhang, R. Ichiki, and Y. Kawai. Behaviour of sheath voltage in negative ion plasma. *J. Phys.: Conf. Ser. 441 012010*, 2013.

[157] R. Deutsch and E. Rauchle. Influence of negative ions on the plasma boundary sheath. *Physical Review A, Volume 46, No. 6*, 1992.

[158] R. N. Franklin. The plasmawall boundary region in negative-ion-dominated plasmas at low pressures. *Plasma Sources Sci. Technol. 9 191*, 2000.